Remote sensing of sea ice leads with Sentinel-1 C-band synthetic aperture radar

submitted by

Dmitrii Murashkin

for the degree of
Doctor of Natural Sciences

Reviewer 1: Dr. Gunnar Spreen
Reviewer 2: Prof. Dr. Christian Haas

Submission: 13 December 2023
Colloquium: 16 May 2024

Institute of Environmental Physics
University of Bremen

Abstract

The presence of leads with open water or thin ice is an important feature of the Arctic sea ice cover. Leads regulate the heat, gas, and moisture fluxes between the ocean and atmosphere and are areas of high ice growth rates during periods of freezing conditions. In the present study an algorithm providing an automatic lead detection based on Synthetic Aperture Radar (SAR) images is developed using traditional machine learning techniques and deep learning methods. The algorithm is applied to a wide range of Sentinel-1 scenes taken over the Arctic Ocean. Distribution of the detected leads in the Arctic during winter seasons 2016–2021 is then analyzed.

An important part of the algorithm development is the data preprocessing as the classification quality depends on the quality of the input images. An advanced data preparation technique improves consistency of the cross-polarization channel and enables the use of dual-polarization SAR images. By using both the HH and the HV channels instead of single co-polarized observations the algorithm is able to detect more leads compared to the use of the HH polarization only.

First, a traditional machine learning approach is described. It is based on polarimetric features and texture features derived from the grey level co-occurrence matrix. The Random Forest classifier is used to investigate the individual feature importance on the lead detection. The precision–recall curve representing the quality of the classification is assessed to define a threshold for the binary lead/sea ice classification. The algorithm produces a lead classification with more than 90% precision with 60% of all leads classified, as evaluated on the test data. The precision can be increased by the cost of the amount of leads detected. Classification quality is improved by introducing an advanced binarization method based on watershed segmentation. Further improvements include object shape analysis resulting in a shape-based filter, which efficiently removes objects appearing due to noise patterns over young ice.

Second, an algorithm based on a convolutional neural network is developed. It shows more robust results compared to the algorithm based on the gray level co-occurrence matrix with Random Forest classification and is applicable to the entire Arctic Ocean. Classification results are evaluated against the dataset which does not include training or testing data, and are also compared to Sentinel-2 optical satellite images.

Finally, the lead detection algorithm is applied to all Sentinel-1 EW GRDM scenes

taken in five winter seasons, 1 November – 30 April of 2016–2021 years. 3-day composite pan-Arctic lead maps with the native Sentinel-1 40 meters pixel spacing are produces. The frequency of lead occurrence derived from these maps is compared with MODIS thermal infrared lead detection results. The lead area fraction is compared with the AMSR2 passive microwave observations. The lead area distribution, lead length, and lead width distributions, as well as the lead orientation distributions, are analyzed in the following regions of the Arctic Ocean: Fram Strait, Barents Sea, Kara Sea, Laptev Sea, East Siberian Sea, Chukchi Sea, Beaufort Sea, Central Arctic. Each region shows the presence of regularity in lead orientation, the preferred orientation has little variation from year to year and during season. The lead width distribution is found to follow the power low with the exponent of 1.86 with 0.16 standard deviation. The yearly mean lead area fraction derived from Sentinel-1 images varies from 2.5% to 3.7% during winter seasons 2016–2021.

Contents

1 Introduction

Average surface temperature of the planet has been increasing during the last decades. Temperature in the Arctic region has been increasing twice faster that the average for the planet as shown in Figure 1.1 (Serreze and Francis, 2006; Dai et al., 2019; Wendisch et al., 2023). One of the most notable effect of the increasing temperatures is the decrease in sea ice extend and sea ice thickness (Kwok, 2018) in the Arctic Ocean, shown in Figure 1.2. Since the beginning of microwave satellite observations of sea ice in 1970s, the maximal sea ice extent at the end of winter and the minimal sea ice extent at the end of summer have been decreasing. More importantly, thick sea ice covering the major part of the Arctic in 1980s has been replaced with a thin young ice, leaving a significant part of the Arctic Ocean open during summer (Kwok, 2018). Decrease in thick multiyear ice, i.e. the sea ice that have survive at least one summer, due to melting is clearly seen in Figure 1.3. During last years, most of thick multiyear ice is located north of Greenland and in the Canadian Arctic. The changes in sea ice conditions influence the heat exchange between the ocean and the atmosphere, which, in turn, influences the climate system of the entire planet (Serreze et al., 2009).

A significant part of the Arctic Ocean is covered with sea ice. Sea ice works as an insulation layer between the ocean and the atmosphere. The presence of leads is an important feature of the Arctic sea ice cover. Leads are areas of open water or thin ice, which are usually of elongated shape, as illustrated in Figure 1.4. They appear as a result of ice fracturing due to shear and divergence stresses in the sea ice cover. These stresses are forced by winds in the atmosphere, as well as by the ocean currents and tides (Weiss, 2003). Leads regulate the heat, gas, and moisture fluxes between the ocean and the atmosphere and are places of increased sea ice production during periods of freezing conditions. Hence, the spatial and temporal distributions of leads are of interest for climate studies (Maykut, 1978; Wang et al., 2016a). In addition to that, leads are areas where sunlight can penetrate the sea ice cover, therefore biological activity in the ocean like phytoplankton blooms takes place there (Assmy et al., 2017). The life of Arctic animals (e.g., walruses, polar bears, birds) is often tied to leads (Stirling, 1997). Furthermore, the mapping of sea ice leads plays an important role for navigation by providing a more fuel-efficient and safe way for vessels through the pack ice.

There is a range of lead properties that are of a particular interest for environmental

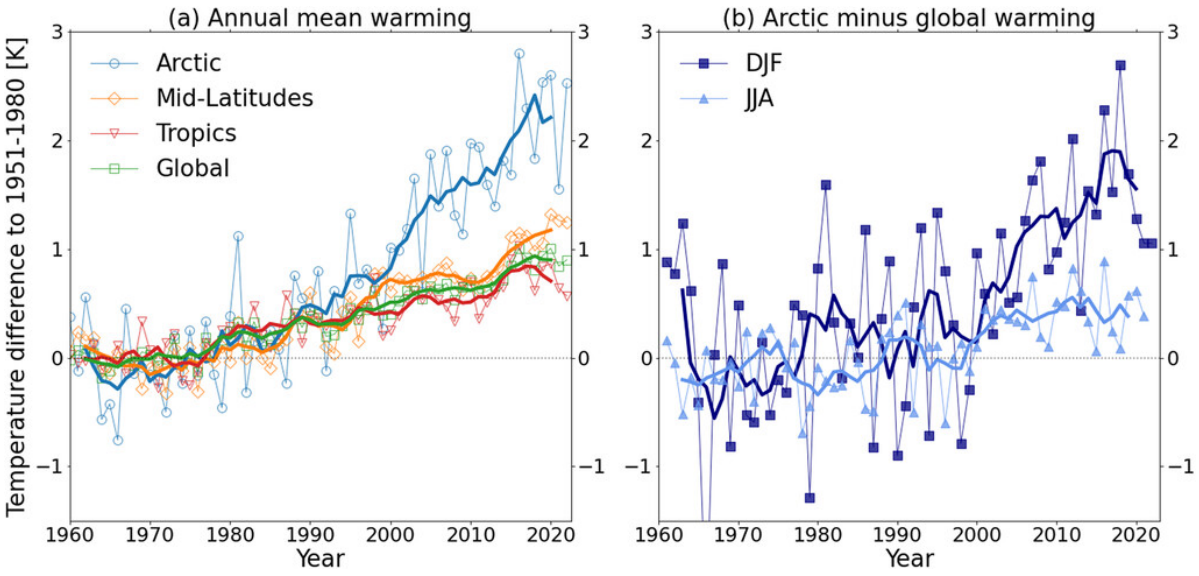

Figure 1.1: a - global average surface temperature (in green), average surface temperatures in tropics (in red), mid-latitudes (in yellow), and Arctic (in blue). b - difference between average Arctic and global temperatures. Images are from Wendisch et al. (2023)

processes and climate numerical modelling. Lead area fraction is related to the open water area within sea ice cover and, thus, is of importance for ocean–atmosphere heat exchange (Chechin et al., 2019). It is also accounted in the albedo feedback mechanism (Curry and Schramm, 1995; Lüpkes et al., 2008) which has a significant influence on the heat balance in the Arctic (Ebert and Curry, 1993). The frequency of lead occurrence provides information on areas featuring high sea ice production rates in winter. The lead orientation indicates typical direction of stresses in the sea ice cover. The lead intersection angle is important for understanding and modelling of sea ice mechanics (Hutchings et al., 2005). Lead intersection angle has been studied on large-scale linear kinematic features by Hutter et al. (2019) and simulated with an ice fracturing model by Ringeisen et al. (2019). Sea ice fracturing is found to follow a power law by Weiss (2003), therefore the lead size distribution is expected to follow a power law. Wang et al. (2016b) have found the distribution of distance between leads, considered as a proxy for ice floe size, which is also found to be scaling with a power law by Rothrock and Thorndike (1984), to not to follow the power law at small scales due to the different mechanism of lead occurrence. At a large scale leads appear due to wind and internal stress, at a small scale wave actions play a major role in the process of lead occurrence. The lead width distribution influences the turbulent heat transfer between the ocean and the atmosphere (Marcq and Weiss, 2012).

Arctic Ocean is often split into the following regions: Fram Strait, Barents Sea, Kara Sea, Laptev Sea, East Siberian Sea, Chukchi Sea, Beaufort Sea, Central Arctic, as shown

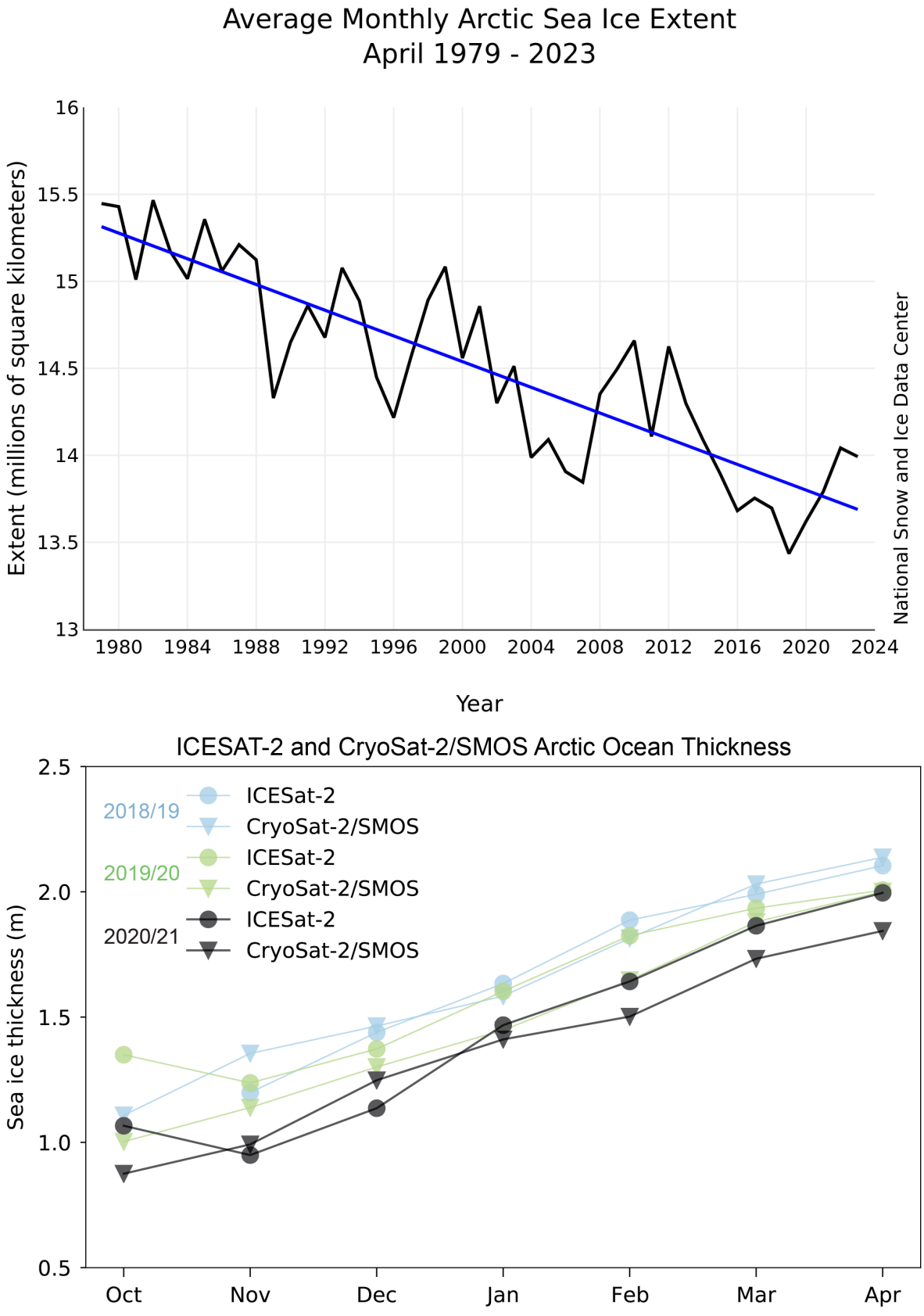

Figure 1.2: top - Maximal sea ice extent (image by NSIDC), bottom - sea ice thickness (image from Arctic Report Card on Sea Ice by Meier and others).

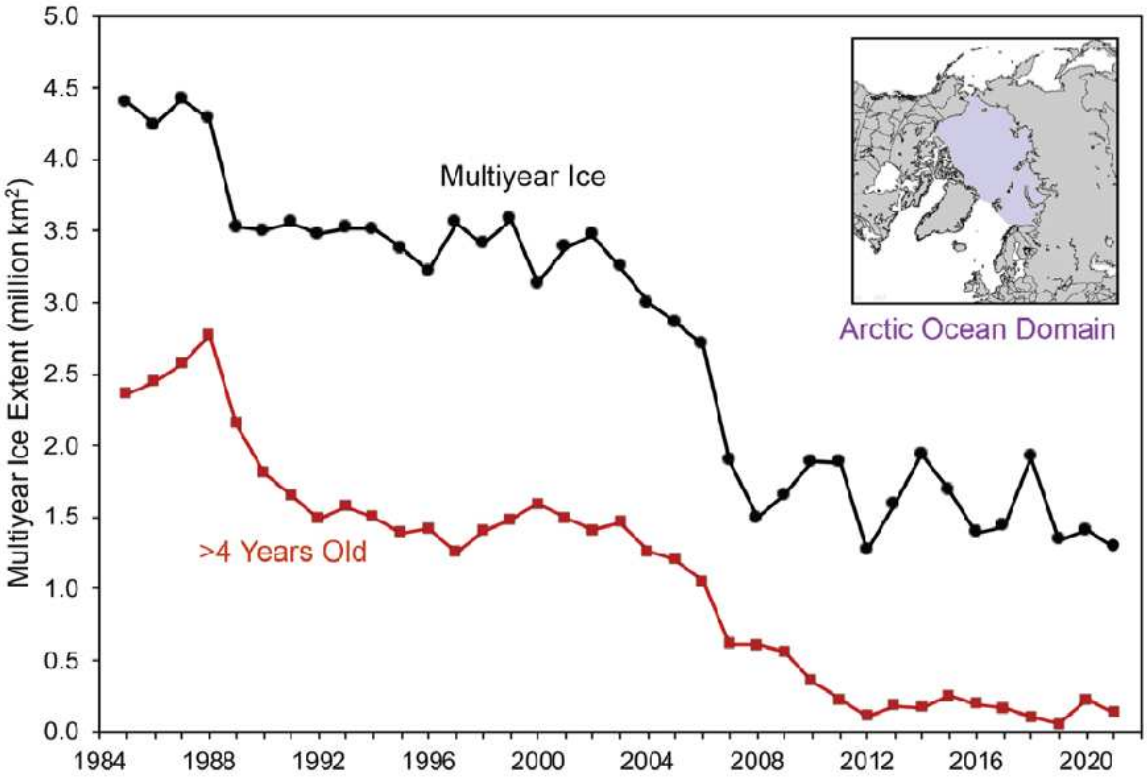

Figure 1.3: Multiyear sea ice extent (National Snow and Ice Data Center et al., 2022)

Figure 1.4: Leads in sea ice cover observed north of Svalbard in 2015

Figure 1.5: Arctic Ocean is split according to Meier et al. (2007) into the following regions: Fram Strait, Barents Sea, Kara Sea, Laptev Sea, East Siberian Sea, Chukchi Sea, Beaufort Sea, Central Arctic.

in Figure 1.5, defined by Meier et al. (2007). Each of the regions have a different ocean and atmosphere conditions, and, therefore, different sea ice conditions.

Due to harsh weather conditions in the Arctic, capabilities for field studies of sea ice are limited. Remote sensing methods provide measurements in the Arctic covering large areas. A range of satellite and airborne instruments have been developed for sea ice surveys over the Arctic with various spatial and temporal resolutions. Several methods have been developed for discrimination of sea ice and water based on remote sensing observations taken in the visible, infrared and microwave parts of the electromagnetic spectrum. They are described in the following four paragraphs.

A large number of Advanced Very High Resolution Radiometer (AVHRR) infrared images were analyzed by Lindsay and Rothrock (1995) to determine lead characteristics. The lead detection algorithm is based on the surface temperature analysis derived from thermal infrared measurements. A threshold was set to discriminate open water from sea ice. The resolution of the data is about 2–3 km. In the studies conducted by Willmes and Heinemann (2015, 2016); Reiser et al. (2020) Moderate Resolution Imaging

Spectroradiometer (MODIS) thermal infrared imagery was used for lead detection. The method is based on a threshold applied to MODIS images with the background temperature subtracted. The resulting maps with resolution of 1 km contain three classes: sea ice, leads, and lead-like structures. Both the AVHRR and MODIS data and results are affected by cloud contamination.

The cloud influence is significantly reduced for observations in the microwave spectrum, where weather conditions have little influence on measurements. Lead detection based on microwave altimetry was studied by Wernecke and Kaleschke (2015) using data from CryoSat-2. The algorithm to discriminate leads from ice is based on the maximum power, the pulse peakiness and other parameters (e.g. the leading edge width, the trailing edge width, the stack standard deviation, the stack excess kurtosis) of the reflected altimeter signal.

Based on observations with the Advanced Microwave Scanning Radiometer AMSR-E, Röhrs and Kaleschke (2012) and Bröhan and Kaleschke (2014) estimated lead concentration and lead orientation statistics. For AMSR-E data on a 6.25 km grid, they detect leads wider than 3 km, which results in a detection of about 50% of the lead area that is seen on MODIS optical images.

Synthetic Aperture Radar (SAR) is able provide high resolution data with large spatial and temporal coverage, which is important for lead mapping since about a quarter of head flux was found to be coming from leads narrower than 1 km by Qu et al. (2019). SAR images are widely used for sea ice type classification and ice-water discrimination (Dierking, 2010, 2013). Ivanova et al. (2016) used a threshold approach on the HH-band (HH: transmitting and receiving in horizontal polarization) of the Envisat ASAR instrument for water-ice discrimination. To improve the quality of object classification the directly measured data (e.g. backscatter intensities) are often extended with texture feature analysis. Ice-water classification based on dual-polarized SAR images (Radarsat-2) with the additional texture information is described by Leigh et al. (2014). The use of a support vector machine on the features based on the grey-level co-occurrence matrix (Haralick et al., 1973) is suggested. This combination was previously used for sea ice type classification by Liu et al. (2015), Korosov and Park (2016). A similar approach is used by Zakhvatkina et al. (2017) for ice-water discrimination. A neural network with texture features based on the grey-level co-occurrence matrix was used for classification of Envisat SAR images by Zakhvatkina et al. (2013). Another method that provides complementary information to the backscatter intensity is based on polarimetric features (e.g., Moen et al., 2015). Polarimetric features are used for sea ice classification (e.g., Ressel et al., 2016), iceberg detection (Dierking and Wesche, 2014), and oil spill recognition (e.g. Brekke et al., 2014).

Another approach in SAR image analysis for the presence of leads is based on linear

kinematic feature extraction (von Albedyll et al., 2023). In this approach a pair of SAR images is used to derive deformations in the overlapping areas, which may indicate existence of convergence or divergence areas. As leads are formed as result of the divergence in the sea ice cover, calculated divergence fields are used to detect leads.

Recently, convolutional neural networks (CNN) are applied more and more often for satellite image analysis. Bentes et al. (2018) applied CNN approach for ship classification on SAR images. An example of sea ice classification based on SAR images with CNN is described by Boulze et al. (2020). Malmgren-Hansen et al. (2021) introduces a method for combined SAR and passive microwave observations analysis for automatic ice chart production.

This work focuses on the tree main questions:

- Can leads be automatically detected on C-band SAR images?
- Do deep learning methods provide a more reliable lead maps?
- What insights do high resolution pan-Arctic lead maps provide about lead characteristics distributions?

This work develops an algorithm for automatic lead/sea ice semantic segmentation, hereafter is referred to as lead detection, with Sentinel-1 C-band synthetic aperture radar (SAR) images. The results are analyzed for the five winter seasons (1 November – 30 April) 2016–2021.

Chapter 2 provides a background on sea ice remote sensing (section 2.1 and section 2.2) and image processing techniques used in the study (section 2.3). The data used for the algorithm development is presented in Chapter 3. Chapter 4 describes a "traditional" machine learning approach to image analysis: gray level co-occurrence matrix analysis accompanied with random forest classification. In Chapter 5 a more robust algorithm based on a convolutional neural network is developed. This method is applicable Arctic-wide. Results are evaluated against 10 m resolution RGB images acquired with Sentinel-2. The developed automatic lead detection algorithm is based on analysis of backscatter amplitude and texture, and, therefore, thin ice and open water between ice flows may also be classified as leads. Finally, Chapter 6 presents lead area fraction, frequency of lead occurrence, and lead properties distribution in the Arctic Ocean, such as lead area fraction, size, length, width, and orientation.

2 Theoretical background

This chapter provides theoretical background on sea ice, synthetic aperture radar observations, and image analysis methods, which are used further in the thesis. Section 2.1 describes sea ice and leads properties relevant to the lead detection and the lead distribution analysis. Synthetic aperture radar (SAR) imaging basics relevant to sea ice observations are described in Section 2.2. Section 2.3 describes image processing methods, including machine learning techniques, used in the thesis.

2.1 Sea ice and leads

2.1.1 Definition of leads

Sea ice leads are often defined as cracks in sea ice cover. Sea ice and leads observations with optical, infrared, and microwave instruments rely on different physical properties. Therefore, leads can be defined in different ways for these instruments. While passive microwave measurements are very sensitive to thin ice, lead detection based on infrared measurements may also consider thin ice as leads. Measurements in the visible spectrum often can separate ice of 10 cm and thicker from water, thinner ice is recognizable depending on presence of snow cover, image resolution, and image processing methods. Active microwave measurements may identify thin ice as leads, depending on wind conditions and acquisition geometry, more details are provided in Section 2.2. In addition to that, several definition of a lead can be found in literature (Weeks, 2010). According to the World Meteorological Organization (WMO) a lead is a "fracture or passage-way through sea ice which is navigable by surface vessels", fractures are defined as "break[s] or rupture[s] through very close ice, compact ice, consolidated ice [...] resulting from deformation processes. Fractures may contain brash ice and/or be covered with nilas and/or young ice" (World Meteorological Organization, 2014). Although leads are often described as elongated areas with open water, throughout this study the shape of detected objects is not considered, unless it is explicitly specified. In this study, leads are considered in the WMO definition, as described above.

2.1.2 Sea ice

Sea ice separates warm ocean from cold atmosphere and regulates heat, gas, and water vapor exchange. Sea ice surface has a higher albedo compared to open ocean and, therefore, decrease the amount of solar radiation absorbed by the surface. In winter sea ice with snow cover is nearly perfect black body and, thus, radiates heat into space. As a result, sea ice is an important component of the world climate system.

Sea ice is essentially frozen sea water. It has crystal the structure of fresh water ice with saline water and air inclusions, which are often referred to as brine pockets and air pockets. The salinity of water inside brine pockets is usually higher than that of sea water and depends on temperature of the ice. Brine salinity at the equilibrium state with the surrounding ice can be described with an empirical equation derived by Notz and Worster (2009) from the measurements done by Assur (1960), the equation is valid in the range between 0°C and –22°C:

$$S_{br} = -21.4T - 0.886T^2 - 0.0170T^3$$

where S_{br} is brine salinity and T is brine temperature. Since temperature of sea ice varies with its depth, the salinity of brine inclusions and the brine content varies with the surrounding ice temperature. Bulk salinity of sea ice is typically 3–4 times lower than the salinity of water it is formed from (Weeks, 2010). As ice freezes, brine is partly trapped in the ice, but the major part of it is expelled into the underlying water. Brine content, in turn, influences the sea ice backscatter during active microwave measurements and the sea ice emission observed with microwave radiometers.

2.2 Active microwave observations of sea ice

A range of satellites is used for observations in the Arctic, as described in the Introduction. Main instruments on board of these satellites are split into two categories: passive and active. Active instruments emit radiation and measure the backscattered fraction of that, passive instruments rely either on the emission by an observed object, or on other emission source, radiation from which is reflected or scattered towards the instrument receiver. Satellites carrying cameras for visible and infrared spectrum, as well as microwave radiometers fall into the passive instrument category. Examples of active measurements are scatterometers, altimeters, and synthetic aperture radars.

An advantage of instruments that work in the microwave spectrum is their independence on cloud coverage, little influence of weather conditions, especially at frequencies below 15 GHz (Ulaby and Long, 2014), and independence from sunlight. As Arctic is often covered with clouds and is not enlighten by sun in winter, microwave satellites

are the major source of year-round observations of sea ice. Although passive microwave satellites cover the entire Arctic daily, they provide measurements at a relatively low resolution, which is usually 3 km and coarser (depending on frequency). Active microwave sensors, on the other hand, can provide observations with significantly higher spatial resolution. Typical resolution of Synthetic Aperture Radar (SAR) images ranges from a few meters to 50 meters. However, the temporal resolution has been one of the shortcomings for SAR instruments. With the launch of Sentinel-1 SAR mission it became possible to cover a major part of the Arctic Ocean in 1–3 days. Radarsat Constellation Mission is further improving the temporal and spatial coverage with SAR.

2.2.1 Synthetic Aperture Radar (SAR)

Synthetic Aperture Radar (SAR) is an active microwave imaging system which provides high resolution microwave observations with a typical pixel size of 5 to 50 meters, depending on swath width. Satellite-borne SAR is an active side looking system that makes overlapping backscatter measurements of a stationary target and combines them into a single higher-resolution image, effectively synthesizing a large aperture with a small antenna. When the overlapping measurements are done with coherent pulses, a sequence of echoes can be processes coherently just as if they originated from a set of many stationary antennas working together to form a single large antenna. SAR acquisition geometry is shown in Figure 2.1. A SAR instrument with an antenna follows the satellite track, this direction is referred to as azimuth direction. Various points within the instrument footprint along the azimuth direction are resolved through the doppler shift analysis. To estimate the doppler shift the target is assumed to be stationary or moving at a speed negligible relatively to the speed of the satellite. Along the azimuth direction, the echo return from objects in the front part of the beam are Doppler shifted to higher frequencies, while echoes from the aft part of the beam are shifted to lower frequencies. For a given target the return signal will change in frequency as the antenna footprint moves through the target. The direction perpendicular to the satellite track is called range direction. Points within the radar footprint along the range direction could be resolved by measuring the echo delay. However, in satellite-based SAR a range compression technique is used. Instead of a short pulse of a fixed frequency, a linear frequency-modulated pulse is transmitted. The transmitted pulse is, therefore, basically encoded, so that single echoes are distinguished in the combination of overlapping return signals.

Various frequencies are used to build up satellite-based SAR sensors. C-band (5.4 GHz) is one of the most common frequencies (RADARSAT, RADARSAT-2, Sentinel-1), L-band (1.4 GHz) is used by ALOS and ALOS-2, X-band (9.6 GHz) is used by TerraSAR-X.

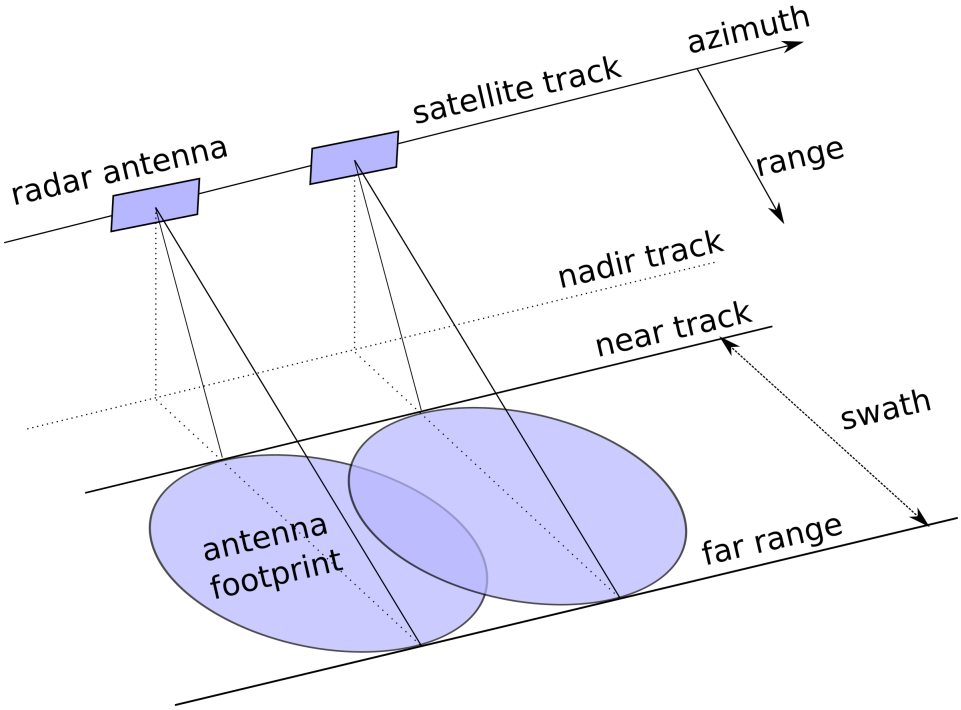

Figure 2.1: SAR acquisition geometry

Instrument frequency is one of the parameters that influences image resolution, lower frequency would have lower resolution under the same conditions. In addition to this, lower frequency bands have higher penetration depth in sea ice (Ulaby and Long, 2014).

Several polarization options are used in SAR measurements. The signal can be emitted with horizontal or vertical polarization. Both the horizontal and vertical components of the backscatter can be measured. This gives in total four values for backscatter intensity: HH, HV, VV, VH. The four values provide complimentary information about scatterers. To increase spatial coverage, some satellite observations are done with only one (HH or VV) or two (HH+HV or VV+VH) polarization combinations. Some satellites like Radarsat-2, Radarsat Constellation Mission, TerraSAR-X are capable of measuring all four components. This observation mode is called fully polarimetric as the four components fully describe backscattering properties of a media. Recent satellites also introduced a compact polarimetric mode, when the emitted signal has circular polarization, both the horizontal and the vertical components of backscatter are measured.

2.2.2 Sea ice and open water backscatter on SAR images

There are two major scattering mechanisms that define SAR backscatter: surface scattering and volume scattering illustrated in Figure 2.2. Volume scattering is the scattering occurring on particles within a media, it regulates penetration depth of microwaves. Therefore, physical properties of upper layers of sea ice influence the volume scattering.

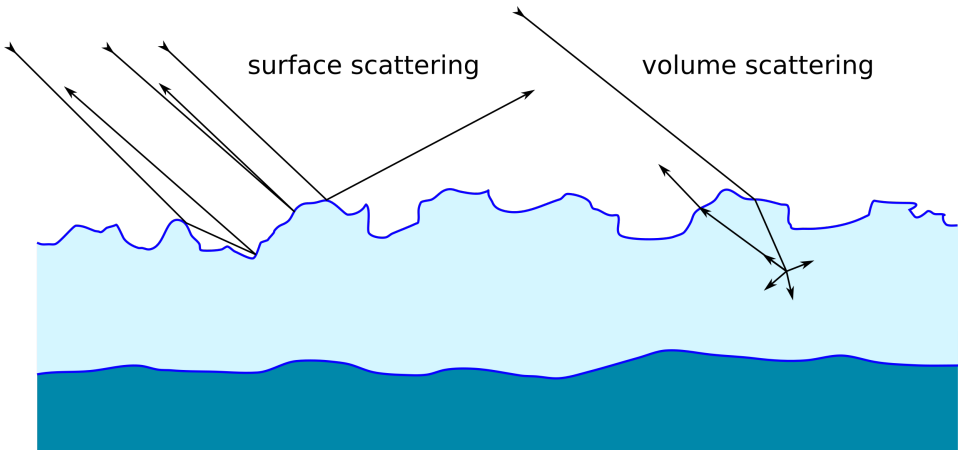

Figure 2.2: Surface and volume scattering

A typical microwave penetration depth in first year is between 7 cm and 30 cm in C-band (Ulaby and Long, 2014), while for multiyear ice it is between 25 cm and 50 cm. Surface scattering takes place at an interface between two media, e.g. the ice–air, snow–ice, or ice–water interfaces. In case of C-band sea ice observations, upper ice interface with air or snow is of most importance as 5.5 cm microwaves penetrate snow surface. When sea ice thickness is below the penetration depth, ice–water interface also contributes to backscatter. Surface scattering depends on surface roughness.

On the upper sea ice interface, the major fraction of the surface scattered microwave radiation returning back to the SAR instrument experience single reflection, which does not change polarization. Therefore, the polarization of the echo is same as the polarization of the transmitted microwave radiation. Volume scattering, on the other hand, changes polarization as the result of multiple scatterings within sea ice. As the result, backscatter in SAR cross-polarization bands mostly contain information about volume scattering of the observed medium, while SAR backscatter in co-polarization bands contain more information about surface scattering.

Dark and bright leads

Microwaves do not penetrate water, therefore an open water surface is a specular scatterer. Under calm water conditions SAR signal is specular reflected from the water surface resulting in low backscatter. A similar process takes place when sea water is covered with a thin smooth sea ice, that is much thinner than the penetration depth. SAR transmitted signal is specular reflected at the ice–water interface, volume scattering does a small contribution to the backscatter which is often within the SAR uncertainties. In these cases, open water leads and leads refrozen with thin sea ice, appear dark on SAR images. This case is further referred to as *dark leads*.

On the other hand, in case of wind-roughened surface or thin rough sea ice backscatter in the SAR co-polarization channel may have a high backscatter, depending on the acquisition geometry and orientation of waves, as rough water surface may scatter a significant amount of microwave radiation back in the direction of the instrument. Although the co-polarization channel will show high backscatter, the cross-polarization channel will still show low backscatter. This case will further be called *bright leads*.

2.3 Selected image processing techniques

This section provides descriptions of the image processing techniques and machine learning methods used further in the study. Gray level co-occurrence matrix described in Section 2.3.1 and Random forest classification described in Section 2.3.2 are the main concepts for the lead detection algorithm described in Chapter 4. Morphological skeletonization (Section 2.3.3) and watershed segmentation (Section 2.3.4) are used for lead filtering in Section 4.1.5. Convolutional neural networks (Section 2.3.5) contains basic information on deep learning methods, used for lead detection algorithm described in Chapter 5.

2.3.1 Gray level co-occurrence matrix (GLCM)

Gray level co-occurrence matrix (GLCM) calculation is one of the ways to represent image texture. Characteristics of GLCM suggested by Haralick et al. (1973) are often used to image classification purposes. GLCM is essentially a two dimensional histogram of an image, that shows how often pixels with certain brightness appear next to each other. Calculation of a GLCM matrix is illustrated in Figure 2.3. Each value of the GLCM matrix shows how many times pixel with brightness values given with the i_{th} row and j_{th} column appear next to each other on the input image.

An example of the resulting GLCM is shown in Figure 2.4. The input image in Figure 2.4a has the same average brightness values in the four regions with different texture. Each of the two boxes, the red and the blue, have same average brightness, but GLCM calculated for the two regions differ, as illustrated in Figure 2.4b and Figure 2.4c. As the results, characteristics of GCLM can be used to discriminate areas with different texture. To describe the matrix P with elements $p(i, j)$ the following parameters are suggested by Haralick et al. (1973):

- angular second moment

$$f_1 = \sum_i \sum_j (p(i, j))^2$$

1	1	1	0	3
1	1	0	3	2
1	0	3	2	0
0	3	2	0	0
3	2	0	0	0

a – input matrix

	0	1	2	3
0	3	0	0	4
1	3	3	0	0
2	3	0	0	0
3	0	0	4	0

b – GLCM of the input matrix

Figure 2.3: Gray level co-occurrence matrix (GLCM) calculation: *a* is the input matrix (image), *b* is the result matrix. Each value in the result matrix shows how many times two pixels with brightness values given by the row and the column appear next to each other on the input image (matrix).

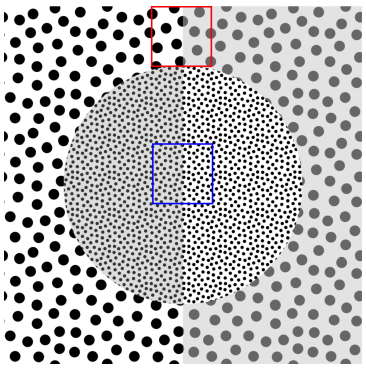

a – input image

	0	1	2	3
0	24607	336	228	1594
1	339	26251	766	1945
2	236	776	7687	1613
3	1602	1949	1599	10080

b – blue box GLCM

	0	1	2	3
0	27115	118	78	606
1	118	28299	302	863
2	78	302	10646	515
3	609	857	518	10584

c – red box GLCM

Figure 2.4: Example of GLCM matrix, *a* initial image has four gray levels, *b* GLCM for the blue rectangle, *c* GLCM for the red rectangle. Although average brightness of the image *a* is same for the blue and the red rectangle, GLCM are different. Therefore, GLCM characteristics can be used to discriminate between the regions.

- contrast

$$f_2 = \sum_{n=0}^{N_g-1} n^2 \sum_{\substack{i=1 \\ |i-j|=n}}^{N_g} \sum_{j=1}^{N_g} p(i,j)$$

- correlation

$$f_3 = \frac{\sum_i \sum_j (ij) p(i,j) - \mu_x \mu_y}{\sigma_x \sigma_y},$$

  μ_x, μ_y, σ_x, and σ_y are the means and standard deviations of p_x and p_y, where

$$p_x(i) = \sum_{j=1}^{N_g} P(i,j)$$

  N_g is number of distinct gray levels,

$$p_y(j) = \sum_{i=1}^{N_g} p(i,j)$$

- sum of squares (variance)

$$f_4 = \sum_i \sum_j (i-\mu)^2 p(i,j)$$

- inverse difference moment (homogeneity)

$$f_5 = \sum_j \sum_j \frac{1}{1+(i-j)^2} p(i,j)$$

- sum average

$$f_6 = \sum_{i=2}^{2N_g} i p_{x+y}(i)$$

  where

$$p_{x+y}(k) = \sum_{\substack{i=1 \\ i+j=k}}^{N_g} \sum_{j=1}^{N_g} p(i,j), k = 2, 3, ..., 2N_g$$

- sum variance

$$f_7 = \sum_{i=2}^{2N_g} (i - f_8)^2 p_{x+y}(i)$$

- sum entropy

$$f_8 = -\sum_{i=2}^{2N_g} p_{x+y}(i) \log(p_{x+y}(i,j))$$

- entropy

$$f_9 = -\sum_i \sum_j p(i,j) \log(p(i,j))$$

- difference variance

$$f_{10} = \text{variance of} p_{x-y}$$

where

$$p_{x-y}(k) = \sum_{\substack{i=1 \\ |i-j|=k}}^{N_g} \sum_{j=1}^{N_g} p(i,j), k = 0, 1, ..., N_g - 1$$

- difference entropy

$$f_{11} = -\sum_{i=0}^{N_g-1} p_{x-y}(i) \log(p_{x-y}(i))$$

- information measure of correlation

$$f_{12} = \frac{HXY - HXY1}{\max(HX, HY)}$$

$$HXY = -\sum_i \sum_j p(i,j) \log(p(i,j))$$

$$HXY1 = -sum_i \sum_j p(i,j) \log(p_x(i) p_y(j))$$

HX and HY are entropies of p_x and p_y.

These parameters, describing GLCM matrix, are then used as input features for image classification.

2.3.2 Random Forest classifier

Random Forest classifier is an ensemble method, often used in machine learning. It is based on a set of decision trees with random feature subspace and bootstrap aggregating applied. These concepts are described below.

Decision trees

Decision tree is a simple method often used in machine learning to learn and predict an outcome from a set of input observation. Decision tree is a hierarchal model that has a tree-like structure of decisions and their possible results. Each internal node splits data into subsets based on an input feature in such a way, that each subsets in a leave of the decision tree can be attributed to one of the classes of the data.

Random feature subspace

A single classification algorithm can be replaced with an ensemble. If every member of the ensemble provides same result, no improvement in the classification quality takes place. However, if every single classification in an ensemble is different, the result of the ensemble classification can be better compared to any single classification. To decrease correlation between classifiers in an ensemble, the idea of random feature subspace is employed. In case decision trees are used as a basic algorithm for an ensemble, every decision tree in an ensemble uses a random subset of input features during training and prediction, that is every tree has is own feature subspace.

Bootstrap aggregating (bagging)

Bootstrap aggregating, often referred to as bagging (**b**ootstrap **agg**regation) is a machine learning method, which suggests to sample a dataset (with replacement) into random sub datasets. It creates data subsets that are independent on each other. The method is often used in ensemble methods, where each learning algorithm of the ensemble is trained on a random independent data subset. After that, results of single learning algorithms are merged through a voting procedure.

The bagging method improves stability and accuracy of ensemble methods. It is applied to ensemble methods based on decision trees, resulting in the Random Forest classifier. Random Forest classifier is an ensemble of decision trees with random feature subspace and bagging applied. This means that every tree learns on a random subset of features and a random subset of data. In this way single trees of a forest have low correlation, and, therefore, provide a better classification result as the ensemble approach.

2.3.3 Morphological skeleton

Morphological skeleton is an extension to morphological operations, which is based on morphological erosion and opening. Morphological skeleton of a shape is a thin version of the shape, calculated with morphological operators as described by Zhang and Suen (1984). Pixels of a morphological skeleton are equidistant from the boundaries of the shape.

2.3.4 Watershed segmentation

Watershed segmentation is an image processing algorithm used for separating different objects suggested by Najman et al. (1994). It is defined for a gray scale image, where pixel brightness is considered as "elevation" over the zero level. The algorithm treats

images as topographic maps. Seeds used in the algorithm are essentially water sources that grow by flooding the elevation map. Each source has its own label, segments growing from each source have, therefore, their own labels.

2.3.5 Convolutional neural network

Convolutional neural network (CNN) is one of the common algorithms in the field of deep learning, used for image analysis. CNN is an algorithm that extends the idea of neural networks, used in machine learning for classification and regression tasks, to images. The major difference from traditional machine learning methods (like support vector machine, random forest, k-nearest, xgboost) is that features used for image classification are not precalculated, but are part of the neural network. This way, neural network is not only trained to find the optimal combination of precalculated features, but also to adjust the classification features in a way, that they describe the input data the best. It is achieved by a combination of different layer types in a CNN model. Below are short descriptions of the layer types used in this study.

Convolutional layers

Convolutional layers are the core technique of convolutional neural networks. Each layer creates a set of convolution kernels of a given size and convolve these kernels with the layer input to produce a tensor of outputs with layer responses to the kernel. A typical size of convolutional layer in deep leaning is 3x3 pixel. Larger kernels can be represented as a set of smaller kernels applied one by one, for instance, a 5x5 convolutional kernel is often replaced with a sequence of two 3x3 convolutions, which requires less computations.

Multi scale convolutions and pooling layer

A convolutional layer typically has a small kernel size. To look on a larger scale, CNN model has to look at a wider surrounding. This can be achieved by increasing size of convolutional kernel, but computational complexity of large convolutional layers grows exponentially. Instead a pooling layer is used. This layer decreases resolution of input image by a factor (often by a faction of two). If a mean value of a region is used for output, the layer is referred to as average pooling, and max pooling – if a maximum value of a region goes to output. When a convolutional layer is applied to the output of a pooling layer, it essentially covers a larger surrounding by a little computational effort compared to a larger convolutional kernel that covers same area.

Nonlinearity and Rectifier Linear Unit (ReLU)

An output of a single fully connected layer in a convolutional network is essentially a linear combination of its inputs. To represent nonlinear dependencies multiple layers are usually used. However, a combination of linear combination is also a linear combination unless a nonlinear function is applied in-between. Rectilinear unit (ReLU) is one of the commonly functions introducing nonlinearity in neural networks. The output of ReLU is equal to the input in the case input is positive and zero otherwise.

$$ReLU(x) = \begin{cases} x, x > 0 \\ 0, x <= 0 \end{cases}$$

Feature independence and dropout layer

Often, in a neural network every output of one layer is connected to every input of the next layer. Such layers are called fully connected. However, in convolutional neural networks it is sometimes desirable to skip some of those connections to avoid model overfitting. This is done through a dropout layer. A dropout layer drops a specified fraction of input to output connections.

Output probabilities with softmax function

Softmax function, also often referred to as normalized exponential function, converts a set of real numbers into a probability distribution of the set. It is often used at the last layer of a neural network to normalize the output to a probability distribution. Probability $\sigma(x)_i$ for each number x_i in an input set consisting of K values is calculated with

$$\sigma(x)_i = \frac{e^{x_i}}{\sum_{j=1}^{K} e^{x_j}}$$

Loss function

Training of a supervised neural network is essentially the process of function minimization. The function that is being minimized is called loss function. One of the most often used loss function, cross-entropy loss function, calculates cross-entropy between the labels p_i and predictions q_i for a set of values size of K. It is defined with

$$H(p, q) = -\sum_{i=1}^{K} p_i \log q_i$$

Kernel regularization

Kernel regularization is a method in convolutional neural networks that decreases chance of model overfitting. Additional value is added to the loss function that is minimized during model training, which describes the variability of values in a convolutional kernel. For instance, it can be calculated with L1 (sum of absolute values) or L2 (square root of sum of squares) metrics. This reduces unnecessary large span of values in convolutional kernels.

3 Data

This chapter describes the data used in the present thesis. The major data sources for the study are Sentinel-1 SAR scenes described in the Section 3.1. Section 3.2 describes optical images taken with Sentinel-2 satellites which are used for evaluation purposes. Finally, Section 3.3 describes sea ice concentration maps derived from AMSR2 passive microwave instrument by Spreen et al. (2008) which are used as an Arctic wide sea ice mask.

3.1 Sentinel-1 SAR images

Sentinel-1 is a satellite constellation that currently consists of two satellites launched in 2014 (Sentinel-1A, operational) and 2016 (Sentinel-1B, non-operational since December 2021) with a C-band SAR as primary instrument. The satellites are launched at a sun synchronous orbit, both share the same orbital plane with a 180° phase difference. The constellation with two satellites has a six day repeat cycle, tree day repeat frequency at equator and one day repeat frequency at the Arctic. The instrument on board of the satellites has four modes: strip map, interferometric (IW), extra wide swath (EW), and wave mode. The EW mode is the primary mode used over the Arctic ocean, therefore Sentinel-1 scenes collected in the EW mode are used in the present study. The EW mode has 40 m pixel size and 410 km swath width which consists of five subswaths. A typical size of a Sentinel-1 EW image is about 10000 by 10000 pixels. Currently the major amount of EW scenes is taken in dual-polarization (HH + HV) mode. Some areas are only covered with single polarization mode (HH) during the time when only one satellite of the constellation is operational.

Every scene contains thermal noise information in the auxiliary data, before July 2015 the thermal noise data does not contain a proper scaling factor. Therefore, the use of early Sentinel-1 data for automatic algorithms is challenging and, therefore, is avoided in the study. Since 18 March 2018 scalloping noise data is included in the supplementary information in addition to thermal noise. In this study the data from November 2016 to April 2021 winter seasons, 1 November – 30 April, is used as two Sentinel-1 satellites (a and b) were operating during this period providing a good spatial coverage of the Arctic. It should be noted that temporal coverage of various Arctic regions is not

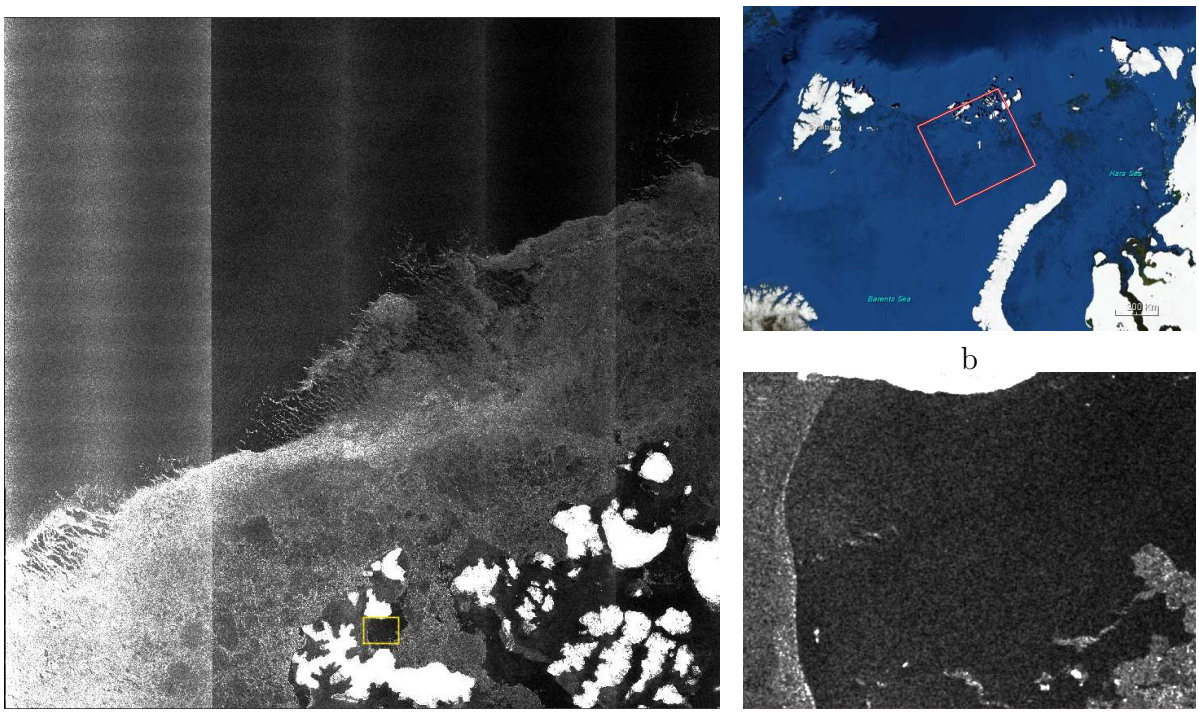

a b c

Figure 3.1: *a* – thermal and scalloping noise on the cross-polarization channel, *b* – location of the scene, *c* – speckle noise.

the same. The European Arctic (Fram Strait and Barents Sea) is normally covered daily with dual-band Sentinel-1 images. Coverage of Siberian Arctic and Beaufort Sea ranges from three to seven days. Therefore lead maps covering the entire Arctic are produced as a combination of three consecutive daily maps, more details are given in Section 4.1.7. Smaller regions (Fram Strait, Svalbard area, etc.) can be investigated at a higher temporal resolution (up to on a day basis). Sentinel-1 scenes are available at the Copernicus Open Access Hub (`https://scihub.copernicus.eu`) and Alaska Satellite Facility (`https://search.asf.alaska.edu`)

3.2 Sentinel-2 optical images

The second source of satellite data used in this study are observations from the Sentinel-2 satellite constellation carrying a multispectral instrument with 13 bands in the visual and near infrared spectral range. The constellation comprises two satellites on the polar sun-synchronous orbit, phased at 180° to each other. The multispectral instrument acquires images at 10 m resolution in the visible and 20 m resolution in the near infrared bands. Sentinel-2 images overlapping in space and time with Sentinel-1 scenes are used in the study to evaluate the results of the lead detection algorithm. For this RGB (red: 2nd band, 492 nm; green: 3d band, 560 nm; blue: 4th band, 665 nm) Sentinel-2 images with

a – Sentinel-2 RGB b – Sentinel-1 HH

Figure 3.2: Example of a Sentinel-2 and a corresponding Sentinel-1 HH image over marginal ice zone. Sentinel-1 SAR image is not affected with clouds cover in the bottom left part of images compared to optical Sentinel-2 image.

10 m spatial resolution are generated. Sentinel-2 scenes are available at the Copernicus Open Access Hub (`scihub.copernicus.eu`).

An example of Sentinel-2 RGB image and a corresponding Sentinel-1 SAR image are shown in Figure 3.2. Images are taken over marginal ice zone, both capture sea ice (top part of images) and open ocean (bottom part of images). Left side of the Sentinel-2 image is cloud-covered, while radar sees through clouds.

3.3 AMSR2 sea ice concentration

AMSR2 is a microwave radiometer instrument on board of the GCOM-W1 satellite launched by Japan Aerospace Exploration Agency (JAXA) in 2012. It has six spectral bands: 6.9 GHz, 10.65 GHz, 18.7 GHz, 23.8 GHz, 36.5 GHz, 89.0 GHz. The polarization difference at 89 GHz is used to estimate sea ice concentration by Spreen et al. (2008). An example of sea ice concentration derived from AMSR2 data acquired over Arctic is shown in Figure 3.3a. A 15% threshold sea ice concentration is applied to these maps to derive a sea ice mask (Figure 3.3b) which is used to mask out open ocean further in this study.

The data is available at the data browser of the remote sensing of polar areas group of the University of Bremen (`seaice.uni-bremen.de`).

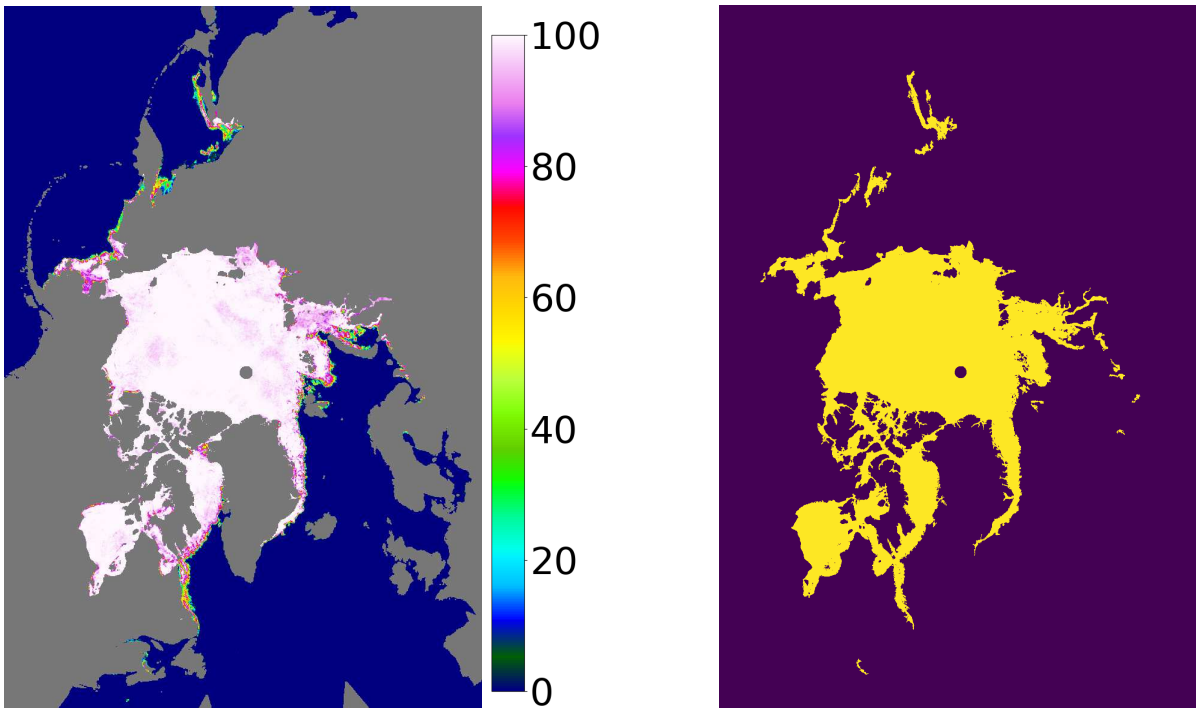

a – sea ice concentration

b – sea ice mask

Figure 3.3: *a* – Arctic sea ice concentration derived from AMSR2 data on 3 January 2019, *b* – Sea ice mask derived with 15% threshold on sea ice concentration *a*.

4 Automatic lead detection with Sentinel-1 images

In this chapter an algorithm for automatic lead detection with machine learning methods is described. Methods and results of this chapter are partly published in Murashkin et al. (2018); Murashkin and Spreen (2019).

The algorithm is developed for Sentinel-1 dual-channel C-band SAR scenes (co- and cross-polarized modes, HH and HV) acquired in the extra wide swath mode (EW). Data preprocessing including calibration is described in Section 4.1.1. The algorithm is based on traditional machine learning techniques for image analysis: gray level co-occurrence matrix (GLCM) texture features combined with polarimetric features (Section 4.1.3) are combined with the random forest classification as described in Section 4.1.4. As backscatter amplitude and texture analysis is the core of the algorithm, sea ice leads covered with thin ice may be classified together with open water between ice flows. There is no assumption on the shape of lead at this point, which means detected objects may have an arbitrary shape. The optimal number of texture features for lead classification is investigated and the precision–recall curve as a classification quality metric is evaluated in Section 4.2.1. Lead classification results are evaluated against 10 m resolution Sentinel-2 optical images in Section 4.2.3. Arctic-wide lead maps are produced from all Sentinel-1 scenes taken within a day over the Arctic ocean as described in Section 4.1.7. Two improvements to the core method are introduced as postprocessing steps: watershed-based binarization (Section 4.1.5) and shape-based filter (Section 4.1.6). The first one decreased the influence of small-scale noise. The second one considers the object shape to filter out patterns appearing due to residual noise on Sentinel-1 images. Results are evaluated (Section 4.2.4) on Arctic lead area fraction maps (12 km grid size) calculated from binary lead maps as described in Section 4.1.7. The data used for the automatic open water detection algorithm development are listed in Table 4.1. The flowchart of the lead detection algorithm is shown in Figure 4.1.

4.1 Methods

4.1.1 Data preprocessing

The data preprocessing procedure includes calibration and thermal noise removal, no data pixel detection at the edges of a scene, incidence angle correction, and speckle noise filtering. Normalized radar cross section (NRCS) σ values are calculated by applying thermal noise and calibration coefficients provided in the auxiliary data to the digital numbers (DN) provided in SAR scene channels, according to the equation given in the Sentinel-1 processing chain documentation (ESA, 2016):

$$\sigma = \frac{(DN^2 - noise)}{\gamma^2} \tag{4.1}$$

where DN is the backscatter amplitude provided in HH or HV channel, *noise* is the intensity of the thermal noise, and γ is a calibration coefficient, both *noise* and γ are provided in the meta data as look-up tables. As the next step the corrected backscatter is converted to dB by application of log_{10}. To prevent infinitely low values a value of $1 \,/\, \max(\gamma)$ is applied as the lowest value threshold. Backscatter values lower than the value are below the noise level. In this way, the thermal noise is removed from the SAR data, but so-called scalloping noise remains. The effect of the scalloping noise is mainly visible over the open ocean and therefore can be masked out with a sea ice mask. The sea ice mask is retrieved by applying a 15% sea ice concentration threshold for the ASI AMSR2 algorithm (Spreen et al., 2008), as described in section 3.3.

The border noise appears in two cases: (i) along the azimuth direction at very low and very high incidence angles, and (ii) at the beginning or the end of an acquisition. In both cases it is detected by median backscatter value analysis within the expected areas. If median value is below the noise level, the entire region is considered to contain no data. The borders are detected on both the HH and the HV channels, the largest of the two is set to be no data values for the scene.

Sea ice backscatter in the SAR data taken in HH polarization depends on the elevation angle and, consequently, incidence angle, which therefore must be taken into account. A linear regression on HH NRCS values versus incidence angle is employed. The regression coefficients are derived from a set of 16 Extra Wide swath mode Sentinel-1 scenes acquired over homogeneous sea ice covered areas. These products cover incidence angles between 18.9°and 48°, the entire range of incidence angles used in the Extra Wide swath mode. The resulting equation for the incidence angle correction is

$$\sigma_{corr} = \sigma + 0.213 \cdot (\theta - \min(\theta)) \tag{4.2}$$

Satellite	Sensor	Acquisition	Product type	Use in the study
Sentinel-1	SAR	1 Oct 2015; 07:36	S1A_EW_GRDM_1SDH	25% training, 75% test
Sentinel-1	SAR	28 Oct 2015; 14:32	S1A_EW_GRDM_1SDH	25% training, 75% test
Sentinel-1	SAR	31 Oct 2015; 16:35	S1A_EW_GRDM_1SDH	25% training, 75% test
Sentinel-1	SAR	4 Jan 2016; 02:01	S1A_EW_GRDM_1SDH	25% training, 75% test
Sentinel-1	SAR	1 Feb 2016; 11:15	S1A_EW_GRDM_1SDH	25% training, 75% test
Sentinel-1	SAR	3 Feb 2016; 22:30	S1A_EW_GRDM_1SDH	evaluation
Sentinel-1	SAR	30 Mar 2016; 13:09	S1A_EW_GRDM_1SDH	25% training, 75% test
Sentinel-1	SAR	2 Aug 2016; 13:18	S1A_EW_GRDM_1SDH	evaluation
Sentinel-2	optical	2 Aug 2016; 14:17	S2A_OPER_PRD_MSIL1C	evaluation
Sentinel-1	SAR	10 Apr 2017; 04:28	S1A_EW_GRDM_1SDH	evaluation
Sentinel-2	optical	10 Apr 2017; 12:06	S2A_MSIL1C	evaluation

Table 4.1: List of Sentinel-1 and Sentinel-2 products used in the algorithm development. The last column gives the fraction of the satellite scene, in percent, used for classification training and testing.

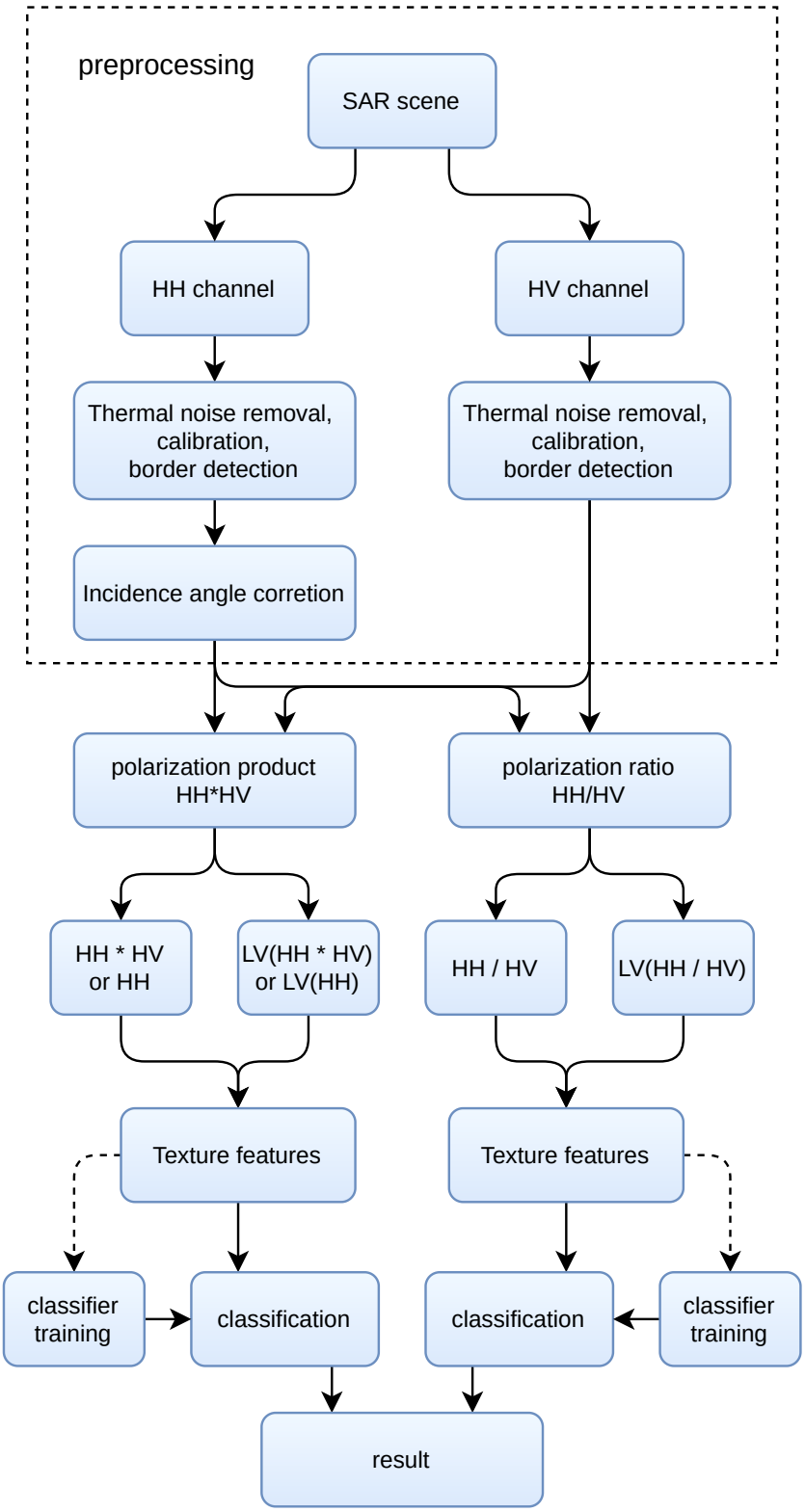

Figure 4.1: Processing flowchart; LV stands for Local Variability (image with background subtracted)

where σ_{corr} is the backscatter after the correction, given in dB, and θ is the elevation angle in degrees. Images taken in the HV polarization do not reveal a significant sensitivity to the incidence angle, therefore the correction is done for the HH channel only.

The last Sentinel-1 scene preprocessing step is speckle noise reduction. A bilateral filter is applied, which is an edge preserving filter known to have high performance in reducing speckle noise (Tomasi and Manduchi, 1998; Alonso-Gonzalez et al., 2013). The size of the square window for the filter is set to 5 pixels, the filter sigma for both the color and the coordinate space is set to 15. Larger window size typically improves filtering quality, but the computation time is increasing exponentially. At this stage the preprocessing of the Sentinel-1 data is finished.

4.1.2 Training data

In order to train the classifier a ground truth dataset is needed with correctly identified objects, i.e., in this case leads with thin ice or open water. A set of Sentinel-1 scenes covering two different typical lead appearance types: dark and bright leads (three scenes for each of the two cases) has been labeled manually, scenes are listed in Table 4.1. These scenes are taken from various times of the year, no scene from summer is used for training datasets because during the melt season melt ponds can have similar signature in SAR backscatter as leads with open water. To evaluate the results of the classification on independent data, two cases of overlapping Sentinel-1 SAR and Sentinel-2 optical data are used (Table 4.1). Although images in one of the cases were taken in August, there is no evidence of melt ponds presence on them. Hence, the melt season is excluded from the study.

Leads with open water or thin ice in most cases have low surface roughness and therefore have low backscatter values on both SAR polarizations, HH and HV (as described in more details in Section 2.2.2). They appear dark on the optical images used for evaluation as well. This case is represented in the first of the two evaluation datasets. Figures 4.2a,b, and c show the HH, the HV, and the product of SAR polarizations HH·HV, respectively, and Figure 4.2d the Sentinel-2 RGB image of the corresponding area taken in the visible spectrum. The time difference between the acquisitions is about 7 hours 40 minutes. Most areas covered with leads appear dark on all images. Only around edges of leads thin crushed ice with a high surface roughness can appear bright while on the image taken in visible spectrum the same thin crushed ice is transparent. The assumption for using the polarization product HH·HV is that when either the HH or the HV channel show low backscatter intensities, the polarization product has low NRCS values.

Leads with open water, however, can appear bright on the HH channel under high

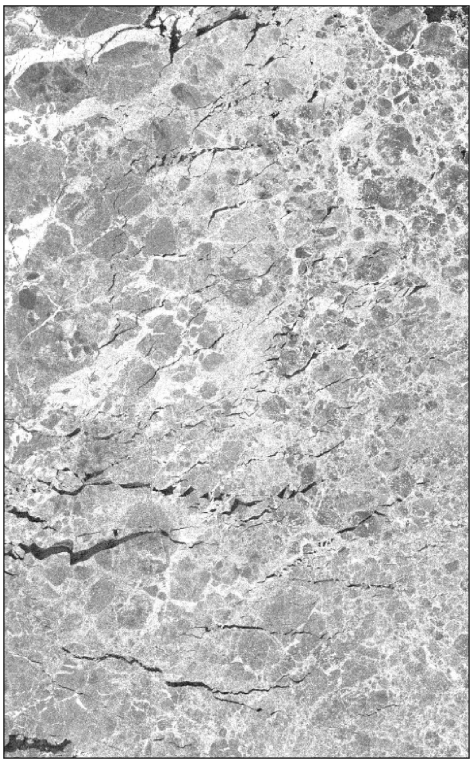

a – HH channel

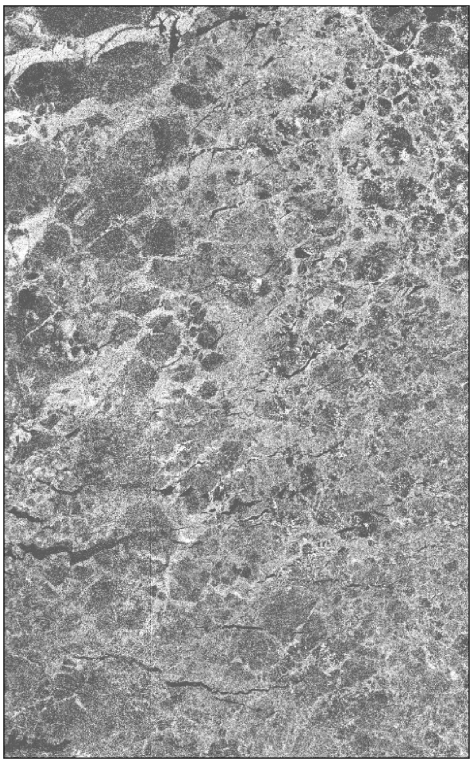

b – HV channel

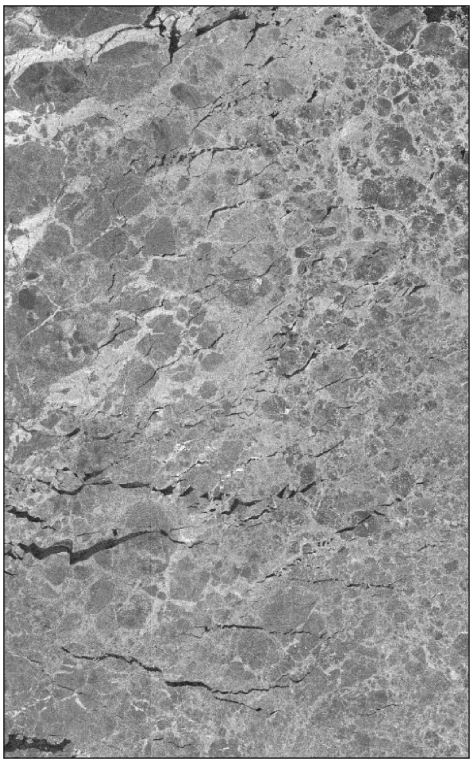

c – polarization product

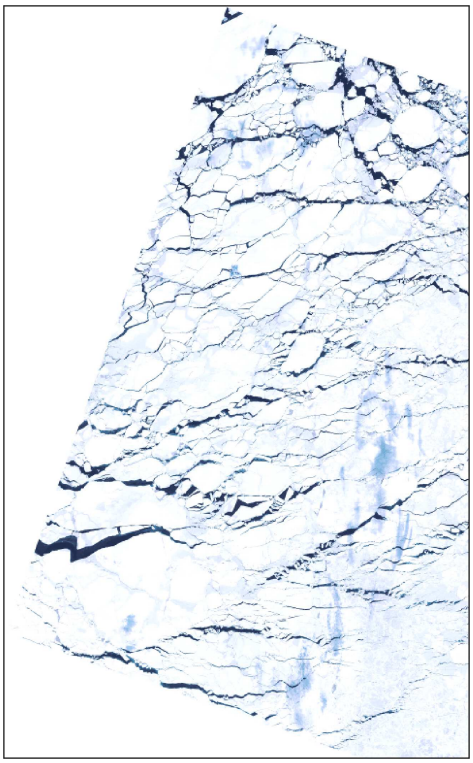

d – optical image

Figure 4.2: *a* and *b* are the HH and the HV channels, *c* is the polarization product – product of the HH and the HV channels (HH·HV) of the SAR scene taken on 10 April 2017, west of the Franz Josef Land; *d* shows Sentinel-2 RGB image taken on 10 April 2017 over the same area.

incidence angles if wind roughens the water surface (Scharien and Yackel, 2005). In the HV channel, leads appear dark under the same conditions. Refrozen leads with thin sea ice covered with frost flowers may have high backscatter in both the HH and the HV channels (Nghiem et al., 1997; Dierking, 2010; Isleifson et al., 2014) and therefore may look similar to pressure ridges in C-band SAR scenes. Leads with frost flowers are not taken into account in the classification to avoid confusion with ridges. Lead detection on the HV channel is more prone to errors since the backscatter intensity at the HV channel is low and often close to the noise floor. An example of the situation when leads have high HH polarization backscatter intensities is shown in Figures 4.3a, b, and d for Sentinel-1 HH, HV, and Sentinel-2, respectively. Leads that are clearly observed in the optical images have higher backscatter than the surrounding sea ice at the HH channel from SAR and lower backscatter in the HV channel. In the polarization ratio HH/HV leads appear bright if HH is high and HV is low.

To account for these two different conditions, the lead classification algorithm is split into two parts: the first one detects leads with low backscatter on both SAR channels and appear dark on images, are referred to as dark leads further. The second one is used for cases with high backscatter values at HH channel (compare also the two branches in the flowchart in Figure 4.1), referred to as bright leads further. As the last step both outputs are merged together to produce the final lead map.

Two cases of overlapping Sentinel-1 and Sentinel-2 data, presented in Figures 4.2 and 4.3, are used for the evaluation of the algorithm. Here leads are labeled on the SAR dataset by visual inspection, taking into account the corresponding optical Sentinel-3 images to confirm the validity of the selected leads.

For the training of the algorithm an independent set of Sentinel-1 scenes is used, scenes are listed in Table 4.1. They also represent the two cases for lead appearance, the leads appearing dark and the leads appearing bright in the HH channel respectively. Half of Sentinel-1 scenes are used to train the “dark lead” classifier and half scenes are used to train the “bright lead” classifier. Leads are identified and labeled manually without the additional support from optical data. The evaluation is performed on Sentinel-1 SAR images which overlaps with Sentinel-2 optical data shown in Figures 4.2 and 4.3.

4.1.3 Texture and polarimetric features

There are two methods to extend the feature space of the measured HH and HV backscatter intensities and improve object classification performance: polarimetric and texture features. Polarimetric features can be calculated for SAR products containing at least two out of the four Stokes vector components whereas texture features can be calculated for a single polarization scene. Here both approaches are combined for Sentinel-1 dual

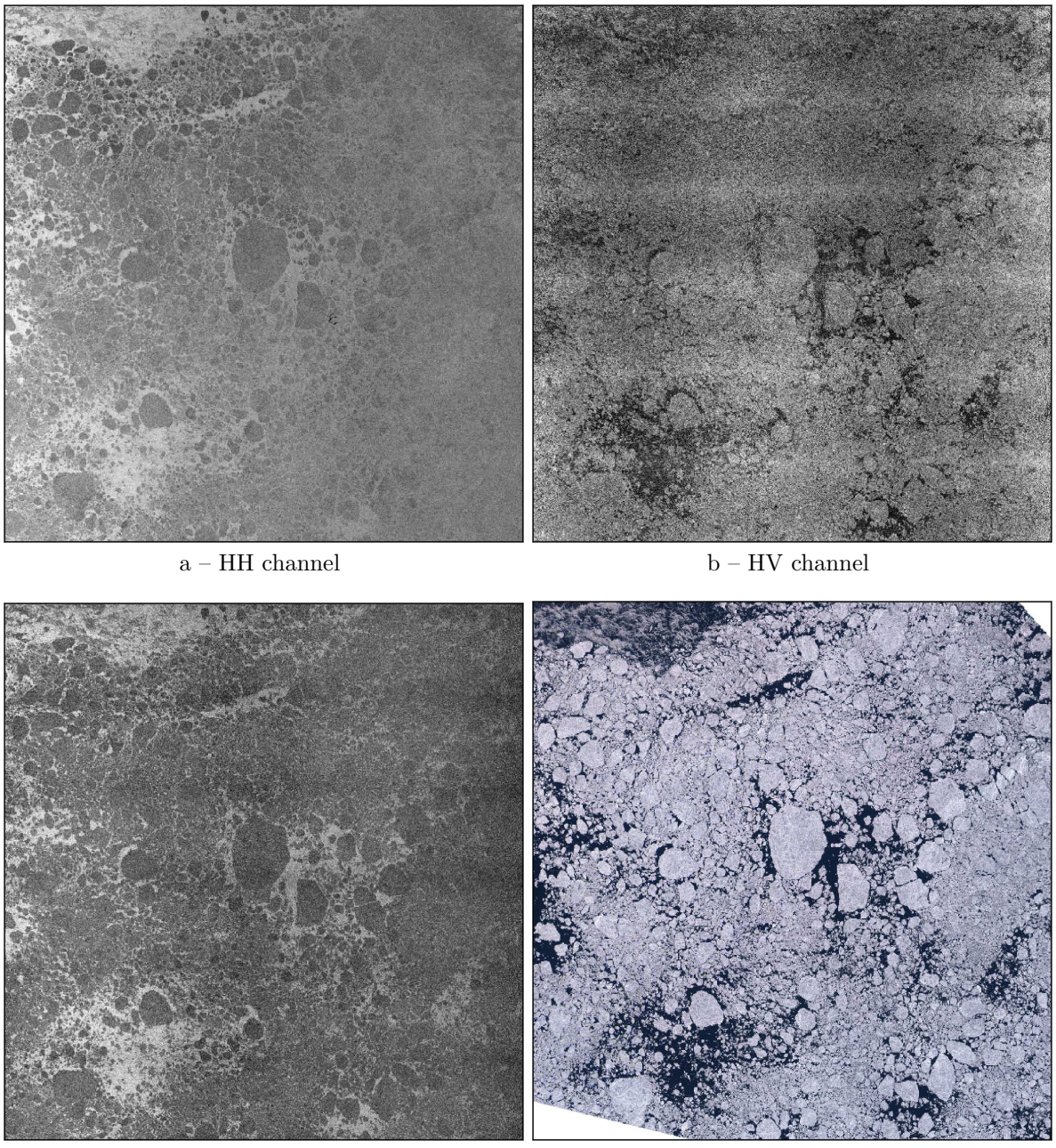

a – HH channel

b – HV channel

c – polarization ratio

d – optical image

Figure 4.3: *a*, *b* and *c* are HH, HV channels, and polarization ratio, respectively, of a Sentinel-1 SAR scene taken on 2 August 2016, between Svalbard and Franz Josef Land; *d* is Sentinel-2 RGB image taken on 2 August 2016 over the same area.

polarization data. Scenes taken with the Sentinel-1 EW mode over the Arctic waters contain co- and cross-polarized channels (HH and HV). As only the amplitude but not phase is available for this data source, the number of available polarimetric features is limited. In this study, the product HH·HV and the ratio HH/HV are used as polarimetric features. The co-polarization ratio HH/VV and real part of the co-polarization cross product is widely used for the SAR image classification e.g. Brekke et al. (2016). It have shown high performance in discriminating open water from sea ice performed by Ressel et al. (2016). In the absence of the VV polarization channel the HV polarization channel is used instead. The cross-polarization ratio was used for classification of SAR images by (Karvonen, 2014). Bright, wind roughened leads in HH channel appear dark in the HV (Figure 4.3), which will cause high values in HH/HV and this is the case to be detected with the polarization ratio. The classification for dark leads is based on the HH·HV product, which will be low if one of the channels is low, i.e., dark. However, because of the low signal to noise ratio in HV channel the classification based on polarization product is also compared with the classification based on the HH channel alone to quantify if there is a benefit from the use of both polarizations.

Therefore, the HH channel, the polarization product HH·HV and the polarization ratio HH/HV are used as input for the following texture analysis. Figures 4.2c and 4.3c show example images for the polarization product and polarization ratio, respectively.

Texture features based on the grey-level co-occurrence matrix (GLCM) are widely used for classification of SAR data (Haralick et al., 1973; Leigh et al., 2014; Liu et al., 2015; Zakhvatkina et al., 2017). The complexity of texture feature calculation depends on the size of the chosen sliding window and the number of grey levels of the input image. Here a discretization into 16 grey levels is chosen as a trade-off between conservation of details and computational cost. NRCS values split equidistantly into 16 groups between –29 Db and +4 Db for the HH channel and between –32 Db and –15 Db for the HV channel. GLCMs are then calculated for a sliding window of 9×-pixel size with 1-pixel step size. A bilinear weighting within the sliding window is applied, so that pixels which are closer to the middle of the window have higher weight for the GLCM computation.

The twelve GLCM features used in this study are listed in Table 4.2. Definitions of the features are given by Haralick et al. (1973). Some GLCM features depend on the image brightness (the value of the HH and the HV polarization product or ratio). This means the absolute value of the pixel brightness influences these texture features. Since leads are often darker than the surrounding sea ice, the difference between the original image and a low-pass filtered version of the image is calculated to show the small-scale backscatter variations. A bilateral filter with a 25×-pixel sliding window is applied to the preprocessed original image and subtracted from the non-filtered image. In this way, the local backscatter variability is emphasized and is used further as an additional

N	Texture feature
1	angular second moment (ASM),
2	entropy,
3	contrast,
4	sum of squares: variance,
5	inverse difference moment (homogeneity),
6	correlation,
7	sum average,
8	sum variance,
9	sum entropy,
10	difference variance,
11	difference entropy,
12	information measure of correlation.

Table 4.2: Twelve GLCM features are used in the study. Definitions of the texture features are given by Haralick et al. (1973).

information for the classification. Afterwards GLCM texture features are calculated both for (i) the original image and (ii) for the small-scale variations of the image. In this way, two sets of texture features are produced for each of two input polarimetric features (i) polarization product and (ii) polarization ratio, and for the HH channel, and further analyzed (see also flowchart in Figure 4.1).

4.1.4 Random Forest classification

The Random Forest classifier (Ho, 1998; Breiman, 2001) is used for the lead detection. It is an ensemble method, which constructs a set of decision trees. Each of these trees is trained on a different subset of data points and features. The decision made by each tree is weighted to provide the final result. The method has been proven to have good quality of classification and at the same time high computational speed. One of the advantages of the classifier is its internal metric for feature importance, which gives information on the frequency of use of each of the input features. Another advantage of the classifier is its capability to perform not only binary, but also probabilistic classification. The probability of pixels to belong to a class can afterwards be translated to binary classification based on a threshold. The default behavior is the use of a threshold of 50% probability. Different thresholds can be applied to adjust the result of classification. While there are several metrics to evaluate the quality of an algorithm, the most widely used metric is *accuracy* (equation 4.3 below). Although alone it might be unrepresentative for the case when the size of one class is considerably larger than the size of the other class. Leads usually occupy a few percent of sea ice area in the Arctic (Steffen, 1991), so that additional metrics should be used for quantifying the classification performance.

Precision and *recall* scores are defined by Fawcett (2006) and are used in the present study altogether with *accuracy*.

$$accuracy = \frac{TP + TN}{TP + FP + TN + FN} \tag{4.3}$$

$$precision = \frac{TP}{TP + FP} \tag{4.4}$$

$$recall = \frac{TP}{TP + FN} \tag{4.5}$$

where TP stands for true positive (pixels correctly classified as a lead), TN – true negative (pixels correctly classified as not being a lead), FP – false positive (pixels that are not leads but are classified as a lead), FN – false negative (pixels that are leads but are classified as "not lead") predictions. The sum $TP + FP + TN + FN$ equals to the total number of pixels in an image. *Accuracy* is the amount of correctly classified pixels over the total number of pixels. *Precision* is the amount of correctly classified pixels of the given class over the total number of pixels classified as the given class. Hence, $(1 - precision) = \frac{FP}{TP+FP}$ is the number of sea ice pixels misclassified as a lead over the total amount of pixels classified as leads. The *recall* rate characterizes how complete the classification is, that is the number of samples classified correctly over the total number of samples of this class. These three scores provide the needed information on the quality of a given class classification. They can aid to make decisions on how many features are needed for the classifiers.

To describe what probability threshold gives the best results for a probabilistic classifier, the receiver operating characteristic curve and the precision–recall curve are widely used (Fawcett, 2006; Davis and Goadrich, 2006). The receiver operating characteristic, for example, was applied for the lead detection algorithm described by Wernecke and Kaleschke (2015). Here the precision–recall curve is used to decide for an optimized binary threshold value for the Random Forest classifier. This will be presented in Section 4.2.2.

Two main classifier parameters influencing the classification quality and the computing time are the number of trees and the maximal depth of each tree. To choose the most suitable values for these parameters the six training SAR scenes, where leads were marked without support from optical data, have been used. The evaluation with the additional optical scenes will be presented in Section 4.2.3.

The two SAR datasets for the "dark" and the "bright" lead classifiers (three SAR scenes each) with manually identified leads have been randomly split into a training (25% of the data) and a test dataset (75% of the data). Two classifiers are trained on the scenes where leads appear dark in the HH channel: one is based on the HH

channel, another one is based on the HH·HV polarization product. Comparison for the two classifiers is presented in Sections 4.2.1 and 4.2.2. The third classifier is trained using the HH/HV polarization ratio based on the scene where leads appear bright in the corresponding HH channel. Each of the three classifiers are trained on the corresponding training dataset and then they are evaluated on the training and test datasets. A number of trees equal to 64 has been chosen for balance between efficiency and computing time. The maximal depth of trees was set to 15 to prevent overfitting and decrease computing time.

To decide on how many texture features give positive benefit for the classification quality and to remove features that are not needed a so-called Recursive Feature Elimination (RFE) is carried out. 12 texture features for the NRCS image, 12 texture features for the small-scale variations of the image, and the original (preprocessed) NRCS image itself altogether constitute 25 features which are used in the recursive feature elimination. The Random Forest classifier provides the feature importance rank for all features used in the lead classification. Recursively, now after each training and classification the number of features is reduced by one and the training and the classification started again. After every step the texture feature with the lowest importance according to the classifier's metric (i.e., the feature least used) is eliminated. Accuracy, precision and recall are calculated to estimate the classification quality of the algorithm on the given subset of features. The operation is repeated until one feature is left. To calculate the three quality metrics a binary classification based on 50% probability threshold is used. Based on this experiment the optimal number of features can be chosen, which is presented in Section 4.2.1.

4.1.5 Watershed-based binarization

The 50% threshold on probabilistic classification is the basic method to produce a binary lead map. In some cases, this approach is heavily influenced by the presence of noise on the original SAR images, especially in the areas covered with smooth new ice and thin first year ice with little amount of deformation features. Therefore, here a more advanced way to produce a binary lead mask from the probabilistic classification is developed. A flowchart of the procedure is shown in Figure 4.4.

To reduce the amount of classified object, i.e. leads, originating from noise patterns, objects that do not contain confident lead pixels are discarded. Only objects, which contain at least 2 pixels with high lead probability, are kept. To achieve this, the watershed segmentation algorithm suggested by Najman et al. (1994) is employed.

As the first step, two binarization thresholds are applied to each image: one corresponds to the normal binarization, the other one corresponds to high-confidence bina-

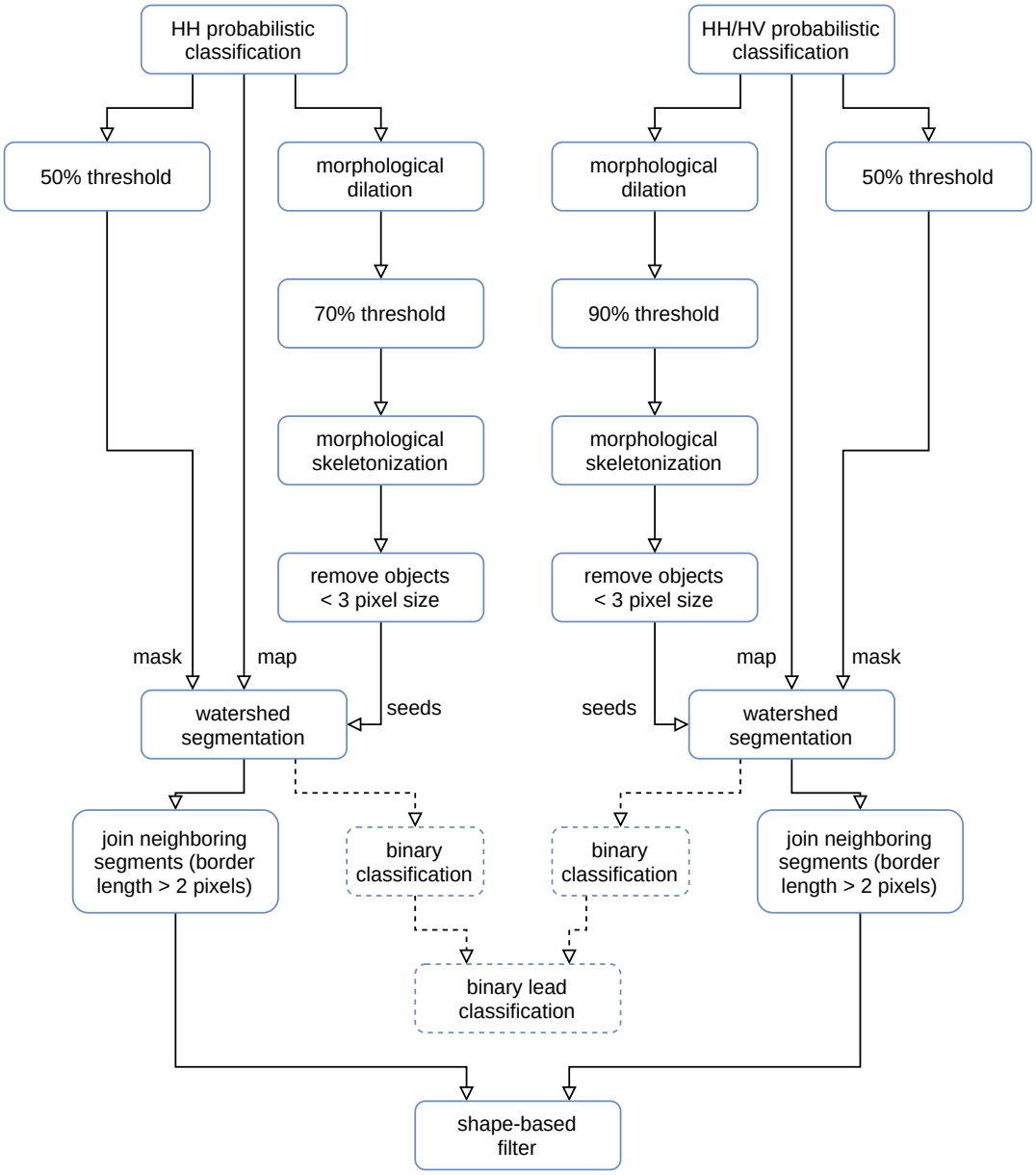

Figure 4.4: Binarization with watershed segmentation algorithm. Input are two probabilistic classifications: one based on the HH channel, the other one based on the polarization ratio. The two inputs are treated separately, results are merged at the final step. Seeds for the watershed segmentation are produced by applying morphological dilation followed by a strict threshold. The result is skeletonized and objects smaller than 3 pixels in size are removed. Binarization with 50% threshold is segmented with the watershed segmentation algorithm using found seeds.

rization. Empirically 50 % and 70 % thresholds have been chosen for the HH channel; 50 % and 90 % for the polarization ratio. The higher confident binarization threshold for the polarization ratio is chosen because of larger variations due to higher noise contamination in the cross-polarization channel compared to co-polarization HH channel. Before the higher threshold is applied, the probabilistic classification is extended with morphological dilation to connect adjacent segments at 1-2 pixel distance. The high-confidence lead pixels are used as segment seeds for the watershed segmentation algorithm. In order to produce the seeds a morphological skeletonization is applied to the high-confidence binary lead classification. Seed objects (sets of adjacent pixels) smaller than 3 pixels are filtered out. After that, the seeds are passed to the next step in the watershed segmentation algorithm. The lead probability map is masked with the binary lead map based on the lower, 50% threshold. This mask defines the maximum span for potential leads (as used in the previous section). To remove wrongly classified, noisy leads, the objects within this mask are now segmented by the watershed segmentation with seeds produced as described above.

As the result, clusters of pixels produced with the lower binarization threshold are preserved only if they contain pixels produced with the higher threshold value. When the watershed segmentation is applied, neighboring segments are joined together if the border between segments is at most two pixel long. The resulting segmentation is converted to a binary lead map, or it can be passed to the object shape analysis, described in the next section. Both cases are compared in result, Section 4.2.4.

4.1.6 Shape-based object filter

The watershed binarization filters out objects that do not contain any confident lead pixels. Nonetheless, some of the non-elongated object can be preserved as object shape is not taken into account. In order to filter out patterns appearing due to noise, shape-based filter is introduced. Each group of connected pixels of the binary lead classification described above is now considered as a single object. The shape of each object is described with a range of features listed below. First, there is a group of shape features related to the area of an object:

- *area* - total object area in pixels (number of pixels within the border of the object)
- *filled area* - object area in pixels, does not include holes that might be present within the object
- *hole area* - area (in pixels) of holes in the object (number of pixels of holes if presented in the object)
- *convex area* - convex hull area of the object in pixels
- *solidity* - *area* to *convex area* ratio

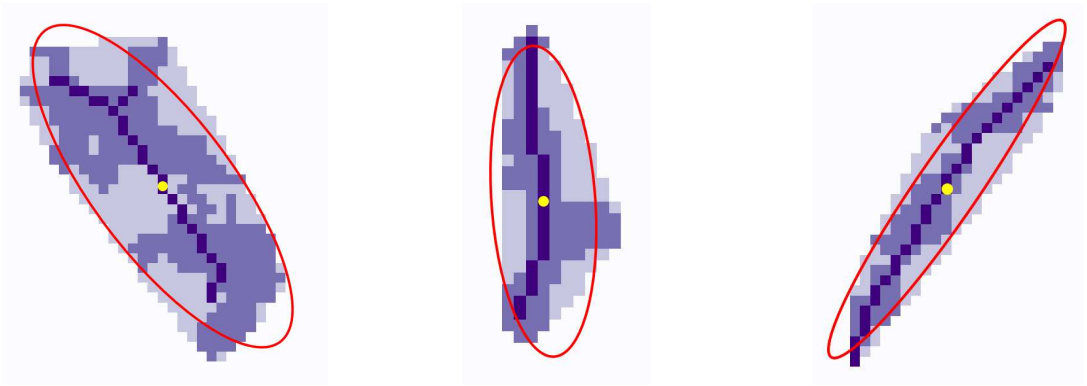

a b c

Figure 4.5: Object shape properties: original objects are shown in medium purple, light-purple corresponds to the convex hull area, dark-purple shows the morphological skeleton of the convex hull; object geometric center is shown with yellow dot. An ellipse approximating an object is shown in red. *a* represents an object appearing due to noise: large perimeter, presence of holes, some pixels of the morphological skeleton are outside of the segment. *b* and *c* are lead-like objects: have elongated shape and less border variations compared to *a*. Objects *b* and *c* would be kept while *a* would be removed by the shape filter.

- *perimeter* - border length of object in pixels
- *compactness* - *area* divided by *perimeter* squared
- *equivalent diameter* - diameter of a circle with same area as the object area

Second, every object is approximated with an ellipse (Figure 4.5) and the following ellipse characteristics are added to the shape analysis:

- *major axis length, a*
- *minor axis length, b*
- *eccentricity,* $e = \sqrt{1 - \frac{a^2}{b^2}}$
- *effective width* - ratio of object *area* to *major axis length*
- *ratio of area to product of major and minor axis lengths*

The shape descriptors above are calculated in accordance to Burger and Burge (2009).

A *morphological skeleton* (see Section 2.3.3)of the *convex hull* is calculated for each object (Figure 4.5) and the following features are considered as additional shape properties:

- *morphological skeleton length* in pixels
- *morphological skeleton interior pixels* - number of skeleton pixels contained by the object
- *morphological skeleton exterior pixels* - number of skeleton pixels that do not belong to the object

These object shape properties provide a tool to identify objects that are not leads and

mainly appear due to noise and filter them out. To create a classifier able to separate leads from noisy patterns, a training and test dataset consisting of around 2000 objects extracted from binary images has been created. The binary lead images are produced with the lead detection algorithm from Sentinel-1 SAR scenes (procedure described above in Sections 4.1.4 and 4.1.5). Only the objects which can be clearly recognized by their shape as leads are labeled *lead*. Thus, small objects that could not clearly be identified as leads or noise are not present in the dataset. For every object, a set of shape characteristics described above is calculated. Every object is manually labeled as a *lead* or *no-lead*. In Figure 4.6 distributions of shape features are shown for the dataset for objects labeled as *leads* and *no-leads* separately. It should be noted that some of the features are be correlated.

For every plot the feature distributions overlap, which means it is not possible to distinguish between correctly classified leads and misclassified leads with a single feature. To find the best combination of features that can perform the shape-based filtering, a Random Forest Classifier Ho (1998); Breiman (2001) is used. The Random Forest classifier is chosen for its performance and ability to work with input features that are not rescaled to have a zero mean value and a standard deviation of 1. The trained Random Forest classifier produces a binary label for each object in the case of two-class classification. In this case, *lead* and *no-lead* classes. Pixels of non-lead class are then masked out on the binary lead classification, lead pixels are kept. This way, the classifier works as a filter for *no-lead* objects.

4.1.7 pan-Arctic map generation

Lead detection is performed on single Sentinel-1 scenes in SAR geometry. Classification results for single scenes acquired during a single day are then projected to North Pole Stereographic projection (EPSG: 3413) and merged together into an Arctic-wide map. In case of scene overlap, older scenes are overlaid with the newer ones. The resolution of the Arctic-wide maps is identical to the resolution of classified scenes. After the scenes are merged, a land mask based on GSHHS data (Wessel and Smith, 1996) is applied. Then an open ocean mask based on AMSR2 sea ice concentration data (described in Section 3.3) is applied.

dark leads (HH channel, HH·HV)

bright leads (polarization ratio HH/HV)

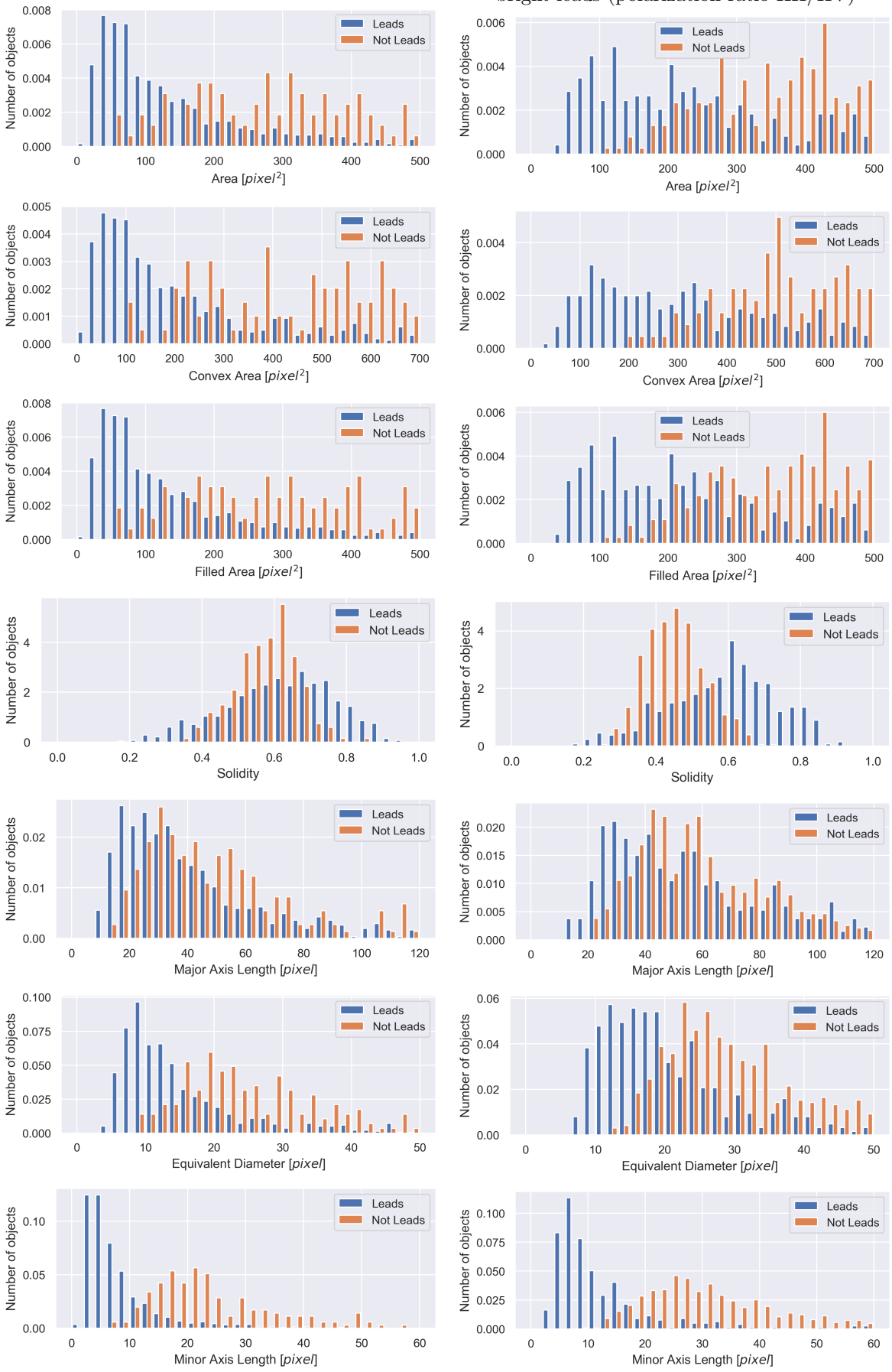

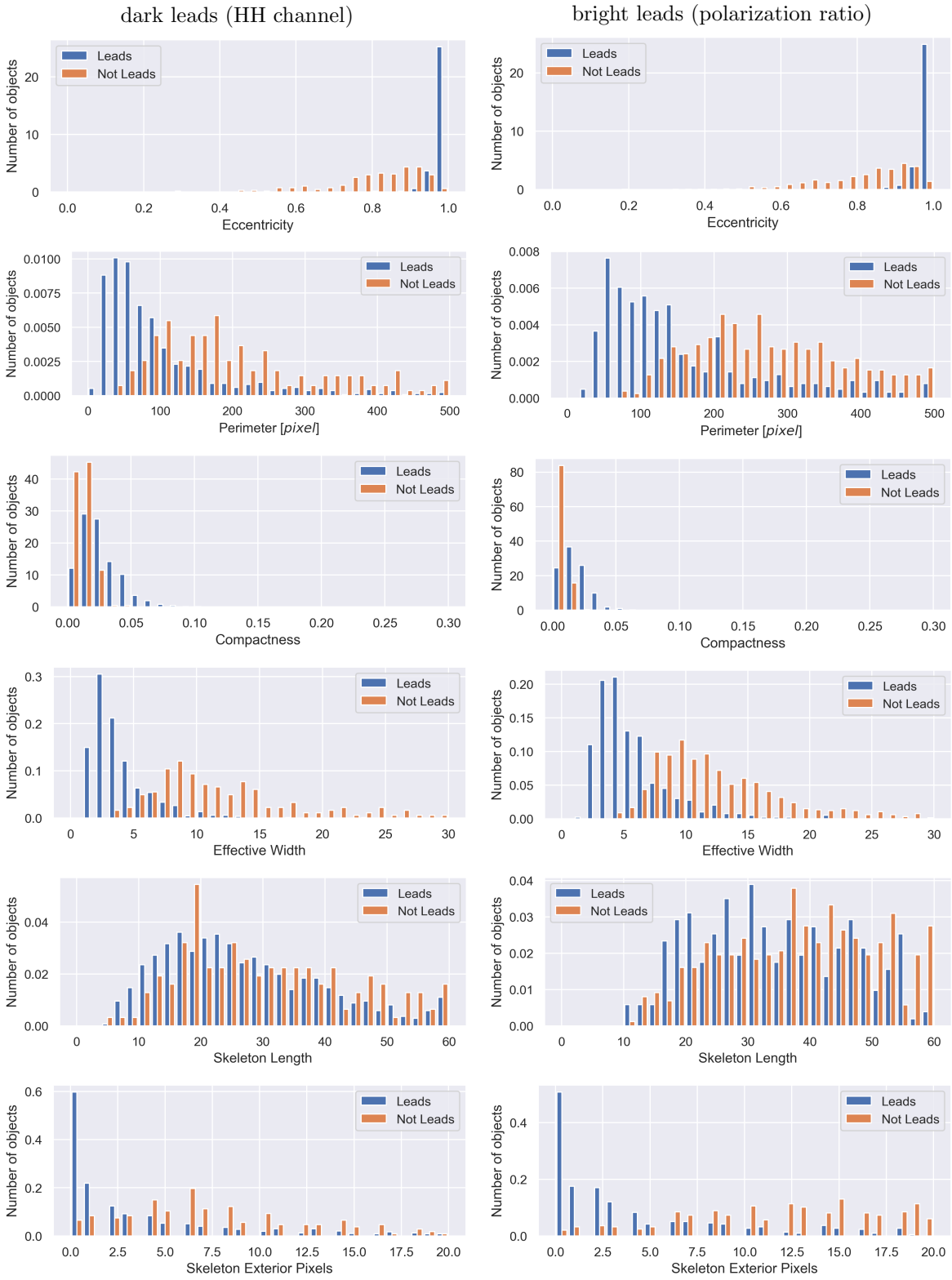

Figure 4.6: Distribution of object shape features for *lead* and *no-lead* classes in the manually labeled training/test dataset. Left column shows features for "dark leads" detected from the HH channel or polarization product HH·HV; right column shows features of "bright leads" detected from the polarization ratio HH/HV.

4.2 Results

4.2.1 Optimal number of texture features

The procedure for texture feature ranking described in the last section was carried out three times: one time the polarization product (HH·HV), the second one for the HH channel, the third one for the polarization ratio (HH/HV). The polarization product and the HH channel are used for the training dataset where leads appear dark and the polarization ratio on the training image with primarily bright leads. Table 4.3 lists the 25 texture features in the order they were eliminated for each of the three cases (i) the HH channel, (ii) the polarization product, and (iii) the polarization ratio.

Accuracy, precision, and recall scores in dependence on the number of features eliminated are shown in Figures 4.7a, 4.7b, and 4.7c, respectively. Dashed lines show accuracy, precision, and recall rates for the training set, solid lines are given for the corresponding metrics calculated on the test dataset. Blue lines stand for classification of the polarization product, green lines stand for classification of the HH channel (i.e., dark lead cases), and red for the polarization ratio (i.e., bright lead case).

Accuracies of the three classifications stay almost constant until the first 9 texture features are eliminated. A noticeable decrease in the classification accuracy appears after 16 texture features are eliminated for both the HH and the polarization product classifiers and after 17 for the polarization ratio classifier. This indicates that the first 9 texture feature for each of the tree classifiers (Table 4.3) can be eliminated without any harm for classification and as little as 3 to 8 texture features already can provide good classification results.

The precision and the recall rates of the HH channel and the polarization product classifiers follow corresponding accuracy trends, but show more variation in amplitude. The recall rate of the polarization ratio classifier shows an increase after 17 texture features are eliminated, but at the same time the precision of the classification drops.

Although all the 25 features could be used for the lead classification, the ones that do not show significant benefit for the classification result are removed. Based on Figures 4.7a,b,c the number of texture features equal to 9 has been chosen for classification of the HH channel and the polarization product, i.e., the first 16 texture features of the first and the second columns in Table 4.3 are removed from the classification. Although only 9 of the texture features are kept, it should, however, be noticed that one could use up to 16 features if even a little improvement of the classification quality is desired. For the polarization ratio the last 8 texture feature from Table 4.3 (the third column) are used for classification in further studies, the first 17 are removed from the polarization ratio classification.

N	HH	polarization product HH·HV	polarization ratio HH/HV
1	entropy$_o$	inverse difference moment$_o$	entropy$_{ssv}$
2	ASM$_o$	correlation$_{ssv}$	inverse difference moment$_{ssv}$
3	sum entropy$_{ssv}$	sum entropy$_o$	ASM$_{ssv}$
4	sum entropy$_o$	sum entropy$_{ssv}$	inverse difference moment$_o$
5	inverse difference moment$_o$	entropy$_o$	inf. measure of correlation$_{ssv}$
6	entropy$_{ssv}$	entropy$_{ssv}$	sum entropy$_{ssv}$
7	sum of squares: variance$_{ssv}$	difference entropy$_{ssv}$	ASM$_o$
8	ASM$_{ssv}$	ASM$_o$	difference entropy$_{ssv}$
9	difference entropy$_o$	inverse difference moment$_{ssv}$	entropy$_o$
10	difference entropy$_{ssv}$	sum of squares: variance$_{ssv}$	difference entropy$_o$
11	correlation$_{ssv}$	difference entropy$_o$	inf. measure of correlation$_o$
12	inf. measure of correlation$_o$	inf. measure of correlation$_o$	correlation$_{ssv}$
13	inf. measure of correlation$_{ssv}$	contrast$_o$	correlation$_o$
14	contrast$_{ssv}$	correlation$_o$	sum variance$_{ssv}$
15	contrast$_o$	difference variance$_{ssv}$	sum average / cluster tendency$_{ssv}$
16	difference variance$_{ssv}$	inf. measure of correlation$_{ssv}$	sum of squares: variance$_o$
17	sum average / cluster tendency$_{ssv}$	ASM$_{ssv}$	sum of squares: variance$_{ssv}$
18	correlation$_o$	sum variance$_{ssv}$	difference variance$_{ssv}$
19	inverse difference moment$_{ssv}$	contrast$_{ssv}$	sum entropy$_o$
20	sum variance$_{ssv}$	sum average / cluster tendency$_{ssv}$	contrast$_o$
21	sum of squares: variance$_o$	sum of squares: variance$_o$	difference variance$_o$
22	difference variance$_o$	difference variance$_o$	contrast$_{ssv}$
23	sum average / cluster tendency$_o$	sum average / cluster tendency$_o$	original image
24	sum variance$_o$	sum variance$_o$	sum average / cluster tendency$_o$
25	original image	original image	sum variance$_o$

Table 4.3: Elimination order of texture features, i.e., the lower the number N the least important is the respective feature for the classifier. Indices o and ssv stand for the texture features calculated on the original image and the small-scale variations of the image, respectively (see section Texture and polarimetric features). Definitions of the texture features are given by Haralick et al. (1973). The three columns present the elimination order for the three classifiers based on (i) the HH channel, (ii) the polarization product, and (iii) the polarization ratio.

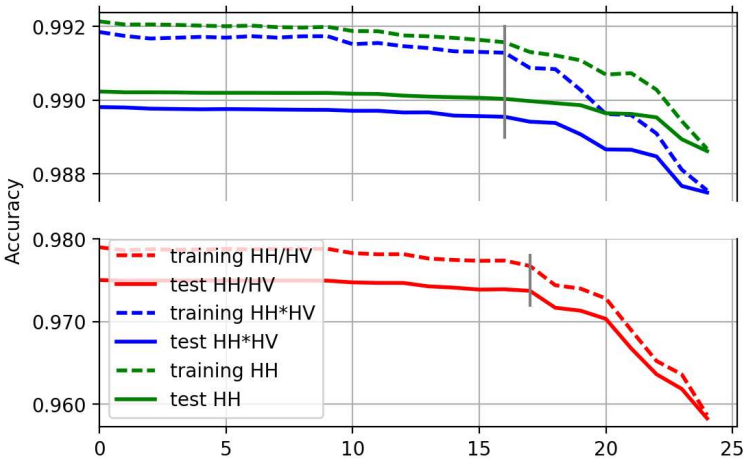

a – accuracy with number of eliminated features

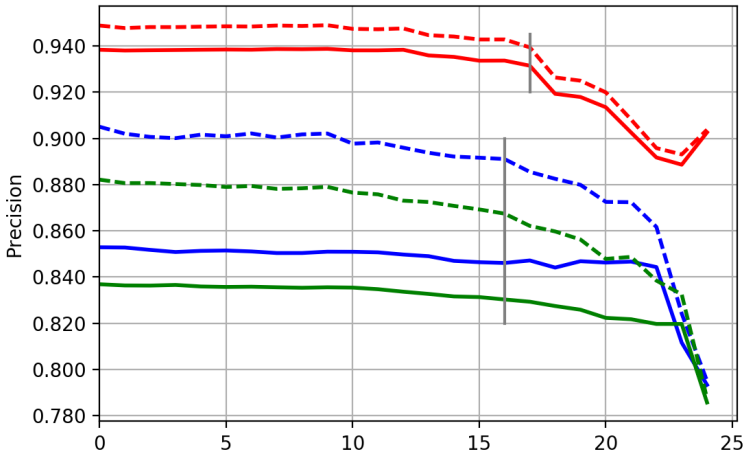

b – precision with number of eliminated features

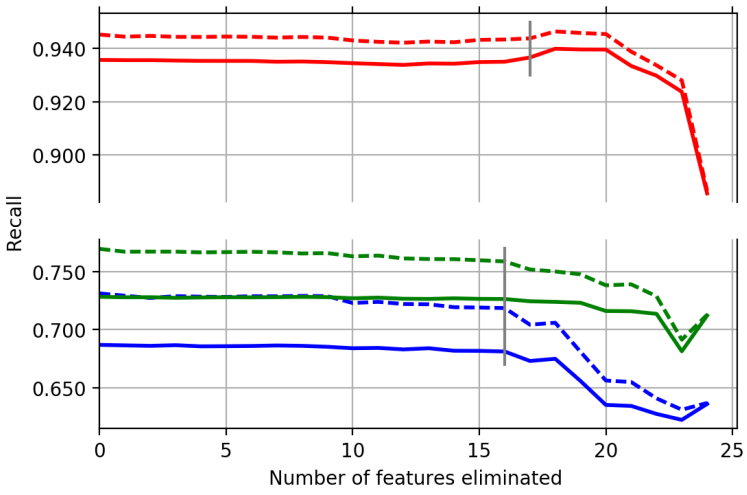

c – recall with number of eliminated features

Figure 4.7: Accuracy *a*, precision *b*, and recall *c* scores of the three classifiers depending on number of features eliminated during the recursive feature elimination analysis. The scores are calculated for the training and test datasets for each of the three classifiers based on the polarization ratio (red), the polarization product (blue), and the HH channel (green).

Since the same dataset is used for both the HH and the polarization product classifiers, their performance can be compared. The accuracy of the HH channel classification is only 0.2% higher than the accuracy of the polarization product classification. On the other hand, the polarization product classification shows a higher precision, but a lower recall comparing to the HH channel classifier. Since it is not defined at this stage whether precision or recall is more important for lead classification, it is not possible to make a conclusion on which of the two classifiers shows a better classification quality at this point. In order to find which of the two classifiers, based on the polarization product and the HH channel, shows better classification quality, the influence of a probability threshold on precision and recall, and, therefore, on the lead classification is analyzed in the next section.

4.2.2 Optimal probability threshold

The Random Forest Classifier provides probabilistic classification, which can be analyzed as is or can be used to obtain the corresponding binary classification by setting a threshold. Here we study the influence of a threshold used to produce the binary classification on the classification quality.

Three probabilistic classifications of the test data were produced with the three classifiers based on the HH channel, the polarization product HH·HV, and the polarization ratio HH/HV. Than a range of threshold is applied to each of them to receive the corresponding binary classification.

To describe the influence of the threshold, the precision–recall curves are calculated for each of the three classifiers, results are shown in Figure 4.8. Dashed lines correspond to precision–recall curves calculated for the training dataset, solid lines are calculated for the corresponding test dataset. Red lines represent the quality of the classifier based on the polarization ratio which is used for the bright lead detection. Blue and green lines represent qualities of classifiers based on the polarization product and the HH channel, respectively. The numbers in black give the respective threshold values used. A higher threshold improves the precision score (i.e., reduce amount of misclassification) but at the same time lowers the recall score (reduce the number of lead pixels detected).

From Figure 4.8 it can be seen that leads are classified with only 84% and 83% precision on the polarization product and the HH channel if the default threshold of 50% probability is used (the solid blue and the solid green curves). But in this case 68% and 72% of all pixels belonging to the lead class are identified (the recall score). If the threshold is set to 70%, then only 57% and 60% of the lead pixels will be detected, but precision of the classification is 92% and 90% (for the polarization product and the HH channel, respectively). To identify more lead pixels the threshold can be lowered.

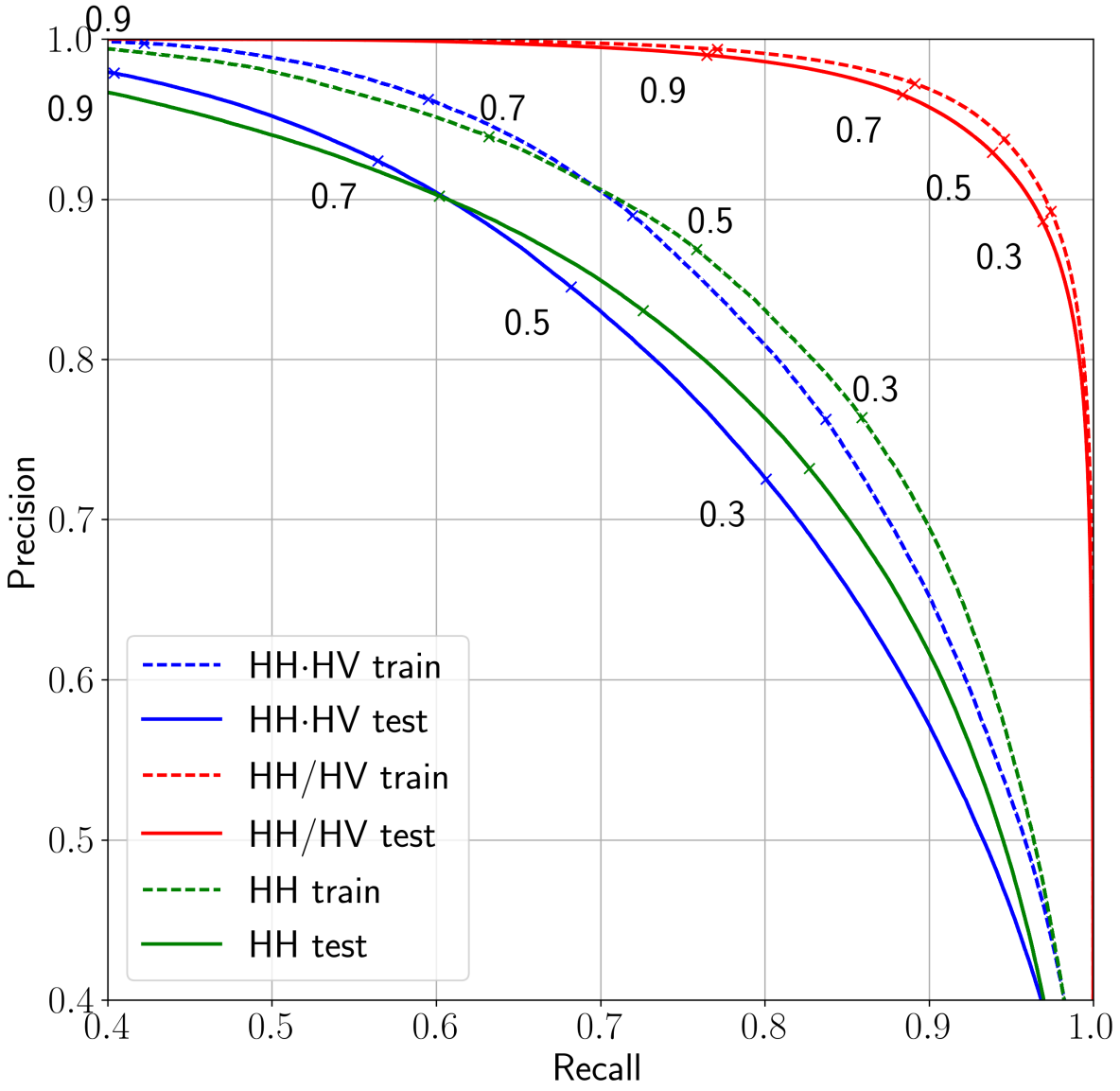

Figure 4.8: Precision–recall curves calculated for the training (dashed) and the test (solid) datasets corresponding to three classifiers: based on the polarization product (blue), the HH channel (green), and the polarization ratio (red). The curves are obtained by applying different thresholds to a probabilistic classification. The points on the curves which correspond to the threshold values of 30%, 50%, 70% and 90% are denoted in the figure (0.3, 0.5, 0.7, and 0.9, respectively).

For example, the threshold set to 30% will allow to detect 80% and 82% of all pixels belonging to leads, but the precision of the classification will drop to 72% and 73%, respectively, for the two classifiers HH and HH·HV.

Similarly, threshold can be adjusted for the polarization ratio classification. The default value 50% will give 93% precision and 94% recall, the higher value, 70% for instance, will increase precision to 97% and decrease recall to 88%. The lower threshold value of 30% will produce the binary classification with 88% precision, up to 97% of lead pixels will be identified.

The solid blue and the solid green curves intersect at the point where precision is 90% and the recall rate is 60%. This means the two classifiers show the same classification quality for the corresponding two threshold values of the two classifiers. For a higher threshold value, a higher precision can be achieved with the same recall rate value if the polarization product classification is used with the appropriate threshold value. Let us consider the right part of precision–recall curves where the green curve is above the blue. It corresponds to an application where the amount of leads detected (the recall rate) is more important than a very high precision (which is lower than 90% in this part of the curve). In this case for any value of the recall rate the binary classification based on the HH channel shows better precision (when a certain threshold is applied to the probabilistic classification) than the binary classification based on the polarization product.

The opposite is true for the left part of precision–recall curves where the blue solid line is above the green one (i.e. applications where a high precision is important). Based on these curves one can chose the appropriate threshold value for a certain task. For example, in climate studies about heat balance and energy one would want to have as many leads detected as possible although some of the detections are wrong. On the other hand, for navigation it is more important to know the location of leads with the highest precision possible even though the number of leads detected is lower.

4.2.3 Evaluation with optical images

So far only results based on the Sentinel-1 SAR data without overlap with optical Sentinel-2 data have been presented. In this section an evaluation of the leads classification quality is conducted for the two Sentinel-1 SAR scenes which overlap with optical Sentinel-2 data (Figures 4.2, 4.3). Two probabilistic classifications of the first evaluation image (Figure 4.2) were produced. The first one is based on the HH channel (Figure 4.2a), the second is based on the polarization product (Figure 4.2c); 9 of the most important texture features (last 9 features in the first and the second columns in Table 4.3) were used in both cases. Results are shown in Figure 4.9. High probabilities

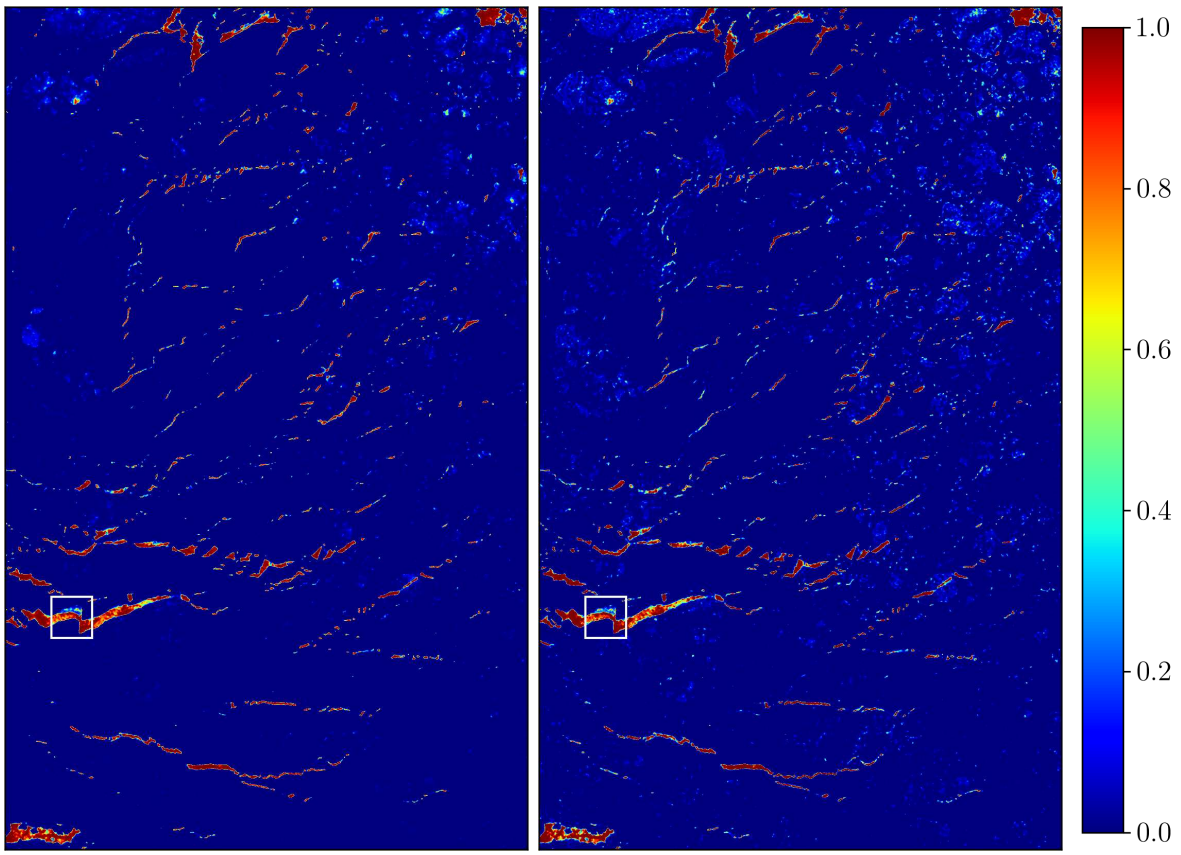

a – HH channel b – polarization product

Figure 4.9: Probabilistic classifications of the SAR scene shown in Figure 4.2c performed with the Random Forest Classifier. *a* and *b* are classifications based on the HH channel and the polarization product, respectively. High values mean high probability of a pixel to be classified as a lead.

of leads are assigned to areas which can be considered as leads from the optical image. Edges of leads have lower probability comparing to their inner parts. This effect is expected because the classification is based on texture features which are calculated within a window around each pixel. Some ice floes appearing dark on SAR images have non-zero probability values, but can easily be distinguished from leads. The upper part of a lead (the white frame at Figures 4.9a and b) has a significantly lower probability because it is covered with new ice as it can be confirmed from the optical data (Figure 4.2d). Large leads are detected correctly, but thin leads (up to 10 pixels which corresponds to 400 meters) are often split into several small pieces. Leads with width less than 5 pixels (200 meters) are smoothed on the step of texture features calculation. As the result such leads have low probabilities and can be considered as not-detected. This is a disadvantage of the method which cannot be eliminated because to calculate texture features relevant for a lead, the lead should have a size comparable or larger than the window size used for texture feature computation.

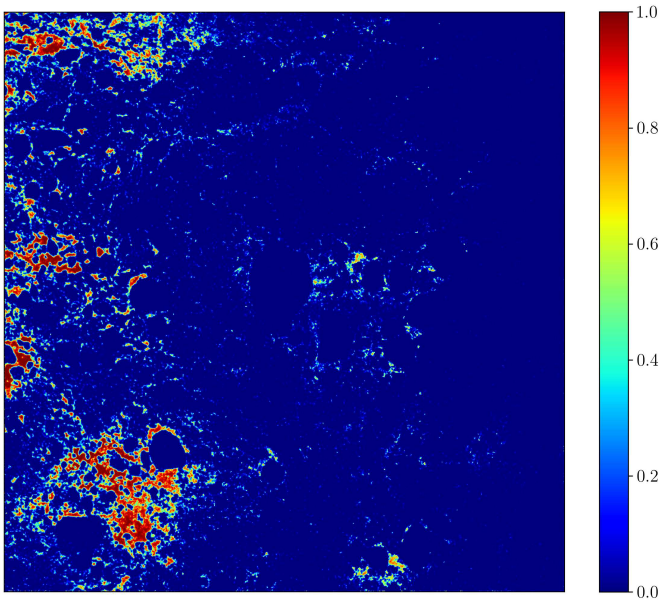

Figure 4.10: A probabilistic classification of the scene shown in Figure 4.3c performed with the Random Forest Classifier and based on 8 texture features.

The probabilistic classification of the second evaluation image (Figure 4.3c) for the polarization ratio is performed with 8 input features. Figure 4.10 shows the result of the probabilistic classification. Many open water areas at the left side of the scene are classified as leads while in the middle leads are not detected. This can be explained by the fact that leads are more pronounced at the left side of the polarization ratio (see Figure 4.10c) which is used as input for the algorithm. The fact that areas which are classified as leads are covered with open water are confirmed with the optical observation (Figure 4.10d).

The following example illustrates the algorithm for lead detection (the flowchart for the algorithm is shown in Figure 4.1). The preprocessed Sentinel-1 SAR images are shown in Figure 4.11a, b. Two large elongated objects are present on the illustration, one is dark on both the HH and the HV channels, the other one is bright on the HH and dark on the HV channel. The two objects represent the two classes of leads we have introduced here, "bright" and "dark" leads. No optical data is available for the scene to confirm that the objects are leads, the objects is only compared with leads appear in SAR images.

To classify both types of leads, two classifiers are applied – one for the dark lead detection and one for the bright lead detection. At first, based on the HH (Figure 4.11a) and the HV (Figure 4.11b) channels, the polarization product (Figure 4.11c) and the polarization ratio (Figure 4.11d) are calculated. Dark leads are detected from the HH channel using the algorithm based on either the HH channel or the polarization product

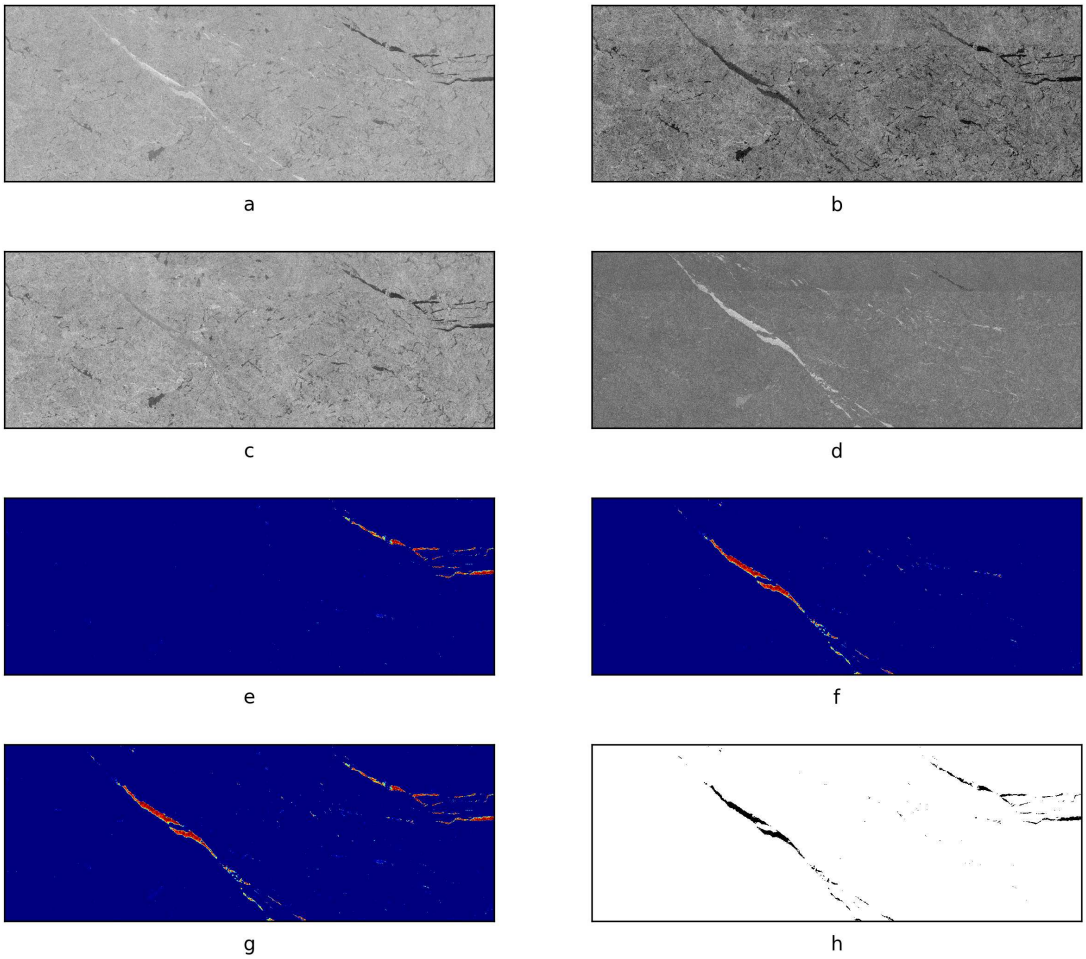

Figure 4.11: *a* and *b* are preprocessed HH and HV channels of a Sentinel-1 scene. *c* and *d* are the polarization product and the polarization ratio derived from the HH and HV channels. *e* and *f* are probabilistic classifications of the SAR scene based on the polarization product and the polarization ratio performed with the Random Forest Classifier. High values means high probability of the pixel to be classified as a lead. *g* is the sum of the two probabilistic classification. *h* is binary classification based on g with 50% probability threshold applied.

(the result based on the polarization product is shown in Figure 4.11e). Bright leads are detected with the algorithm based on the polarization ratio (Figure 4.11f). Afterwards, the probabilities for the dark lead and the bright lead branches are added together. As the last step, a threshold of 50% is applied to the resulting probabilistic classification, so that the final binary classification is obtained (Figure 4.11h).

4.2.4 Binarization and shape-based filtering

The Random Forest classifier was trained on 90% of the training dataset and tested on the remaining 10%. All objects from both the training and testing dataset are classified correctly. To avoid overfitting the maximal depth for decision trees was limited to 12 levels. Additionally, scenes not used for the algorithm training and testing have been visually evaluated for possible misclassifications to ensure no overfitting occur. It should be kept in mind how the manual test/training dataset was created (last section): only "easy" cases that are clearly a *lead* or *not a lead* are part of the dataset. For this "idealized" test dataset it is concluded that the very high accuracy value is reasonable. Actually, the classifier identifies many more objects in the test scenes than the objects being part of the test/training dataset. For these objects, however, it is not clear if they are leads or not as no in situ measurements is available. Thus, no accuracy can be assigned to these objects, but certainly some object might be misclassified. Therefore, the high classification accuracy for the test/training dataset should not be mistaken as accuracy for the whole procedure. Future studies with airborne high-resolution evaluation datasets may shed more light on this.

In addition to a classification, the Random Forest classifier provides information on feature importance. Shape properties ranking by importance and percent of cases a certain shape property was used during the training process are shown in Figure 4.12. The raw numbers are present in Table 4.4.

The ranking is shown for the "dark lead" cases based on the HH channel and for the "bright lead" cases based on the polarization ratio channel separately. This is due to the fact that object shape properties distribution can vary for the two cases due to higher noise level of the HV channel that is used to calculate the polarization ratio. In both cases, the HH channel and the polarization ratio, the features *eccentricity*, *minor axis length*, and *effective width* dominate the shape feature importance. For the polarization ratio also *width to length ratio* has an above 10% importance. Most of the other of the in total 16 considered features contribute with 2% to 4% to the classification. Considering that also some features are correlated (e.g. *eccentricity* and *width to length ratio*) one could reduce the number of features if needed for computational reasons. Here all features are kept as all are contributing to the classification to some degree.

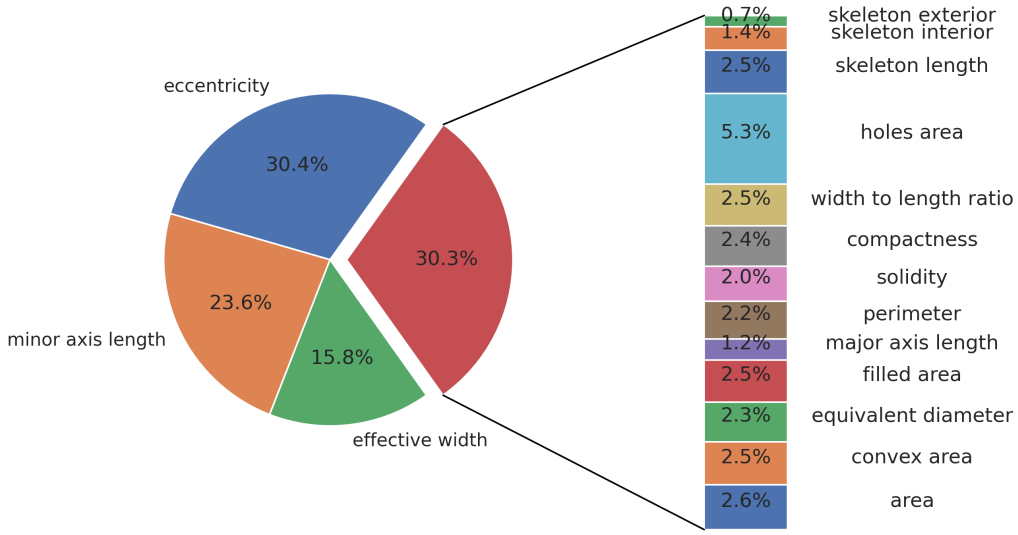

a – HH channel shape features

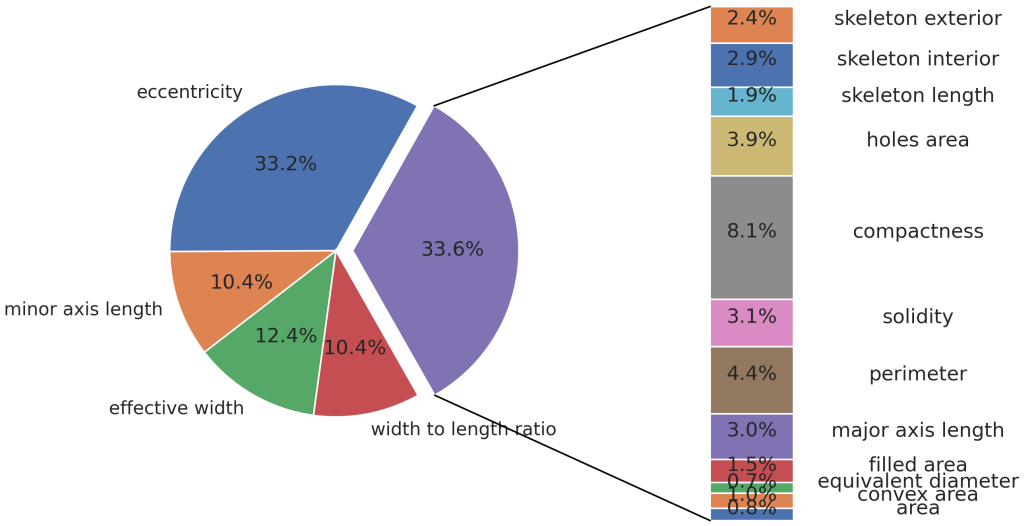

b – Polarization ratio shape features

Figure 4.12: Importance of shape parameters for the Random Forest classifier. *a* shows the feature importance for the classification based on the HH channel and *b* on the polarization ratio. In both cases only 3 and 4 out of the 16 features contribute with more than 10% to the classification, respectively.

parameter	HH	band ratio
area	0.0264	0.008
convex area	0.0253	0.010
eccentricity	0.3038	0.333
equivalent diameter	0.0235	0.007
filled area	0.0248	0.015
major axis length	0.0122	0.030
minor axis length	0.2356	0.104
perimeter	0.0224	0.044
solidity	0.0205	0.031
effective width	0.1576	0.124
compactness	0.0238	0.081
width to length ratio	0.0247	0.104
hole area	0.0533	0.039
skeleton length	0.0254	0.019
skeleton interior	0.0138	0.029
skeleton exterior	0.0067	0.024

Table 4.4: Feature importance as a fraction of number of cases the feature has been used to the total number of cases provided with the trained Random Forest classifier

As an example a fine scale illustration of the lead detection results for each stage of the algorithm is shown in Figure 4.13. A cutout of the original Sentinel-1 scene taken on 2 January 2019 over the Chukchi Sea is shown in Figures 4.13a (HH channel) and 4.13b (polarization ratio). As first step, the lead detection algorithm is applied to each of the two input channels, the HH channel (a) and the polarization ratio (b). The probabilistic classification results are shown in Figures 4.13c and 4.13d, respectively. Figures 4.13e, 4.13f, 4.13g, 4.13h show binary lead classification results derived from 4.13c and 4.13d by applying a method to both inputs separately and merging results together. Figure 4.13e shows the binary result of the lead detection if a 50% threshold applied to the probabilistic lead detection algorithm as described in Section 4.1.4. If the binary threshold is replaced with the binarization based on the watershed segmentation algorithm described in section 4.1.5 the result has less small scale noise as shown in Figure 4.13f. Figure 4.13g shows detected leads from the previous step (4.13f) that are kept by the object shape-based filter based on the Random Forest classifier described in Section 4.1.5. As a last step, small, non-elongated objects in the surrounding of noisy pattern detected in the previous step are removed and the final lead detection result is shown in figure 4.13h.

Classification results are compared with Sentinel-2 optical images, Figure 4.14. Sentinel-1 SAR and Sentinel-2 optical images were acquired on 21 March 2019 with 7 hour time difference. Despite changes in the ice field between the SAR and the optical image

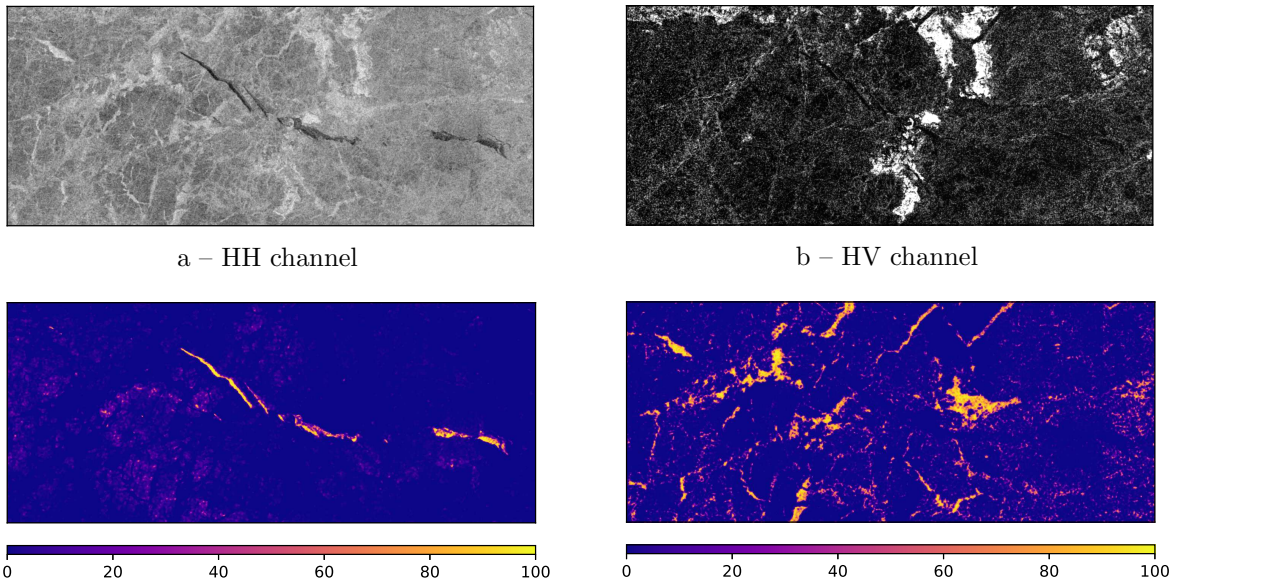

a – HH channel

b – HV channel

c – probabilistic classification of a

d – probabilistic classification of the polarization ratio HH / HV

e – 50% threshold binary from c and d

f – watershed binary from c and d

g – shape-based filter applied to f

h – small objects near noise removed from g

Figure 4.13: Example of lead classification: a and b – raw data, HH and HV SAR channels; c and d – dark (HH) and bright (polarization ratio) probabilistic lead classifications; e – binary classification calculated by applying a 50% threshold (as example; in the final classifier the watershed result in f is used); f – binary classification calculated with watershed binarization; g – shape-based filter is applied to the binary classification in f calculated with watershed; h – final result; small objects near noise classified with the shape-based classification are removed. The scene was taken on 2 January 2019 over the Chukchi Sea.

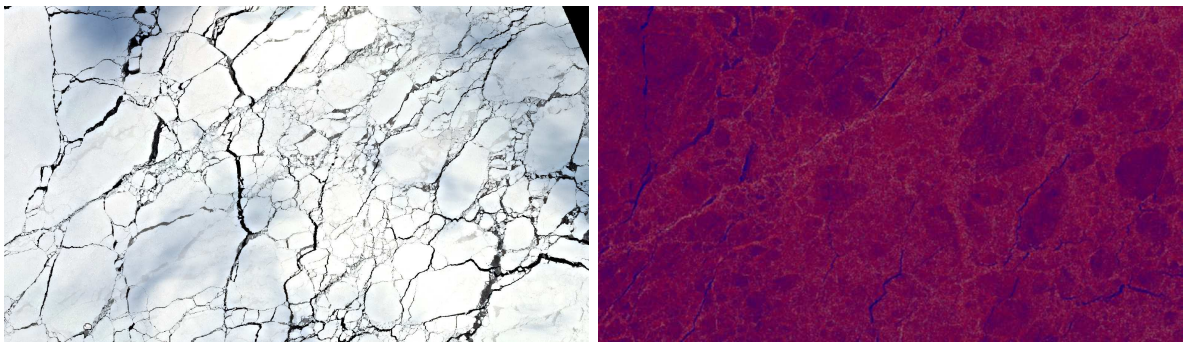

a – Sentinel-2 RGB

b – Sentinel-1 pseudo-RGB (HH, HV, HV/HH)

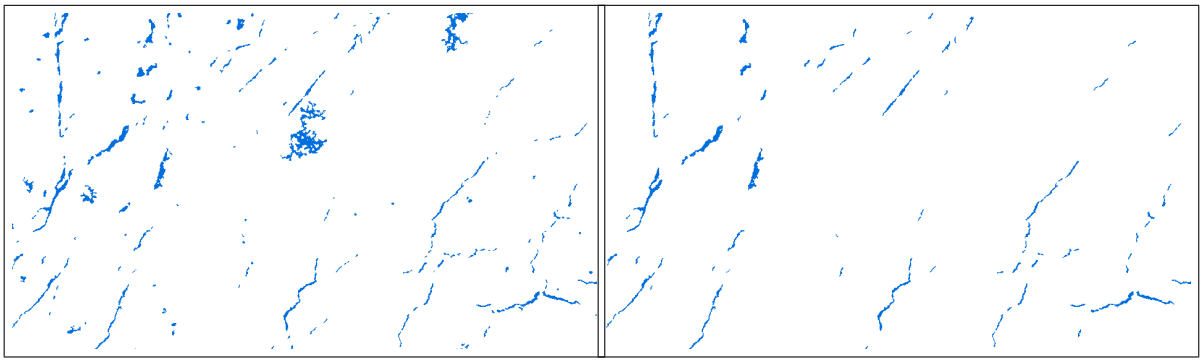

c – binary lead map

d – shape-filtered lead map

Figure 4.14: *a* – Sentinel-2 optical RGB image has been acquired on 21 March 2019 at 9:17UTC, *b* – Sentinel-1 SAR pseudo-RBG (HH, HV, HV/HH) has been acquired on 21 March 21 2019 at 2:32UTC, *c* – result of the basic lead detection algorithm applied to scene *b*, *d* – result of the final lead detection algorithm with the shape filter applied to the result *c*.

(Figure 4.14(a, b)), the major cracks are recognizable on both images and are detected with the lead detection algorithm Figure 4.14c. However, several noisy patterns are detected as leads with the lead detection algorithm, which are then filtered out with the shape-based filter as shown in Figure 4.14d.

To see the large-scale picture, the improved lead detection algorithm has been applied to all Sentinel-1 scenes acquired over the Arctic on 2 January 2019. The binary lead classification on individual SAR scenes are merged together to produce an Arctic-wide lead map as described in Section 4.1.7. After that, the binary lead information is available at 80 meter resolution Arctic-wide for all regions covered by Sentinel-1 SAR (full coverage takes about three days). Due to the high resolution and large extent of the map, it is not possible to present it here in full detail as figure. Therefore, the lead area fraction is calculated on a 12 km grid.

An Arctic-wide comparison of lead detection results is shown in Figure 4.15. The four images in Figure 4.15a, 4.15b, 4.15c, and 4.15d correspond to images 4.13e, 4.13f, 4.13g, and 4.13h of the fine scale comparison. That is, Figure 4.15a represents result of the

lead detection algorithm described in this chapter, Figures 4.15b and 4.15c are results at the two intermediate steps: binarization based on the watershed segmentation and supervised shape-based filter. Figure 4.15d represents the final result of the improved lead detection algorithm. We can see that every additional filter removes more and more *no-lead* objects. The final lead map in Figure 4.15d shows a more uniform distribution of leads without apparently artificial higher lead fractions along the swath edges. Areas with higher lead fraction like in the Beaufort Sea still can be clearly identified. It cannot be excluded that some "true" leads are removed by the filter but the classified leads in the final map in Figure 4.15d are detected with high confidence, which is most important for all statistical analysis to be applied on it in future.

To ensure the algorithm produces stable result we have applied it to all Sentinel-1 scenes taken over the Arctic in January 2019. Daily lead maps are combined to 3-day composite maps to decrease the amount of gaps where no Sentinel-1 data was acquired. In case scenes overlap, the later acquired scene overlays the earlier acquired one. To avoid the influence of daily change in sea ice conditions on the estimate for the lead area fraction, the sea ice mask has been shrunk by 10 km in the marginal ice areas and along coastlines with morphological binary erosion. Therefore, areas where sea ice extent is smaller on Sentinel-1 scenes compared to AMSR2 data are not accounted as leads in further analysis. The total lead area and the sea ice area are calculated for each 3-day composite map and are shown in Figure 4.16a. The ratio of the two is presented in Figure 4.16b in green for the lead detection with 50% threshold on probabilistic result and in red for the result after the watershed binarization and the shape filter applied. Figure 4.16b also shows open water concentration calculated from the passive microwave sea ice concentration maps cut to the coverage of Sentinel-1 scenes for the corresponding days. The AMSR2 point on 2019-01-27 is an outlier due to reduced coverage in passive microwave data on the date. This is one of a few days, when AMSR2 data does not cover the entire Arctic, so that the lead area fraction is lower than what it would be with the full coverage. According to the shape-filtered lead detection, the mean lead area fraction in January 2019 is 0.71% with a standard deviation of 0.05 for the 10 data points of the time series, whereas the algorithm without the improvements shows a mean lead area fraction of 2.3% with standard deviation 0.2. The open water concentration on AMSR2 data is 1.8% with 0.3 standard deviation. Small variations in lead area and sea ice area may appear due to natural reasons, which include lead opening, closing, and refreezing, as well as due to small differences in satellite coverage since sometimes the Arctic is not entirely covered even on 3-day composite maps.

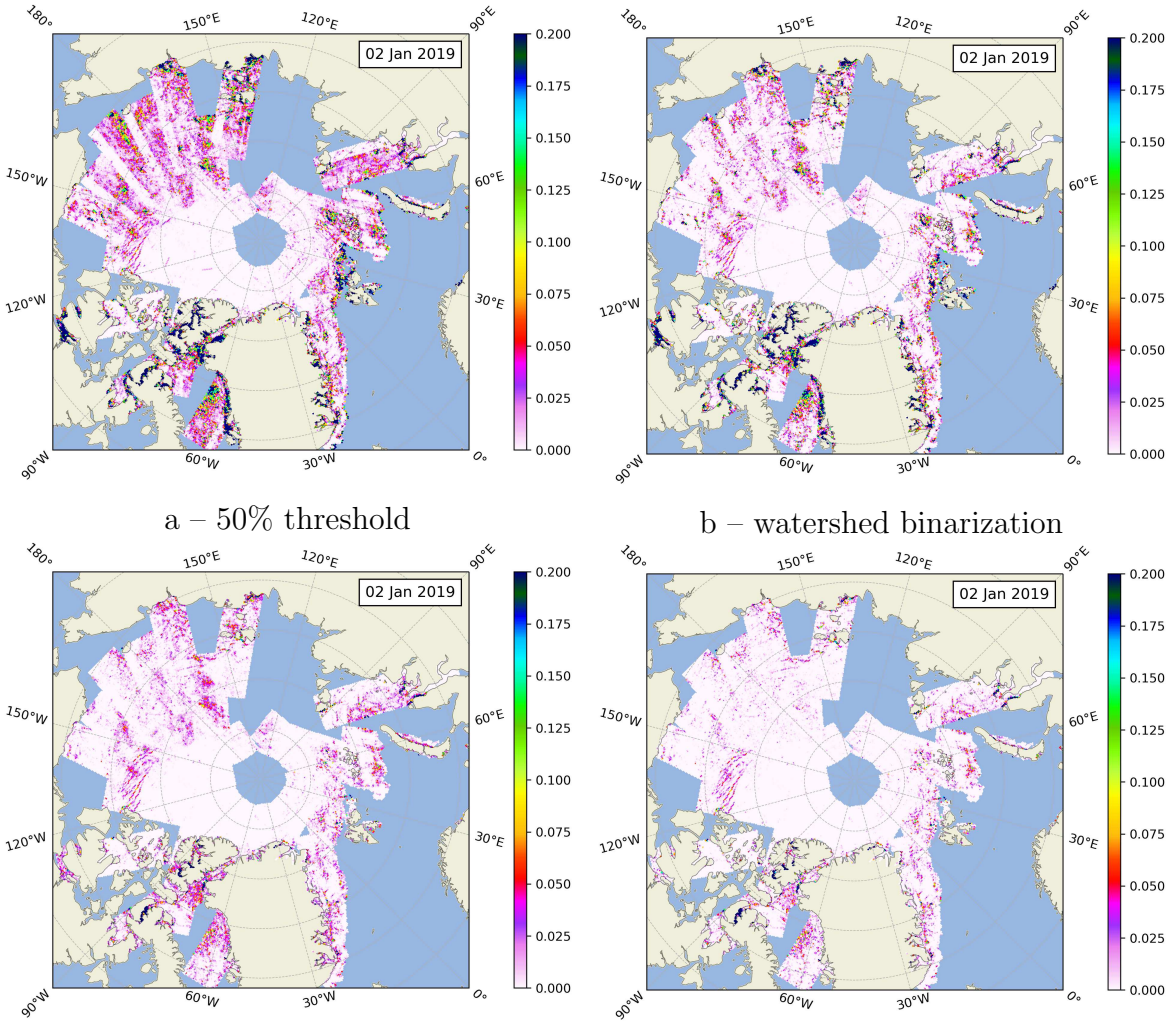

a – 50% threshold

b – watershed binarization

c – shape filter

d – final result

Figure 4.15: Arctic-wide Lead Area Fraction maps (12 km resolution) derived from the daily Arctic lead map. The Arctic lead map consists of all Sentinel-1 scenes acquired over the Arctic on 2 Jan 2019. *a* Lead Area Fraction derived with the original algorithm based on GLCM features and Random Forest classifier. *b* Lead Area Fraction calculated by replacing the original threshold binarization with the watershed binarization algorithm and with the shape-based filter applied. *c* Lead Area Fraction after additionally applying the shape-based filter on *b* without removing objects in surrounding of the noisy patterns. *d* Final Lead Area Fraction map after applying all filters.

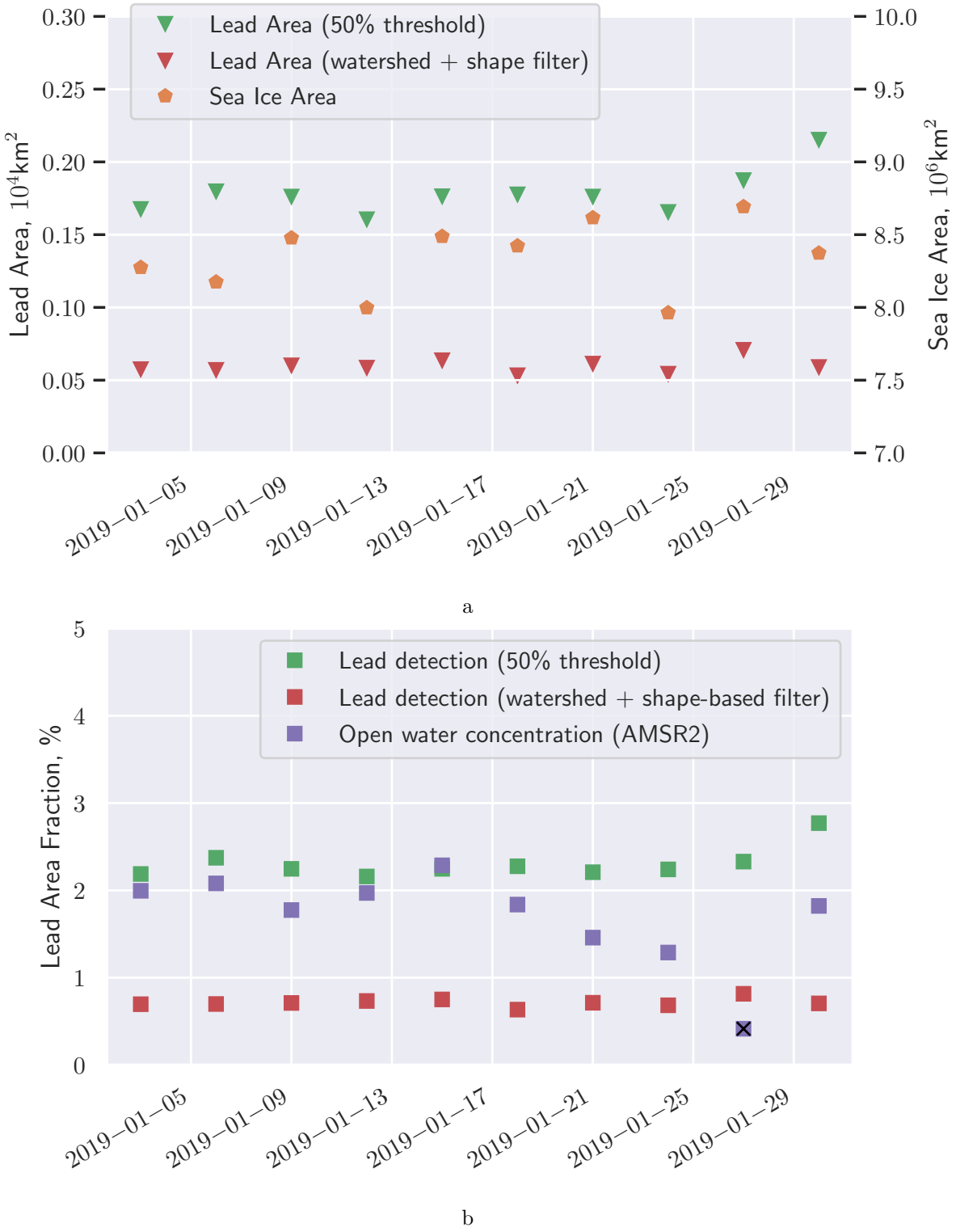

Figure 4.16: *a* – Lead area (left y-axis) and sea ice area (right y-axis), and *b* – lead area fraction derived from 3-day composite lead maps of the Arctic in January 2019. The sea ice area in *a* mainly changes due to changing satellite coverage (i.e., not due to ice growth/melting).

4.3 Discussion

4.3.1 Texture features required for classification

The procedure of texture features elimination shows that the use of a range of texture features (the first 9 from each column of Table 4.3) do not improve the classification and therefore is excluded. At the same time these texture features do not decrease classification quality. This is because although these features are fed to the classifier, only the texture features that help to perform classification are used within the Random Forest Classifier. In the process of elimination of the next 7–8 texture features, the classification quality slightly decreases. Therefore these 7–8 texture features may also be excluded from the classification process, especially if fast computation is of importance. As the result 16–17 texture features can be eliminated without significant decrease in classification quality, so that only 8–9 of the texture features are used in classification. In cases when even a little improvement of the classification quality is desired, up to 16 input features can be used. For the case when computational time is limited, the number of texture features used for classification can be decreased.

Of the 9 most important texture features (last 9 rows in Table 4.3) the majority is derived from the original input channel and not from the small scale variations data, where the background amplitude is removed. The original channel is one of the most important inputs for all three classifiers. This means texture features do not substitute the original channel and provide only a complementary information. Texture features and the original channel should be used in conjunction.

To produce the final lead map a classifier based on either the polarization product or the HH channel for dark leads should be used in combination with the classifier based on the polarization ratio for bright leads. In Figure 4.7b the classifier based on the polarization product shows higher precision, however, in Figure 4.7c the recall rate of the classifier is lower compared to the classifier based on the HH channel. This leads us to the conclusion that both the precision and the recall by itself do not provide enough information about the quality of a classification, neither of the two should be used as the only quality metrics, and both of them should be considered together.

In case of probabilistic classification, it is possible to increase the precision by the cost of the recall rate and vice versa by adjusting a threshold used to obtain the corresponding binary classification. Thus, a comparison of the two classifiers is performed by the use of the concept of the precision–recall curve.

4.3.2 Classification quality

First, considering the quality of dark leads classification. The precision–recall curves (Figure 4.8) of the HH channel and polarization product classifiers have an intersection point. This means each of the two classifiers is used in the final product, as both provide the best result in its own range of thresholds (location on the precision–recall curve, Figure 4.2.2). The quality of the classifier based on the polarization product is higher when a high precision (over 90%) of lead detection is desired. In this case only about 60% or less leads will be detected. If the recall rate also matters for the application, the HH channel should be used for dark leads classification.

The precision–recall curves clearly show that the quality of bright leads classification is higher than of the dark leads classification based on both the polarization product and the HH channel (red curves are above blue and green curves). This might be due to the fact that sea ice can appear dark at both the HH and the HV channels and, therefore, may be misclassified as a lead. At the same time, the polarization ratio is known for its good water-sea ice discrimination potential. Objects appearing bright at the HH channel and dark at the HV channel are usually not misclassified as sea ice (which can be dark or bright at both channels) or pressure ridges (bright at both channels). This provides more confidence that an object detected from the polarization ratio is a lead.

In case of single channel measurements only the HH channel is available for Sentinel-1 EW images. This single channel mode is often used for scenes at high latitudes. In this case only the HH classifier for dark leads can be applied. If dual polarization SAR data is available, the polarization product and the polarization ratio can be calculated and, therefore, the classifiers based on the polarization product HH·HV and the polarization ratio HH/HV are used. The first classifier shows better classification quality for dark leads than the classifier based on the HH channel (Figures 4.7 and 4.8) when used for a high-precision classification (with precision above 90%). Since bright leads show a similar backscatter to ridges in HH channel, they cannot be detected from HH channel alone. Thus, with the use of the polarization ratio more leads are detected from the dual polarization SAR data than from single HH channel scenes.

Further in the study the HH classifier will be used to for "dark lead" detection and the classifier based on the polarization ratio for "bright lead" detection. Although the classifier based on the polarization product HH·HV has advantages when higher precision and lower recall rates are required, at 50% threshold the classifier based on HH channel only provides a better classification quality as described in Section 4.2.2 and shown in Figure 4.8. Also it can be applied for single polarization acquisitions (HH), which become more common when only one Sentinel-1 satellite is available (until October 2016, since December 2021 till present) to detect at least some of the leads ("dark lead" branch).

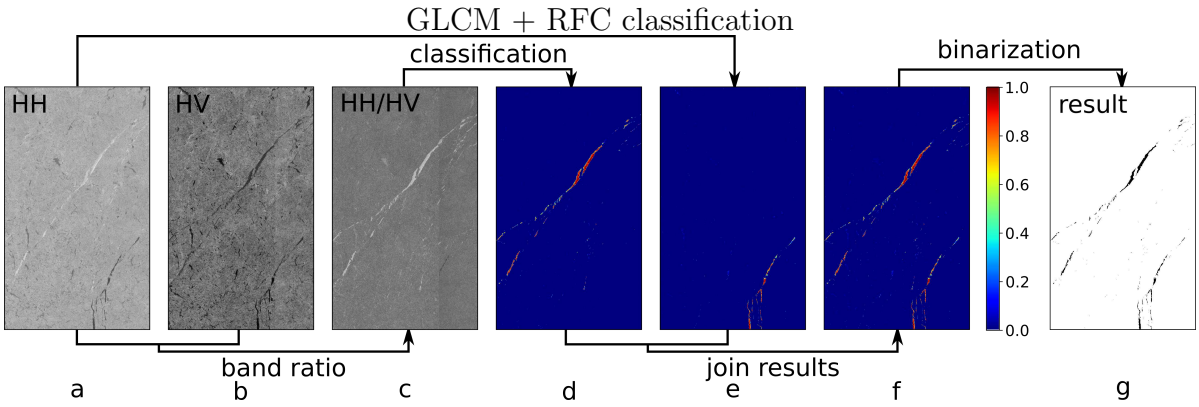

Figure 4.17: lead detection algorithm based on GLCM + RFC. *a* and *b* are the original Sentinel-1 SAR data (3 Feb 2016, 22:29, Canadian Arctic; size of the area shown is about 150 km by 80 km), HH and HV respectively. *c* is the polarization ratio HH/HV. *d* and *e* are probabilistic classification results of *a* and *c*. GLCM calculation and Random Forest classification is used on this step. *f* is the sum of probabilities *d* and *e*. *g* is the binary classification derived from *f* by applying a threshold of 50%.

The algorithm as it is used in later chapters is illustrated in Figure 4.17.

As the lead detection algorithm is based on backscatter analysis, open water between ice floes is classified as leads. During summer the separation of leads from melt ponds will not be possible with the features used here (the shape of the features would have to be considered). For the data used in this study there is no evidence for the presence of melt ponds. Therefore, the algorithm has not been evaluated for the summer season.

4.3.3 Binarization and shape-based filtering

The core of the lead detection algorithm is based only on NRCS values and texture features, so that also non-elongated objects like general open water area and polynyas are detected. These non-elongated objects are the detected open water areas or are caused by ambiguities in the backscatter signature. With the 80 m resolution of the lead detection, which is based on the 40 m pixel size Sentinel-1 SAR scenes, it is possible to account for the shape of the detected objects.

Objects *lead* or *not lead* have been manually labeled based on their shape. The shape characteristics distributions of this training/test dataset are shown in Figure 4.6. These distributions indicate that leads are, in most cases, smaller, more compact, and elongated compared to noise patterns appearing on Sentinel-1 scenes over smooth new ice areas. No single parameter can be used for their identification. The shape properties importance provided by the shape classification algorithm shows that the most often used feature is *eccentricity* followed by *minor axis length* and *effective width* (Figure 4.12 and Table 4.4). These properties are directly related to the elongation of objects. This perfectly fits the

definition of a lead as a crack in the sea ice cover, which often have elongated shape originating from nature of their occurrence, i.e. sea ice deformation.

The classification results shown in Figure 4.13 illustrate improvement of the algorithm performance with regard to lead detection. Objects of non-lead-like shape that might come from smooth young ice or can be related to scalloping and speckle noise in the SAR data are effectively removed. Such cases are shown in Figure 4.14, where binary lead map contains several non-lead-like structures (Figure 4.14c), which are removed with the shape filter (Figure 4.14d). This is especially important in the Siberian Arctic as it can be seen in Figure 4.15 on 2 January 2019. The confidence is high that the remaining features are leads with open water or thin ice. The new Arctic-wide lead distribution in Figure 4.15d is more uniform and has less artifacts compared to the original version without improved binarization and shape filters in Figure 4.15a. A typical pattern of intersecting leads can be seen in the Beaufort Sea and high lead fraction in the marginal seas like Laptev or Greenland Sea. In the high Arctic close to the North Pole as expected less leads can be observed. This qualitatively is in line with previous lead fraction datasets at lower spatial resolution from AVHHR Lindsay and Rothrock (1995), MODIS Willmes and Heinemann (2015); Reiser et al. (2020), AMSR-E Röhrs and Kaleschke (2012), and CryoSat-2 Wernecke and Kaleschke (2015) derived for other years.

The lead area and the sea ice area calculated on 3-day composite map are correlated as shown in Figure 4.16a. The correlation coefficients are 0.45 and 0.68 for the lead area calculated with 50% threshold, and with watershed binarization and shape filter applied, respectively. This indicates that the variations in the total lead area come from the variability of Sentinel-1 coverage. The difference in coverage should therefore have small influence on the lead area fraction calculated as a ratio of the lead area to the sea ice area.

In Figure 4.16b it is demonstrated that the watershed binarization and shape-based filter delivers stable results: the lead area fraction (plotted with red) for January 2019 shows only small variation around its average value of about 0.7%. The open water concentration in the central Arctic away from marginal ice area is known to be typically around 1-2% Lindsay and Rothrock (1995); Röhrs and Kaleschke (2012); Maykut (1978). In-situ observations of sea ice thickness indicate sea ice cover consists of 1% 0-20 cm thick sea ice (by area) Thorndike et al. (1975). Thus, the 0.7% lead area fraction derived with the lead detection algorithm with the shape filter applied is slightly lower comparable to the previous studies, while the lead area fraction derived with 50% threshold is slightly higher than the expected values. This indicate the shape-based filter filters out some of the real leads that might have a complex shape.

The major part of open water concentration variation on AMSR2 data comes from marginal ice areas where open water may have an arbitrary shape and often does not have

elongated shape. Therefore, these areas are not considered as *leads* by the improved lead detection algorithm. The lead concentration derived with the improved lead detection algorithm is below the open water concentration. This is expected as *lead* class contain only elongated open water areas. At the same time passive microwave measurements are known to be sensitive to a very thin ice. Leads covered with thin ice are likely to be excluded from the AMSR2 open water concentration. Whereas the lead detection algorithm is expected detect refrozen leads with ice thickness up to 10-20 cm as leads.

Lead area fraction in Figure 4.16b in red calculated on 3-day composite maps does not show high variability confirming the stability of the lead detection algorithm. Some variability is expected as leads may open or close based on dominance of divergent or convergent ice dynamic regimes. However, averaged of the whole Arctic this variability is small.

5 Lead detection with convolutional neural network

Despite watershed binarization and shape-based filter being applied as postprocessing steps to the lead detection algorithm described in the previous chapter, there is still some evidence of noise presented in results, as noticed in Figure 4.2.4. This chapter describes an improved lead detection algorithm based on the U-Net Convolutional Neural network (Ronneberger et al., 2015). Initially the U-Net architecture was introduced for biomedical image segmentation, but later has been applied for a variety tasks, including SAR image analysis (Park et al., 2020; Mao et al., 2020; Malmgren-Hansen et al., 2021; Stokholm et al., 2022). A part of the methods section in this chapter is published in Murashkin and Frost (2021).

First, an improved calibration algorithm is introduced in Section 5.1.1. The auxiliary data provides information not only on thermal noise, but also on scalloping noise singe 13 March 2018, as described in Section 3.1. This provides the necessary information for a more consistent Sentinel-1 data preprocessing, which is especially important for cross-polarization images. Next, U-Net architecture is adjusted for lead detection as described in Section 5.1.2. In order to apply the algorithm a Sentinel-1 scene should be split into smaller tiles, which are then fed to U-Net model. Tile edge effects, arising due to the split of an original large image into smaller tiles, often occurring in deep learning methods is addressed in Section 5.1.3. Classification results are presented in Section 5.2.1, evaluated with optical images in Section 5.2.2, and then compared with the algorithm described in the previous chapter in Section 5.2.3.

5.1 Methods

5.1.1 Data preprocessing

The previously described preprocessing algorithm (Section 4.1.1) has been improved with applying scalloping noise correction, which is available for Sentinel-1 data acquired after 13 March 2018. However, the thermal noise on the cross-polarization band remains pronounced on some images, as shown on example in Figure 5.1a,b. It remains because

the thermal noise data provided in the auxiliary data has a discrepancy, which is visible at the subswath borders. To correct for this, a swath brightness balancing technique bringing Normalized Radar Cross Section (NRCS) values within different subswath to a uniform scale, is introduced. The thermal noise distribution within a subswath is assumed to have little discrepancy, whereas the thermal noise absolute value has some error and can be corrected with a scale factor α:

$$noise^{new}_{SW_i} = \alpha_i \cdot noise_{SW_i} \tag{5.1}$$

where α_i is the scale coefficient for the subswath SW_i. Sentinel-1 scenes are assumed to be homogeneous at the subswath border, therefore the average brightness should not drastically change between subswaths. Thus, the SAR NRCS values averaged in along-track direction should be continuous in the range (cross-track) direction.

$$DN^2_{SW_i} - noise_{SW_i} = DN^2_{SW_{i+1}} - \alpha \cdot noise_{SW_{i+1}} \tag{5.2}$$

where DN is Digital Number (the value provided in Sentinel-1 level 1 product, before calibration and noise correction) averaged in along-track direction at the subswath SW_i to subswath SW_{i+1} transition. The 5th subswath is taken as reference and its scale factor is 1, 1st to 4th swaths are normalized to the NRCS values of the 5th subswath, see Figure 5.1. Then, the noise scale factor α_i is calculated with

$$\alpha_i = (DN^2_{SW_i} - DN^2_{SW_{i+1}} + noise_{SW_i})/noise_{SW_{i+1}} \tag{5.3}$$

Scaling thermal noise for the adjacent swath by α_i brings an opportunity to produce a more uniform Sentinel-1 image, which improves robustness of an automatic classification algorithm. An illustration for a preprocessed Sentinel-1 scene is shown in Figure 5.1. Figure 5.1a,b show two Sentinel-1 EW HV bands with the preprocessing procedure suggested by ESA with the noise tables provided. The different swaths are still visible, especially swath 1 (the leftmost subswath on images). The same images with the swath balancing applied are shown in Figure 5.1c,d. Figure 5.1e,f show backscatter values averaged along the azimuth direction. The abrupt changes in average brightness between subswaths with the basic noise correction applied (blue line) are eliminated with the swath brightness balancing applied (orange line).

5.1.2 U-Net convolutional neural network

The U-Net CNN is represented by a multi-level encoder–decoder architecture, where encoder and decoder are connected on every level (Ronneberger et al., 2015). For the lead

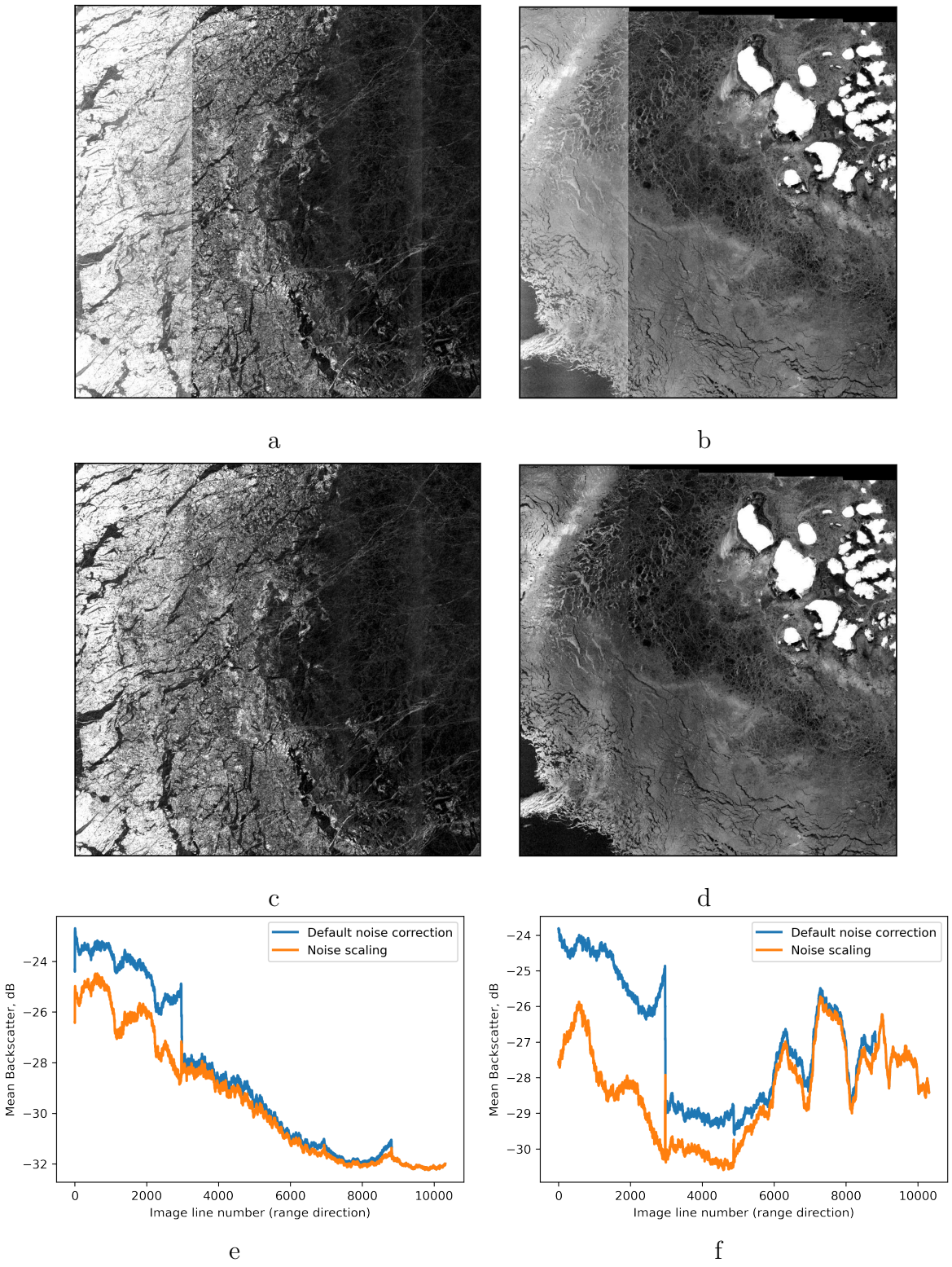

Figure 5.1: *a* and *b* – basic preprocessing result with the noise data provided in each scene; *c* and *d* – preprocessing result with noise scaling; *e* and *f* – mean brightness along azimuth direction, for the basic preprocessing *a*, *b* in blue, for the improved preprocessing algorithm *c*, *d* in orange.

detection the depth of the encoder and the decoder is increased to six layers compared to four layers suggested in the original study, the algorithm is schematically shown in Figure 5.2. A preprocessed Sentinel-1 image is split into 512-pixel square patches (are referred to as *tiles* further). The input for the model consists of a stack of the tiles, each of them has two layers: the HH band and the band ratio HV/HH, both normalized to [-1; 1]. Every standard unit (a single block on the diagram) consists of a dropout layer, where only 50% of inputs are connected to the output layer (Hinton et al., 2012), and two convolution layers with 3x3 pixel size kernel and ReLu activation function (Fukushima, 1969). Number of output layers are shown in Figure 5.2. Red arrows represent max pool layer, which decreases the image size two times by keeping only a single maximal value in every block of 2x2 pixels. Green arrows show upscale convolution layers, where image size in increased two times. In the decoder part of the algorithm (right side in Figure 5.2) results from the lower layer and the corresponding layer of the encoder (left part of the Figure 5.2) are concatenated and then passed to the standard unit as described above. The output layer includes L_2 kernel regularization Cortes et al. (2009) and a softmax activation function and creates output class probabilities.

For algorithm training a new set of data has been labeled. All scenes for the new training dataset have been acquired after 18 March 2018, so that they contain scalloping noise information in the auxiliary data. Twenty one Sentinel-1 scene have been pre-processed as described in this chapter (Section 5.1.1), converted to pseudo-RGB images as described in Section 3.1 and then manually labeled. The list of scenes is shown in Table 5.1. The major part of the data (90%) is used for training, the remaining 10% as test sub dataset.

5.1.3 Tile edge effects

An input to the model is a 512x512 pixel tile with two layers, the HH band and the HV band. A typical size of a Sentinel-1 EW GRDM scene is about 10000x10000 pixels. Therefore, the original images is split into tiles. Every tile is classified by the CNN independently. As the result, classification results might not match at the edges of the tiles, leading to appearance of edge effects at tile edges on the corresponding full size classified image.To reduce this effect, the classification is applied four times to every Sentinel-1 scene. Each of the four times the Sentinel-1 preprocessed image is split into tiles with an offset as shown in Figure 5.3. Frames in black, red, green, and blue colors correspond to 0% (no offset), 25%, 50%, and 75% relative offset. Every pixel of a classified tile is weighted linearly by its distance from an edge of the tile. This way, the classification result for a pixel in the middle of a tile has a higher weight compared to a pixel at an edge of the tile. Four weighted probabilities (one per offset) are summed up

List of Sentinel-1 scenes
S1A_EW_GRDM_1SDH_20190102T014317_20190102T014421_025292_02CC3B_F243
S1A_EW_GRDM_1SDH_20190102T032201_20190102T032306_025293_02CC41_C821
S1A_EW_GRDM_1SDH_20190102T032306_20190102T032406_025293_02CC41_66FC
S1A_EW_GRDM_1SDH_20190102T032406_20190102T032506_025293_02CC41_318E
S1A_EW_GRDM_1SDH_20190102T163157_20190102T163301_025301_02CC94_427C
S1A_EW_GRDM_1SDH_20190102T163301_20190102T163401_025301_02CC94_4D80
S1A_EW_GRDM_1SDH_20190102T163401_20190102T163501_025301_02CC94_C5B9
S1A_EW_GRDM_1SDH_20190102T180327_20190102T180427_025302_02CC9A_EBD9
S1B_EW_GRDM_1SDH_20190102T072713_20190102T072813_014312_01AA0F_B30E
S1A_EW_GRDM_1SDH_20200427T040317_20200427T040421_032308_03BD11_B2EE
S1A_EW_GRDM_1SDH_20200427T040421_20200427T040521_032308_03BD11_59F6
S1A_EW_GRDM_1SDH_20200427T072044_20200427T072148_032310_03BD24_499D
S1A_EW_GRDM_1SDH_20200427T072148_20200427T072248_032310_03BD24_5D32
S1B_EW_GRDM_1SDH_20200427T031414_20200427T031514_021324_028799_E14D
S1B_EW_GRDM_1SDH_20200427T062819_20200427T062919_021326_0287AA_C373
S1B_EW_GRDM_1SDH_20200427T062919_20200427T063019_021326_0287AA_FAC2
S1B_EW_GRDM_1SDH_20200427T080907_20200427T081007_021327_0287B6_BE66
S1B_EW_GRDM_1SDH_20200427T081007_20200427T081107_021327_0287B6_F2EF
S1B_EW_GRDM_1SDH_20200427T081107_20200427T081207_021327_0287B6_0532
S1B_EW_GRDM_1SDH_20200427T081207_20200427T081307_021327_0287B6_68A9
S1B_EW_GRDM_1SDH_20200427T094631_20200427T094731_021328_0287C3_178E

Table 5.1: List of the scenes which have been manually labeled and used as a training dataset for the lead detection algorithm.

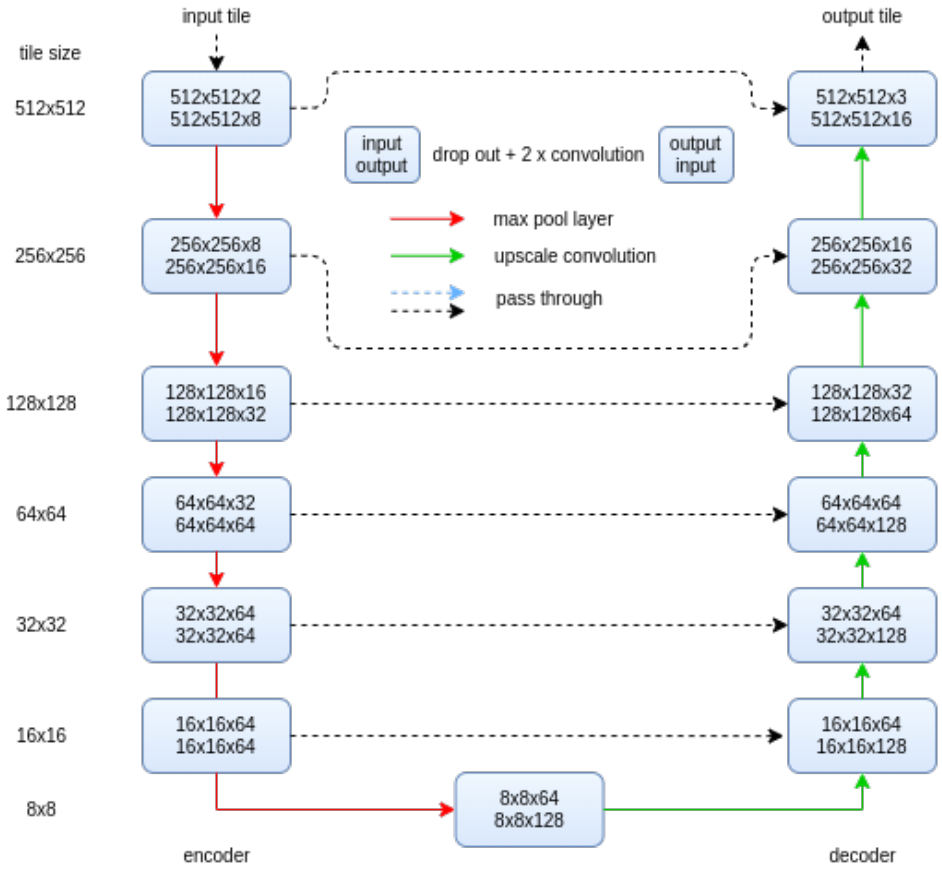

Figure 5.2: The original U-Net architecture has been extended to 6 layers and input tile size has been increased to 512 pixels.

to the final classification result. For instance, a pixel shown in purple of an input scene will appear at the middle of the red tile (split into tiles with 25% offset), closer to an edge of the green and black tiles (split into tiles with 50% and 75% offset), and at the edge of the blue tile (75% offset). Therefore, the lead probability, produced by the model applied to the red tile, has the highest contribution to the final result, while the lead probability, produced by the model applied to the blue tile, has the lowest contribution. The influence of near-border pixels on the per-pixel classification is decreased, thus, the transition between tiles becomes smooth improving the final classification result.

5.2 Results

The U-Net -based classification workflow with results is shown in Figure 5.4. Preprocessed as described in Section 5.1.1 HH (Figure 5.4a) and HV (Figure 5.4b) channels are used to calculate the polarization ratio, shown in Figure 5.4c. The HH channel and

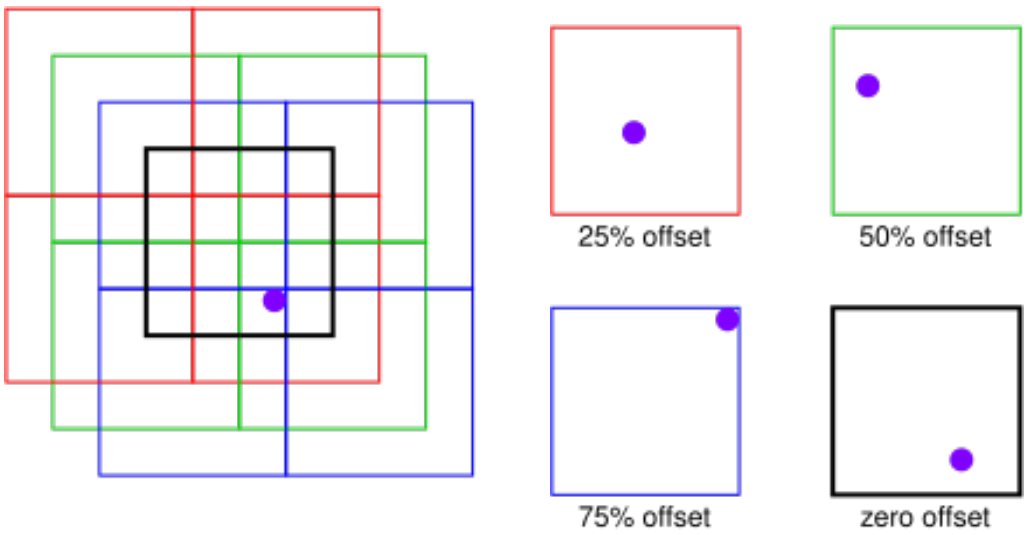

a b

Figure 5.3: Smooth prediction for edge effects reduction. A trained model is applied to a given scene four times, each time with an offset. Zero offset is shown in black, 25% offset is red, 50% offset is green, 75% offset is blue. A pixel of a tile (shown in purple) appears close to the center of the tile in case of red tiling and close to the edge on the blue tiling.

true\predicted	dark leads	bright leads	sea ice
dark leads	0.989	0.0	0.011
bright leads	0.0	0.989	0.011
sea ice	0.001	0.0	0.999

Table 5.2: Normalized confusion matrix for the lead detection algorithm. i-th row and j-th column entry indicates the number of samples with true label being i-th class and predicted label being j-th class.

the polarization ratio are passed to the U-Net -based classifier described in Section5.1.2, which produces probabilities for dark leads (Figure 5.4d) and bright leads (Figure 5.4e). Both are merged together into the result shown in Figure 5.4f, which is then converted to a binary lead map shown in Figure 5.4g.

The classification quality is evaluated by applying the classification to 18 manually labeled Sentinel-1 scenes, which have not been used for training or testing. The classification accuracy on the evaluation data is 99.2% with balanced classes. The normalized confusion matrix calculated with balanced classes is shown in Table 5.2. Both the accuracy score and the confusion matrix are weighted by number of class samples.

5.2.1 Classification results on a small scale

Classification results on each step of the algorithm and comparison to the similar results from the algorithm described in the previous chapter (see Section 4.1) are shown in

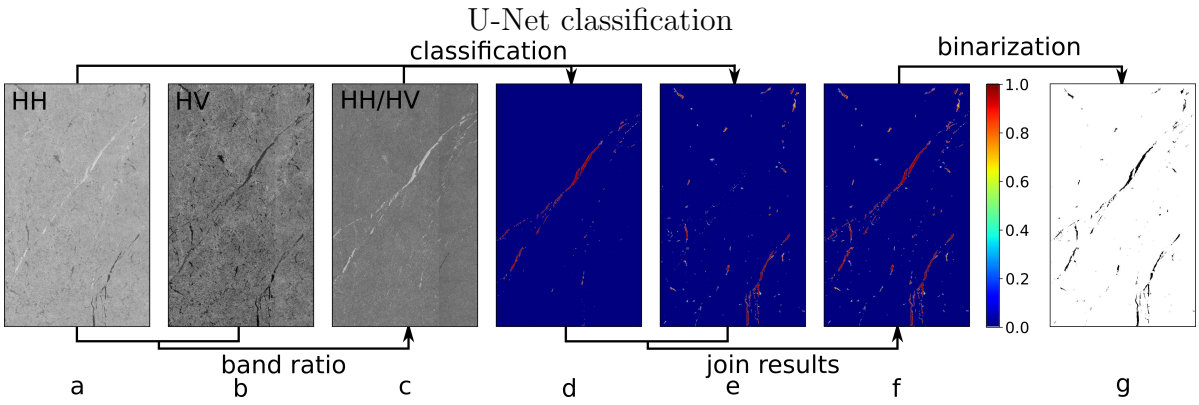

Figure 5.4: Improved lead detection algorithm based on a U-Net convolutional neural network. *a* and *b* are the original Sentinel-1 SAR data (3 Feb 2016, 22:29, Canadian Arctic; size of the area shown is about 150 km by 80 km), HH and HV respectively. *c* is the band ratio HH/HV. *d* and *e* are lead probabilities produced by the lead classification algorithm for dark and bright leads, based on *a* and *c*. U-Net convolutional neural network is used at this step. *f* is the sum of probabilities *d* and *e*. *g* is the binary classification derived from *f* by applying a threshold of 50%.

Figure 5.5. A cutout of the original Sentinel-1 scene taken on 2 January 2019 over the Chukchi Sea is shown in Figures 5.5a,b (the HH channel and the HV channel, respectively). These two images are used as input channels for the both lead detection algorithms, described in Chapter 4 and earlier in this chapter. The probabilistic results for the "dark leads" and "bright leads" of the algorithm based on gray level co-occurrence matrix and random forest classifier are shown in Figure 5.5c,d. The corresponding results from the algorithm based on the U-Net convolutional neural network are shown in Figure 5.5e,f. The color scheme is same for all the four result images (Figures 5.5c,d,e,f). Binary classifications derived with 50% threshold on probabilities produced with both algorithms are shown in Figure 5.5g,i. Figure 5.5h,j present result of the watershed binarization algorithm (described in Section 4.1.5) applied to probabilities produced by both the GLCM + RFC and U-Net -based algorithms.

5.2.2 Evaluation with optical images

Classification results are compared with Sentinel-2 optical images, Figure 5.6. Sentinel-1 SAR and Sentinel-2 optical images were acquired on 21 March 2019 with 7 hours time difference. Despite changes in the ice field between the SAR and the optical image (Figure 5.6a, b), the major cracks are recognizable on both images and are detected with the lead detection algorithm Figure 5.6c.

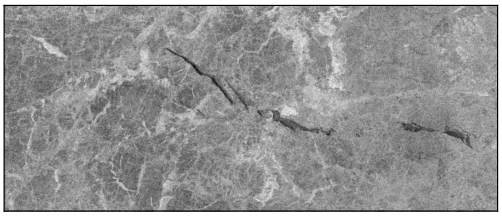

a – HH band

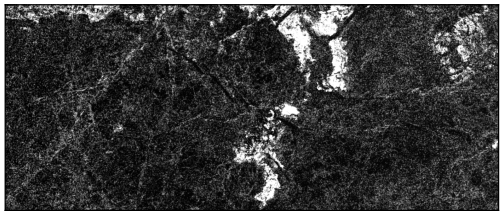

b – HV band

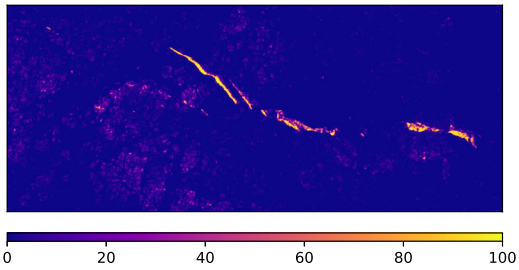

c – GLCM + RFC of a

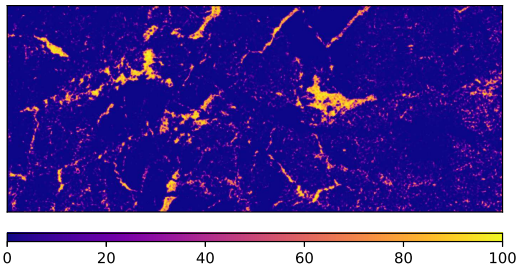

d – GLCM + RFC of the band ratio HH / HV

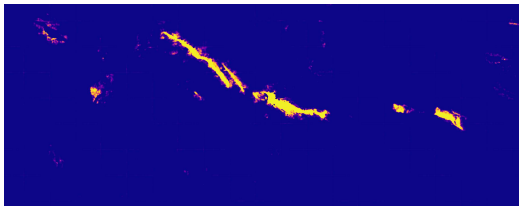

e – U-Net of dark leads

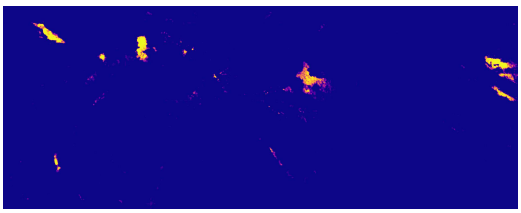

f – U-Net of bright leads

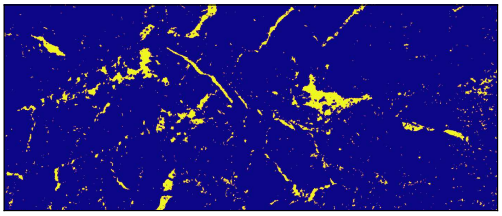

g – 50% threshold binary from c and d

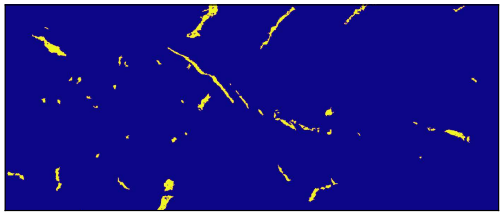

h – watershed + shape filter from c and d

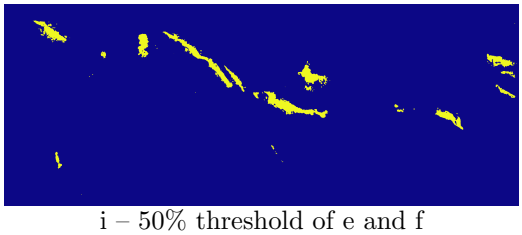

i – 50% threshold of e and f

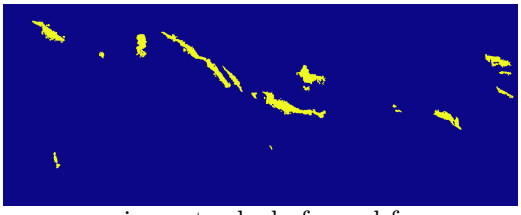

j – watershed of e and f

Figure 5.5: Example of lead classification: *a* and *b* – raw data, HH and HV SAR channels; *c* and *d* – dark (HH) and bright (band ratio) probabilistic lead classifications calculated with the GLCM + RFC algorithm described in Chapter 4; *e* and *f* – dark (HH) and bright probabilistic lead classifications calculated with U-Net; *g* – binary classification calculated by applying a 50% threshold to classifications in *c* and *d*; *h* – watershed binarization and shape-based filter are applied to the probabilistic classifications in *c* and *d*; *i* – binary classification calculated by applying a 50% threshold to classifications in *e* and *f*; *j* – watershed binarization is applied to the probabilistic classifications in *e* and *f*; The scene was taken on 2 January 2019 over the Chukchi Sea, the scene name is `S1B_EW_GRDM_1SDH_20190102T190125_20190102T190220_014319_01AA45_7719`

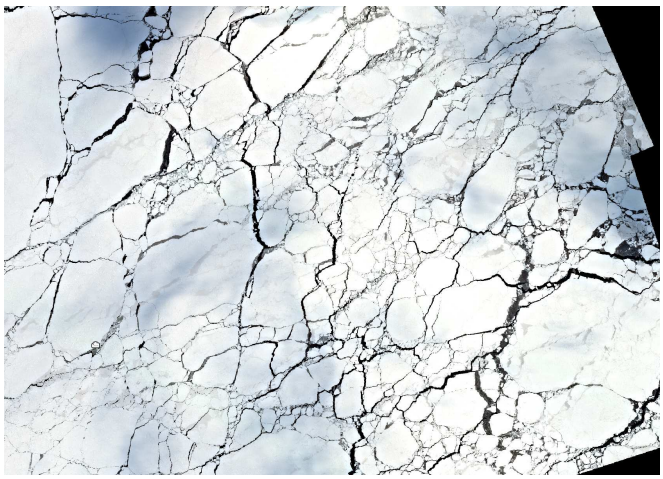

a – Sentinel-2 RGB

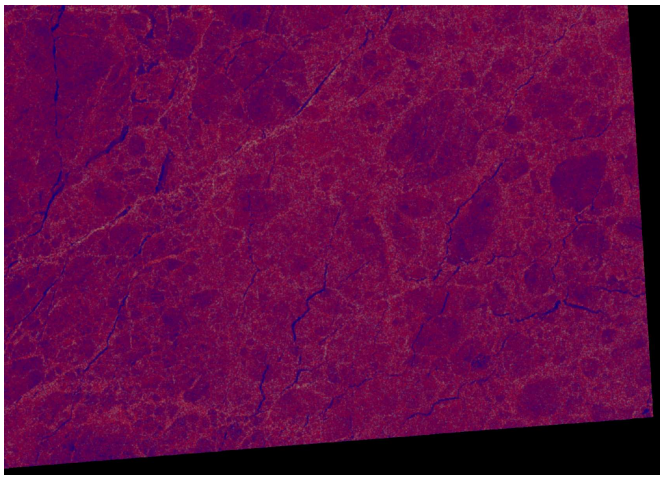

b – Sentinel-1 pseudo-RGB (HH, HV, HV/HH)

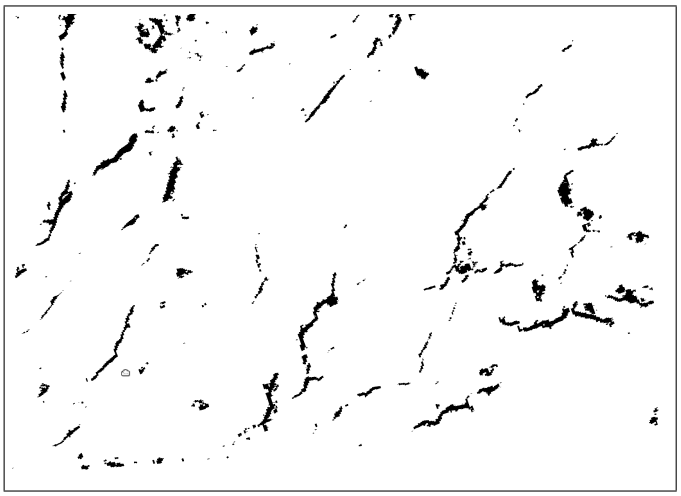

c – binary lead map

Figure 5.6: *a* – Sentinel-2 optical RGB image has been acquired on 21 March 2019 at 9:17UTC, *b* – Sentinel-1 SAR pseudo-RBG (HH, HV, HV/HH) has been acquired on 21 March 21 2019 at 2:32UTC, *c* – result of the lead detection algorithm applied to scene *b*. The shift between SAR and optical image is due to sea ice drift during the 7 hours between the data acquisition times.

5.2.3 Pan-Arctic lead maps

To see the large-scale picture, the improved lead detection algorithm has been applied to all Sentinel-1 scenes acquired over the Arctic on 2 January 2019. The binary lead classification on individual SAR scenes are merged together to produce a pan-Arctic lead map. In case scenes overlap, the information from the latest acquired scene is used. The lead information is then available at the Sentinel-1 EW native 40 meter pixel size Arctic-wide for all regions covered by Sentinel-1 SAR (full coverage with two satellites takes about three days). The high resolution and extent of the map makes it impossible to present it here in full detail as figure. Therefore, the lead area fraction is calculated on a 12 km grid. An pan-Arctic comparison of lead detection results is shown in Figure 5.7. The four images 5.7a,b,c,d correspond to images 5.5g,h,i,j of the fine scale comparison above. That is, Figure 5.7a represents the result of the lead detection algorithm described in Section 4.1.4, Figure 5.7b represents the result of the GLCM + RFC algorithm with watershed binarization applied as described in Section 4.1.5. Figure 5.7c and 5.7d are results of the U-Net based lead detection with 50% threshold and watershed binarization applied, respectively. Figure 5.7d represents the final result of the improved lead detection algorithm. The final lead map in Figure 5.7d shows a more uniform distribution of leads without apparently artificial higher lead fractions along the swath edges. Areas with higher lead fraction like in the Beaufort Sea can clearly be identified despite 12 km grid lead area averaging.

To ensure the algorithm produces stable results, we have applied it to all Sentinel-1 scenes taken over the Arctic in January 2019. Daily lead maps are combined into 3-day composite maps to decrease the amount of gaps where no Sentinel-1 data was acquired. A sea ice mask based on passive microwave sea ice concentration from AMSR2 with 15% threshold is applied to the 3-day composite maps, as described in Section 3.3. To avoid the influence of daily change in sea ice conditions on the estimate for the lead area fraction, the sea ice mask has been shrunk by 10 km in the marginal ice areas and along coastlines with morphological binary erosion. Therefore, areas where sea ice extent is smaller on Sentinel-1 scenes compared to AMSR2 data are not accounted as leads in further analysis. The total lead area and the sea ice area are calculated for each 3-day composite map and are shown in Figure 5.8a. The ratio of the two is presented in Figure5.8b in red. Figure 5.8b also shows lead area fraction derived with the original lead detection algorithm (in green) and open water concentration calculated from the passive microwave sea ice concentration maps cut to the coverage of Sentinel-1 scenes for the corresponding days. All three are calculated on the same extent: areas covered with Sentinel-1 acquisitions and considered as ice-covered areas with AMSR2 data. The AMSR2 point on 2019-01-27 is an outlier due to reduced coverage in passive microwave

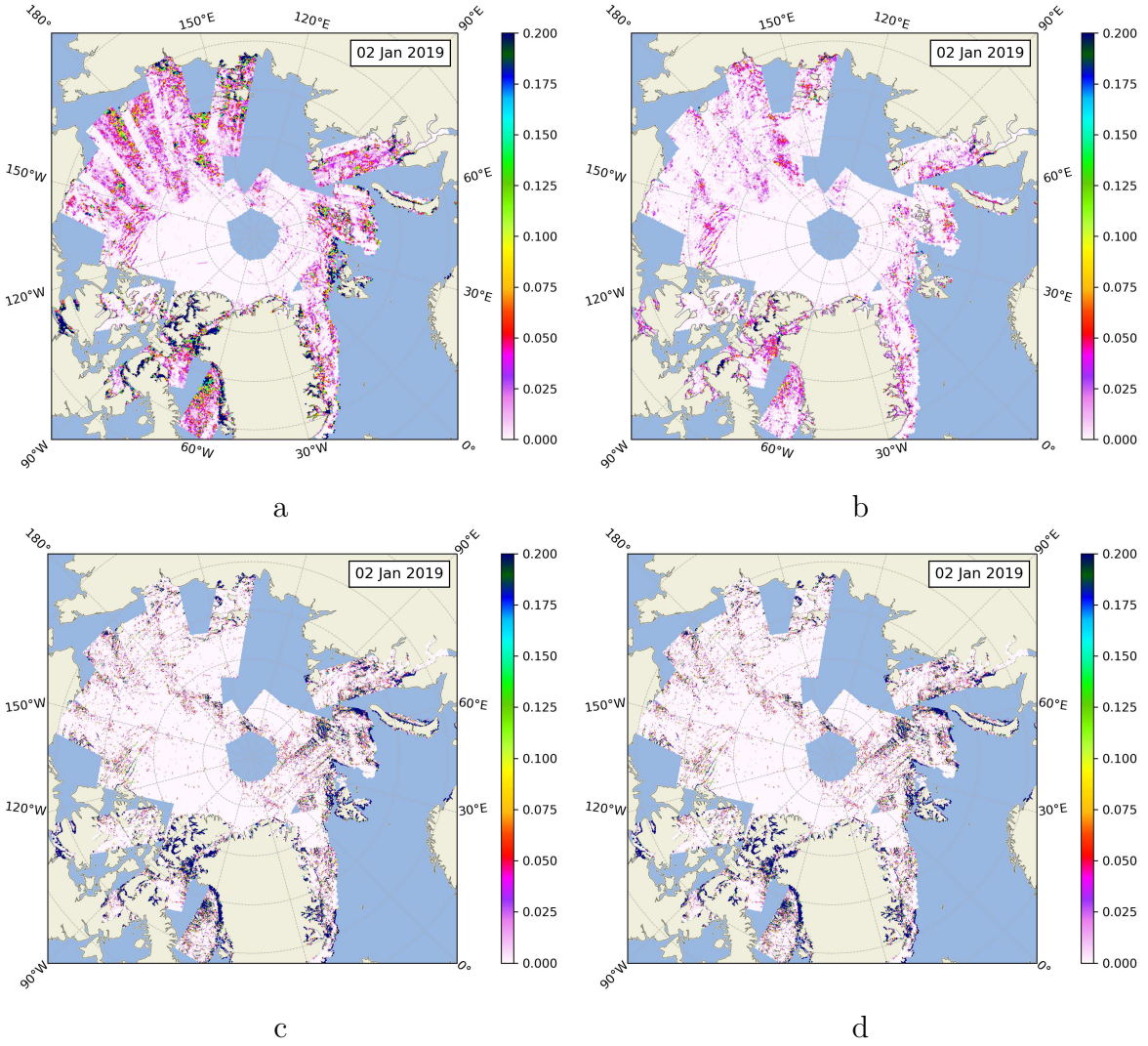

Figure 5.7: Arctic-wide Lead Area Fraction maps (12 km resolution) derived from the daily Arctic lead map. The Arctic lead map consists of all Sentinel-1 scenes acquired over the Arctic on 2 Jan 2019. *a* – Lead Area Fraction derived with the original algorithm based on GLCM features and Random Forest classifier as described in Murashkin et al. (2018). *b* – Lead Area Fraction calculated by replacing the original threshold binarization with the watershed binarization algorithm and with the shape-based filter applied (both described in this paper). *c* – Lead Area Fraction derived with the improved lead detection algorithm based on U-Net CNN. *d* – Lead Area Fraction calculated with the improved lead detection algorithm based on U-Net CNN and watershed binarization applied.

data on the date. According to the CNN-based lead detection, the mean lead area fraction in January 2019 is 2.44% with a standard deviation of 0.25% for the 10 data points of the time series, whereas the GLCM + RFC algorithm proposed earlier shows a mean lead area fraction of 2.3% and 0.7% with standard deviation 0.17% and 0.05% for the basic and shape-filtered cases, respectively. The open water concentration on AMSR2 data is 1.8% with 0.3% standard deviation. Small variations in lead area and sea ice area may appear due to natural reasons, which include lead opening, closing, and refreezing, as well as due to small differences in satellite coverage since sometimes the Arctic is not entirely covered even on 3-day composite maps.

5.3 Discussion

The subswath balancing technique described in Section 5.1.1 adjusts thermal noise by subswath and removes the sudden changes in backscatter between subswaths over a uniform area, which are very noticeable at swath borders, as shown in Figure 5.1. This leads to a smaller backscatter variation in the HV channel, making it more reliable for use as input for automatic classification algorithms.

The classification results shown in Figure 5.5 illustrate the improvement of the U-Net -based lead detection algorithm described in this chapter over the method based on GLCM+RFC described in Chapter 4. On one hand, leads are detected with more confidence (see Figure 5.5c, d, e, and f, scale shows probability of a pixel to be detected as lead), on the other hand, less objects appearing due to scalloping and speckle noise are present in the classified images. This is especially noticeable for bright leads, that have previously been detected from the polarization ratio, which, in turn, had a greater influence of thermal noise. The swath balancing technique described in Section 5.1.1 decrease variation in HV backscatter values appearing due to thermal noise, as shown in Fig. 5.1. The watershed-based binarization method described in Section 4.1.5 makes a significant improvement for the GLCM+RFC lead detection, while has a smaller effect on the U-Net results, as U-Net classification shows higher classification confidence, Figure 5.5.

The Arctic-wide lead maps (Figure 5.7) show a clear improvement in lead detection in the Siberian region of Arctic. This is the region of thin and flat ice, which has low backscatter values. A scene preprocessing that provides a robust backscatter across Sentinel-1 scenes in the area is essential. The use of the watershed-based binarization shows a significant improvement in lead detection quality, which means a lower probabilistic classification confidence in the area. The U-Net -based lead detection algorithm described in Section 5.1.2 shows a significant improvement in performance. While GLCM+RFC algorithm could only be applied to the European Arctic, the U-

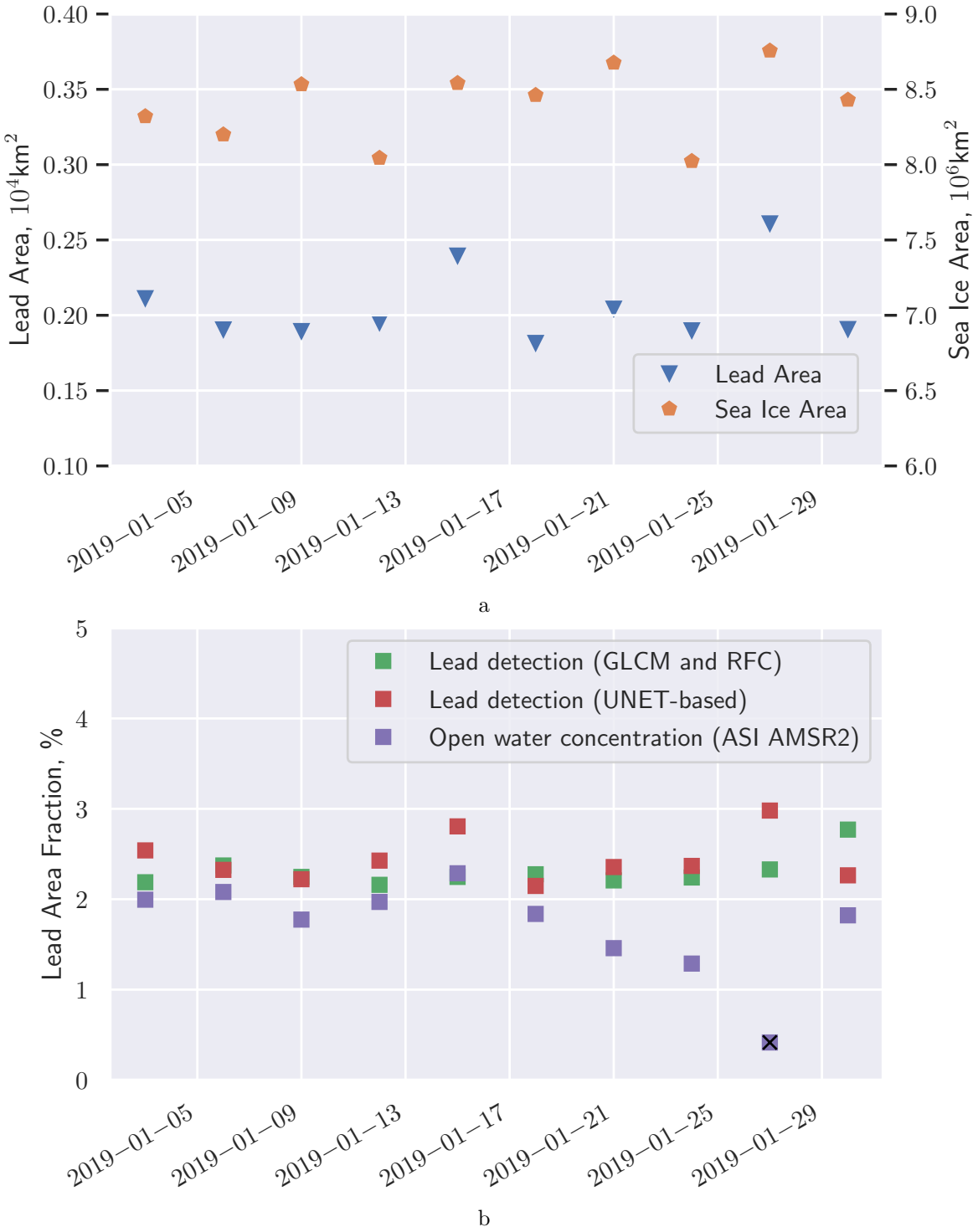

Figure 5.8: *a* Lead area (left y-axis) and sea ice area (right y-axis), and *b* lead area fraction derived from 3-day composite lead maps of the Arctic in January 2019. The sea ice area in *a* mainly changes due to changing satellite coverage (i.e., not due to ice growth/melting).

Net -based method works over the entire Arctic. The higher classification confidence of the U-Net -based probabilistic classification explains the smaller improvement when watershed-based binarization is applied instead of the 50% thresholding.

The lead area and the sea ice area calculated on 3-day composite map are correlated as shown in Figure 5.8a. This indicates the variations in the total lead area partly to come from the variability of Sentinel-1 coverage. The difference in coverage should therefore have little influence on the lead area fraction calculated as a ratio of the lead area to the sea ice area.

Figure 5.8b shows the new algorithm delivering stable results: the lead area fraction (plotted with red) for January 2019 shows small variation with 0.25% standard deviation around its average value of about 2.44%. It is in the same range with the passive microwave open water concentration.

The open water concentration in the central Arctic away from marginal ice area is known to be typically around 1–3% Lindsay and Rothrock (1995); Röhrs and Kaleschke (2012); Maykut (1978). In-situ observations of sea ice thickness in the Central Arctic indicate sea ice cover consists of 1% 0–20 cm thick sea ice (by area) Thorndike et al. (1975). Thus, the 2.44% lead area fraction derived with the improved lead detection algorithm is comparable to the previous studies. A slightly higher lead area fraction compared to passive microwave data is related to a different sensitivity of C-band SAR to thin ice. Refrozen leads with thin flat ice are detected as leads, whereas passive microwave as well as thermal infrared data might be able to distinguish thin ice from open water in the same situation.

Which algorithm to use

Below three lead detection options are considered:

- GLCM and RFC lead detection with 50% threshold on predicted lead probabilities (basic lead detection) described in Section 4.1.4;
- GLCM and RFC lead detection with watershed binarization and shape filter applied (filtered lead detection) introduces in Section 4.1.5 and Section 4.1.6.
- U-Net -based lead detection described above in this chapter in Section 5.1.2.

Lead area fraction variations within January 2019, produces with SAR lead detection are smaller than the variation of open water concentration derived with AMSR2 data. The lead area fraction calculated with the first option is slightly higher than the open water concentration derived with AMSR2 data. However, the two have small correlation of 0.05. The second option has a higher correlation with the passive microwave data, 0.37, but the absolute values are significantly lower compared to AMSR2-derived data. The third option shows the highest correlation to AMSR2 open water concentration of

0.5 and provides a comparable lead area fraction value. Therefore, the U-Net -based lead detection is concluded to provide the best lead detection results of the three option. It will be used further for lead distribution analysis described in the next chapter.

6 Lead distributions in the Arctic Ocean

The distribution of leads and their properties in the Arctic Ocean are analyzed in this chapter. Pan-Arctic map for frequency of lead occurrence for the five winter seasons 2016–2021 is introduced in Section 6.3.2. Lead area fraction is calculated for the entire Arctic and compared to AMSR2 radiometer open water fraction in Section 6.3.1 for the same period of time. Lead area, lead length, lead width, and lead orientation are described in Sections 6.3.4 – 6.3.7. A part of the results presented in this chapter are published in Murashkin and Spreen (2019).

6.1 Sea ice feature scaling

Scaling is the way an observed value changes with the scale of observation. Applying this definition to sea ice cover, one can study dependence of sea ice fracturing processes on the observed scale. As ice floe size and lead size are due to sea ice cover fracturing, these properties are used as proxies for sea ice mechanical properties studies. Sea ice floe size distribution is found to scale with a power law by Rothrock and Thorndike (1984). Weiss (2003) have found the lead size, as a feature related to sea ice cover, to scale with a power law. These observations bring together observation at various scales, which include mesoscale, regional, local observations, and laboratory experiments. According to Weiss (2003), fracturing properties of sea ice scale with a power law from a centimeter to 50 meter scale, based on laboratory studies. On the other size, satellite image analysis done by Lindsay and Rothrock (1995) show sea ice fracturing properties to scale from 1 km scale to 200 km by analyzing distance between leads, which is considered as an indicator for ice flow size. Later, these observations were confirmed with visible imagery (Marcq and Weiss, 2012) on 20 m–2 km scale, CryoSat-2 radar altimetry (Wernecke and Kaleschke, 2015) at 600 m–20 km scale. Similar results based on Helicopter-borne thermal infrared imagery (4–400 m scale) are reported by Thielke et al. (2023). Power law exponents from these studies are summarized in Table 6.1.

Source	Sensor	Scale range	exponent factor
Lindsay and Rothrock (1995)	AVHRR	1-50 km	1.6±0.18
Marcq and Weiss (2012)	SPOT	20 -2 km	2.1-2.3 2.5-2.6
Wernecke and Kaleschke (2015)	CryoSat-2	600 m-20 km	2.47±0.04
Qu et al. (2019)	MODIS, Landsat-8	300 -20 km	2.241-2.346
Thielke et al. (2023)	Helicopter IR	4-300m	2.26-2.61

Table 6.1: Power law exponents derived in previous studies

6.2 Methods

The lead detection algorithm described in the previous chapter is applied to each Sentinel-1 EW GRDM scene acquired over the Arctic Ocean during winter seasons, 1st November – 30 April, 2016–2021, when two Sentinel-1 satellites, A and B, were operational. Then, 3-day composite pan-Arctic lead maps are produced by merging three consecutive daily pan-Arctic maps, as described in Section 4.1.7. This is done to increase the spatial coverage in the areas which are not covered daily with Sentinel-1 scenes.

The data for the five seasons is combined into a frequency of lead occurrence map. Arctic Ocean is split into the following regions: Fram Strait, Barents Sea, Kara Sea, Laptev Sea, East Siberian Sea, Chukchi Sea, Beaufort Sea, Central Arctic, as shown earlier in Figure 1.5, defined by Meier et al. (2007). Each region is cut from a pan-Arctic lead map in a projection, where north is at the top of the region, except for the Central Arctic. Lead area fraction shown in Figures 6.1,6.2 and frequency of lead occurrence shown in Figures 6.5,6.6,6.7 illustrate these regions in the corresponding projections. The regional lead area fraction time series is calculated based on the regional binary lead maps.

Properties distribution for single leads identified on binary regional maps are analyzed. A group of adjacent lead pixels of the 3-day composite binary lead map is considered as a single lead object. Lead objects at a distance of two pixels are also considered as a single lead. For each lead the following lead shape properties are discussed in this chapter:

- lead area
- lead length
- lead width
- lead orientation

These properties are based on shape descriptors introduced in Section 4.1.6. Lead area distribution is directly calculated from areas of identified leads. Lead length is ap-

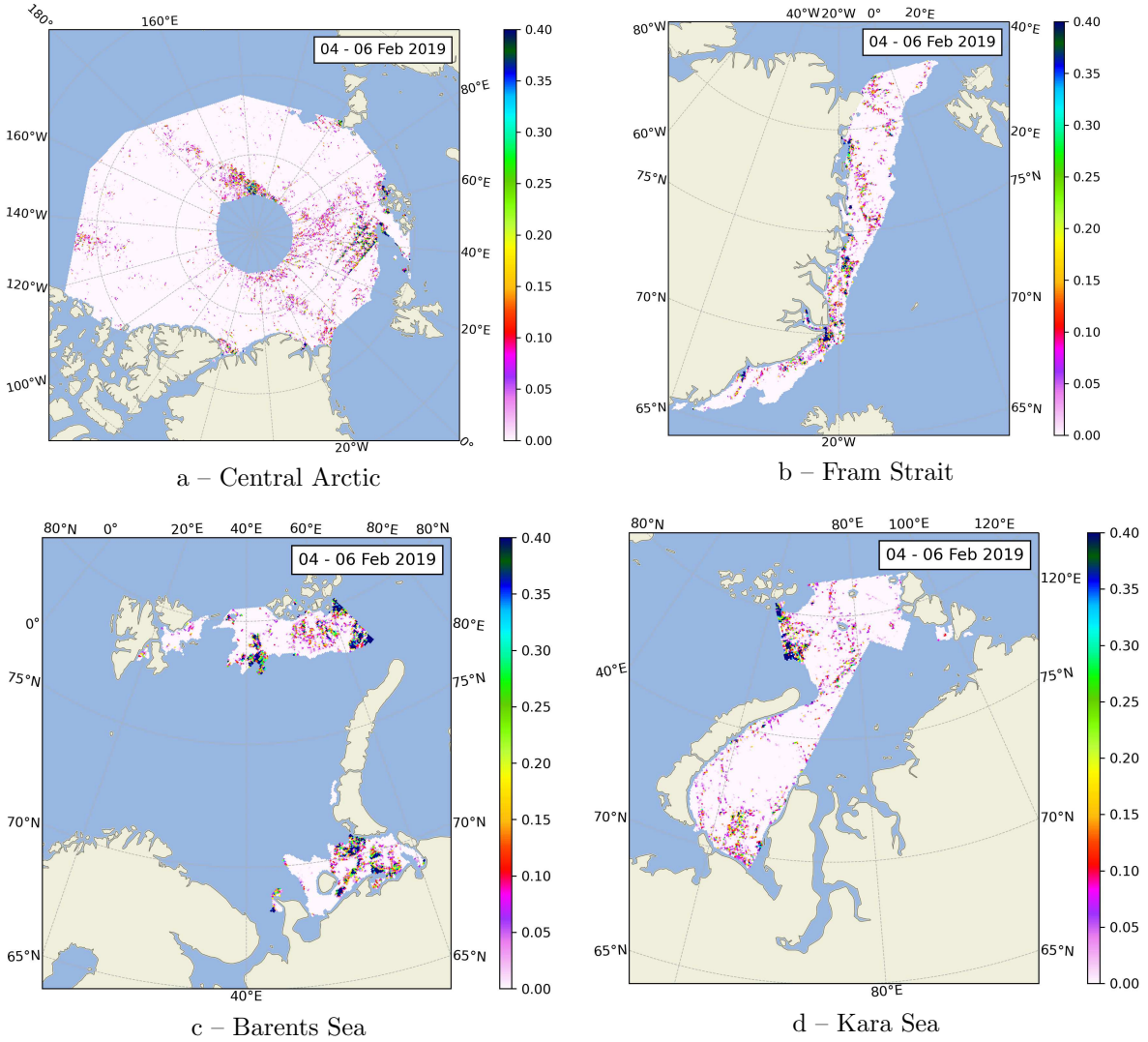

a – Central Arctic

b – Fram Strait

c – Barents Sea

d – Kara Sea

Figure 6.1: Lead area fraction in Arctic regions in corresponding regional projections for *a* Central Arctic, *b* Fram Strait, *c* Barents Sea, *d* Kara Sea. Regional lead area fraction maps on 12 km grid are derived from 3-day composite pan-Arctic binary lead maps with 40 m resolution. Four more regions are shown in Figure 6.2.

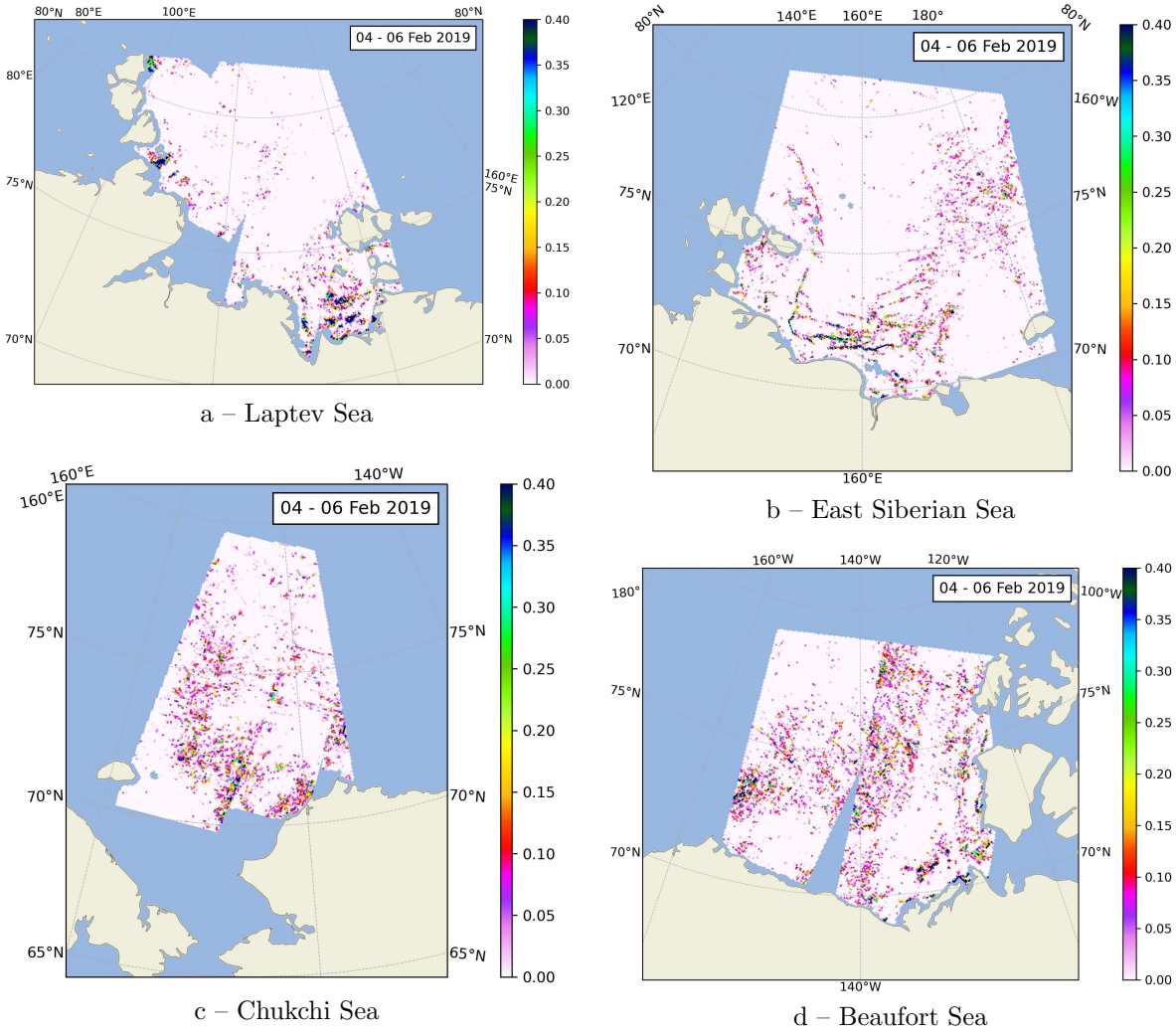

Figure 6.2: Lead area fraction in Arctic regions in corresponding regional projections for *a* Laptev Sea, *b* East Siberian Sea, *c* Chukchi Sea, *d* Beaufort Sea. Regional lead area fraction maps on 12 km grid are derived from 3-day composite pan-Arctic binary lead maps with 40 m resolution. Four more regions are shown in Figure 6.2.

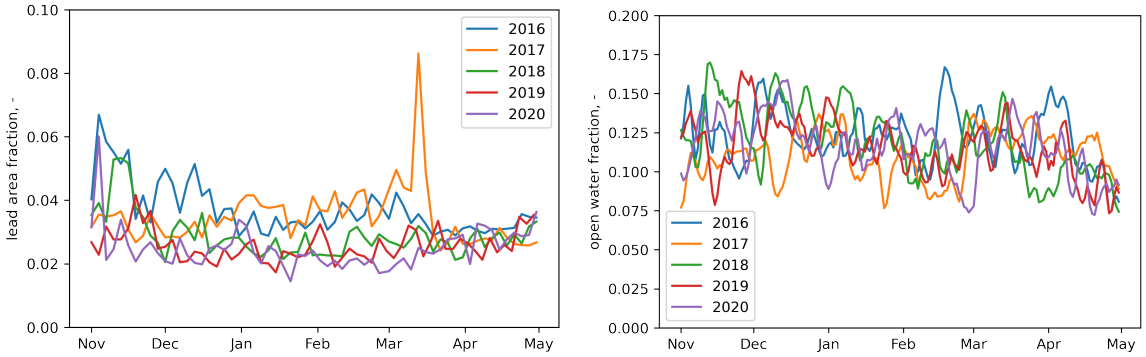

a – SAR lead area fraction

b – MODIS lead area fraction

Figure 6.3: Lead area fraction during winters 2016–2021. *a* – Lead area fraction derived from Sentinel-1 SAR scenes with the algorithm described in Chapter 6. *b* – Lead area fraction calculated from MODIS data by Willmes and Heinemann (2015); Reiser et al. (2020).

proximated with *major axis length* and *skeleton length* parameters, lead width is approximated with *effective width* descriptor. Lead orientation is the orientation of the approximating ellipse and is calculated relatively to the region projection, shown in Figures 6.1 and 6.2. The orientation angle of 0° corresponds to a horizontal line on images, angle values increase from –90° to 90° counter-clockwise.

6.3 Results

6.3.1 Lead area fraction

Ratio of area covered with leads to the total area covered with sea ice, the lead area fraction, is calculated for each 3-day composite binary lead map, shown in Figure 6.3a. For comparison, Figure 6.3b shows lead area fraction derived from MODIS lead maps by Willmes and Heinemann (2015); Reiser et al. (2020). Average SAR lead area fraction is lower than the one derived from MODIS. It shows less variability within a single year, but more variability between years. Lead area fractions are summarized in Table 6.2. The average lead area fraction is between 3.7% and 2.5% for years 2017–2021 with average value of 3.0%.

6.3.2 Frequency of lead occurrence

Frequency of lead occurrence is calculated based on 3-day composite binary lead maps for winter seasons 2016–2021, shown in Figure 6.4a. For comparison, frequency of lead occurrence is also calculated from lead maps derived from MODIS infrared images by Willmes and Heinemann (2015); Reiser et al. (2020). The two maps cut to a regional

	SAR		MODIS	
year	LAF	STD	LAF	STD
2017	0.037	0.008	0.123	0.020
2018	0.035	0.009	0.110	0.016
2019	0.029	0.007	0.120	0.023
2020	0.026	0.005	0.116	0.020
2021	0.025	0.006	0.116	0.021
total	0.030	0.009	0.117	0.021

Table 6.2: Average lead area fraction (LAF) and standard deviation per year calculated from Sentinel-1 and MODIS data.

scale are shown in Figures 6.5,6.6,6.7. Patterns occurring on the MODIS frequency of lead occurrence maps are discussed by Willmes et al. (2023). Similar patterns for the frequency of lead occurrence are present on both datasets between Svalbard and Franz Josef Land, around Severnaya Zemlya archipelago, Beaufort Sea, Baffin Bay, Fram Strait. Most differences occur in Canadian Arctic, where sea ice forms under more calm conditions. There is less wave and current influence on the sea ice, which, therefore is less ridged compared to the Arctic Ocean, which leads to smoother sea ice surface, which appears radiometrically similar to the surface of refrozen leads.

Figure 6.4a also shows straight line patterns that correspond to Sentinel-1 swath borders, most pronounced in Beaufort Sea (Figure 6.7a), and north of Svalbard (Central Arctic region, Figure 6.5a). Despite the incidence angle correction applied to Sentinel-1 scenes as a part of the preprocessing procedure described in Section 4.1.1, the differences in SAR backscatter from various incidence angles cannot be fully neglected. Backscatter depends on physical properties of the scattering surface and underlying scattering volume, both of which, in general case, physically depend on the incidence angle. When scenes are acquired with various geometries throughout season, these differences are smoothed out. This is the case for the season 2016–2017, when scenes have been taken in both the ascending and descending geometry. However, in years 2017–2022 Arctic Ocean have been covered mostly with the descending geometry, according to `https://sentinel.esa.int/en/web/sentinel/copernicus/sentinel-1/observation-scenario`, acquisition plan for 2016–2017 and 2017–2018 are shown in Figure 6.8. As the result, uncertainties are amplified when all scenes taken during the season are stacked together. As expected, leads occur more often around islands, which induce stresses in sea ice moving under wind and current forcing, in the Fram Strait as the main gate for sea ice from Arctic Ocean, Beaufort Sea covered with thicker sea ice.

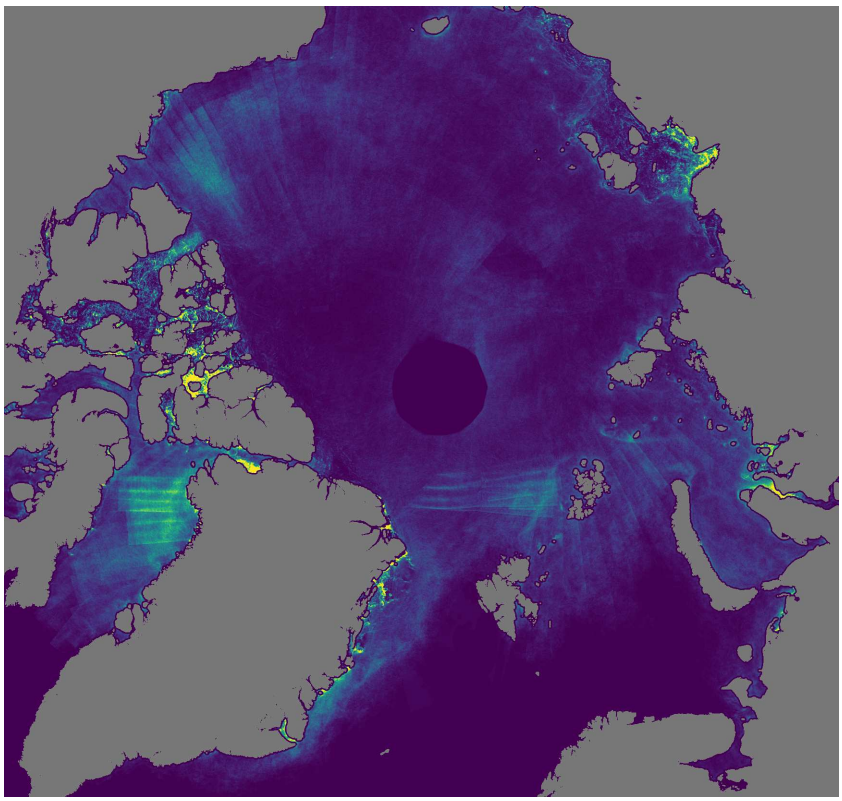

a – SAR lead frequency

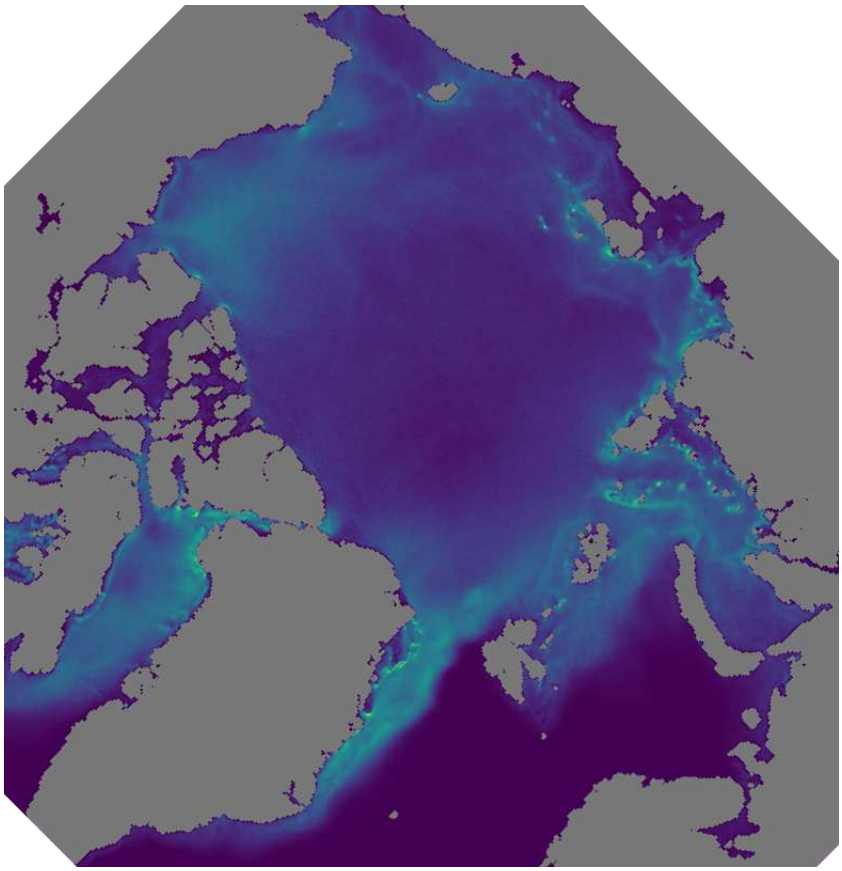

b – MODIS lead frequency

Figure 6.4: Lead frequency of occurrence during winters 2016–2021. *a* – Lead frequency derived from Sentinel-1 SAR scenes with the algorithm described in Chapter 6. *b* – Lead frequency produced from MODIS thermal infrared lead area maps derived by Willmes and Heinemann (2015); Reiser et al. (2020).

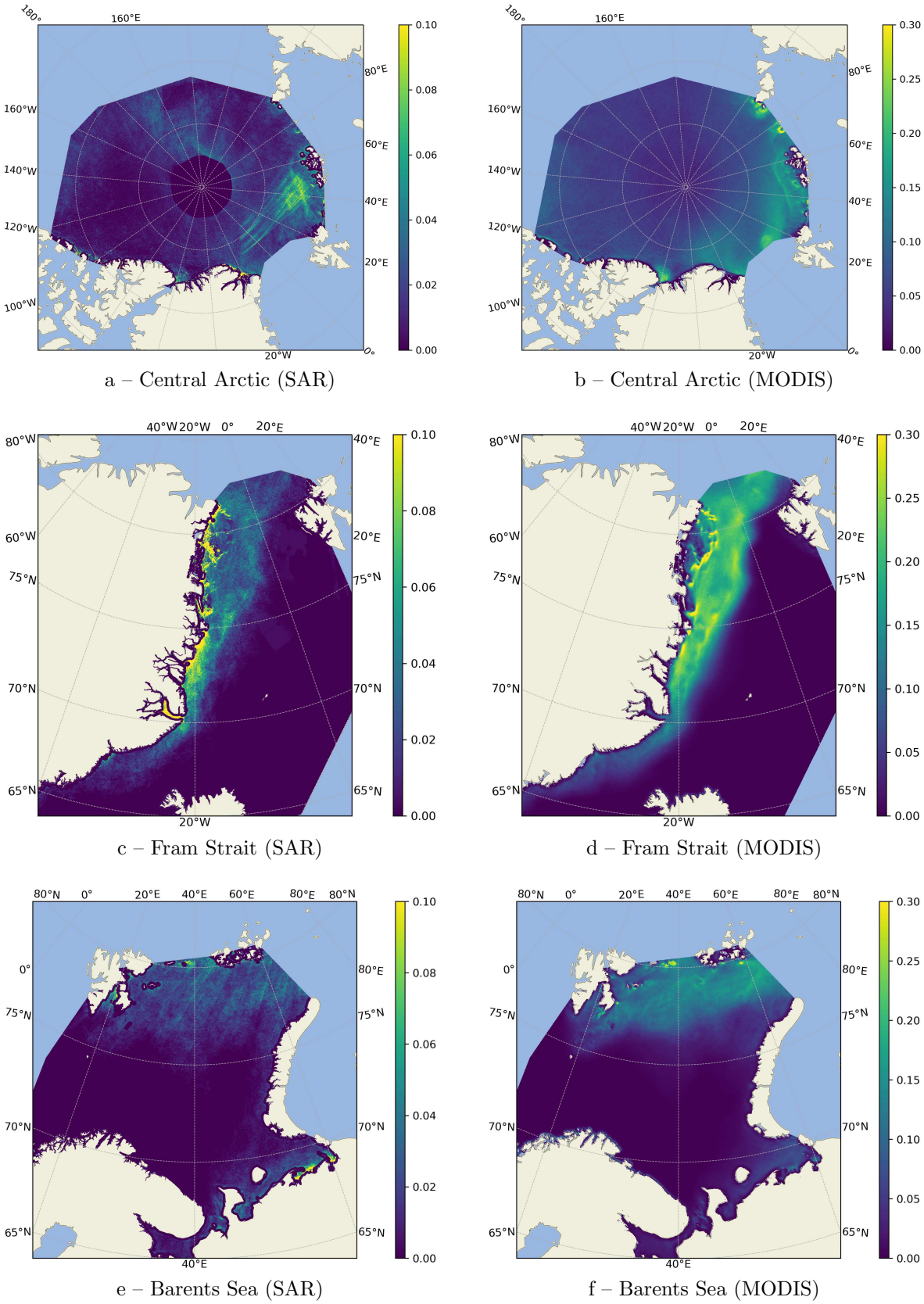

a – Central Arctic (SAR)

b – Central Arctic (MODIS)

c – Fram Strait (SAR)

d – Fram Strait (MODIS)

e – Barents Sea (SAR)

f – Barents Sea (MODIS)

Figure 6.5: Regional lead frequency of occurrence from SAR (left column) and MODIS (right column), both are calculated for 5 winter seasons 2016–2021.

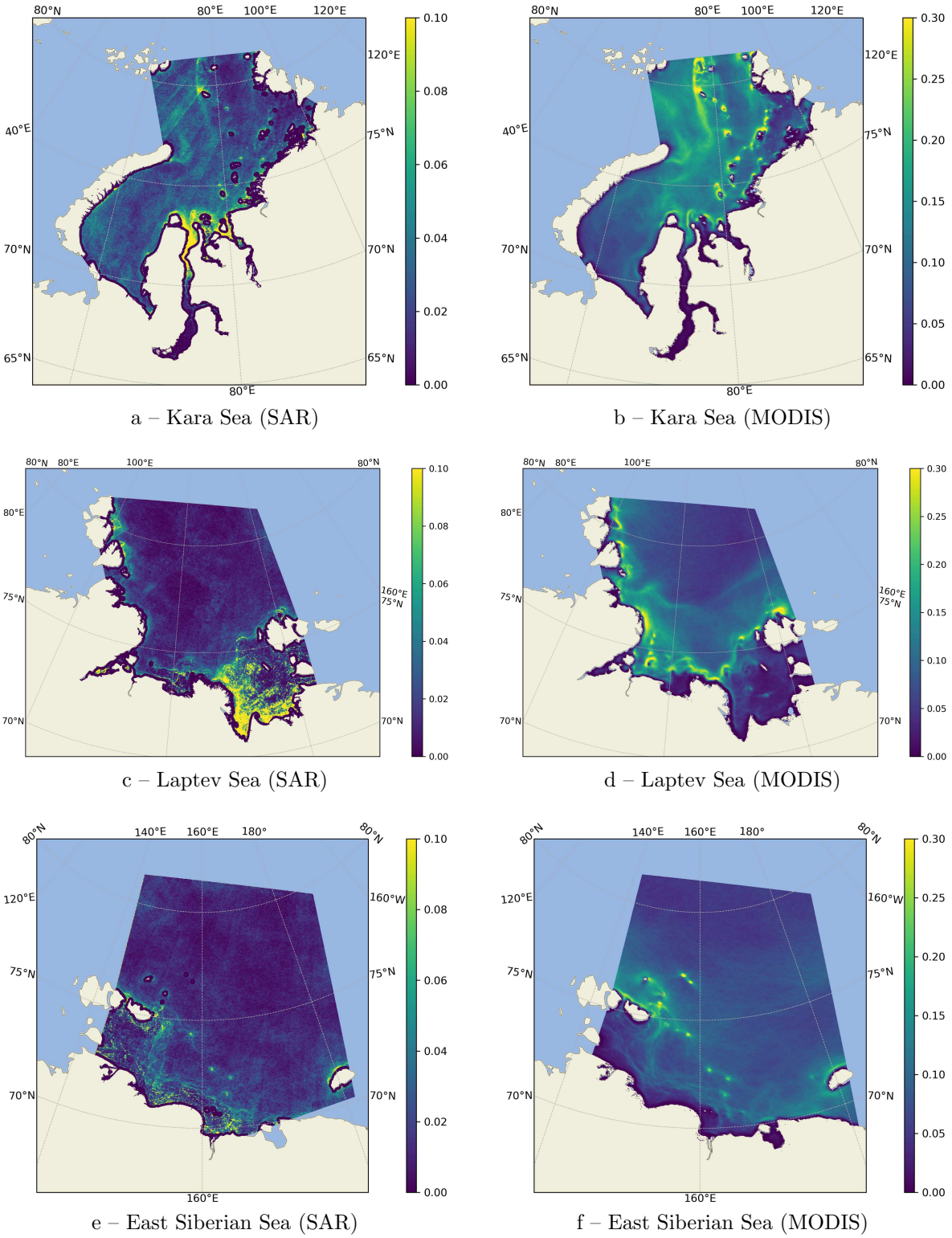

a – Kara Sea (SAR)

b – Kara Sea (MODIS)

c – Laptev Sea (SAR)

d – Laptev Sea (MODIS)

e – East Siberian Sea (SAR)

f – East Siberian Sea (MODIS)

Figure 6.6: Regional lead frequency of occurrence from SAR (left column) and MODIS (right column), both are calculated for 5 winter seasons 2016–2021.

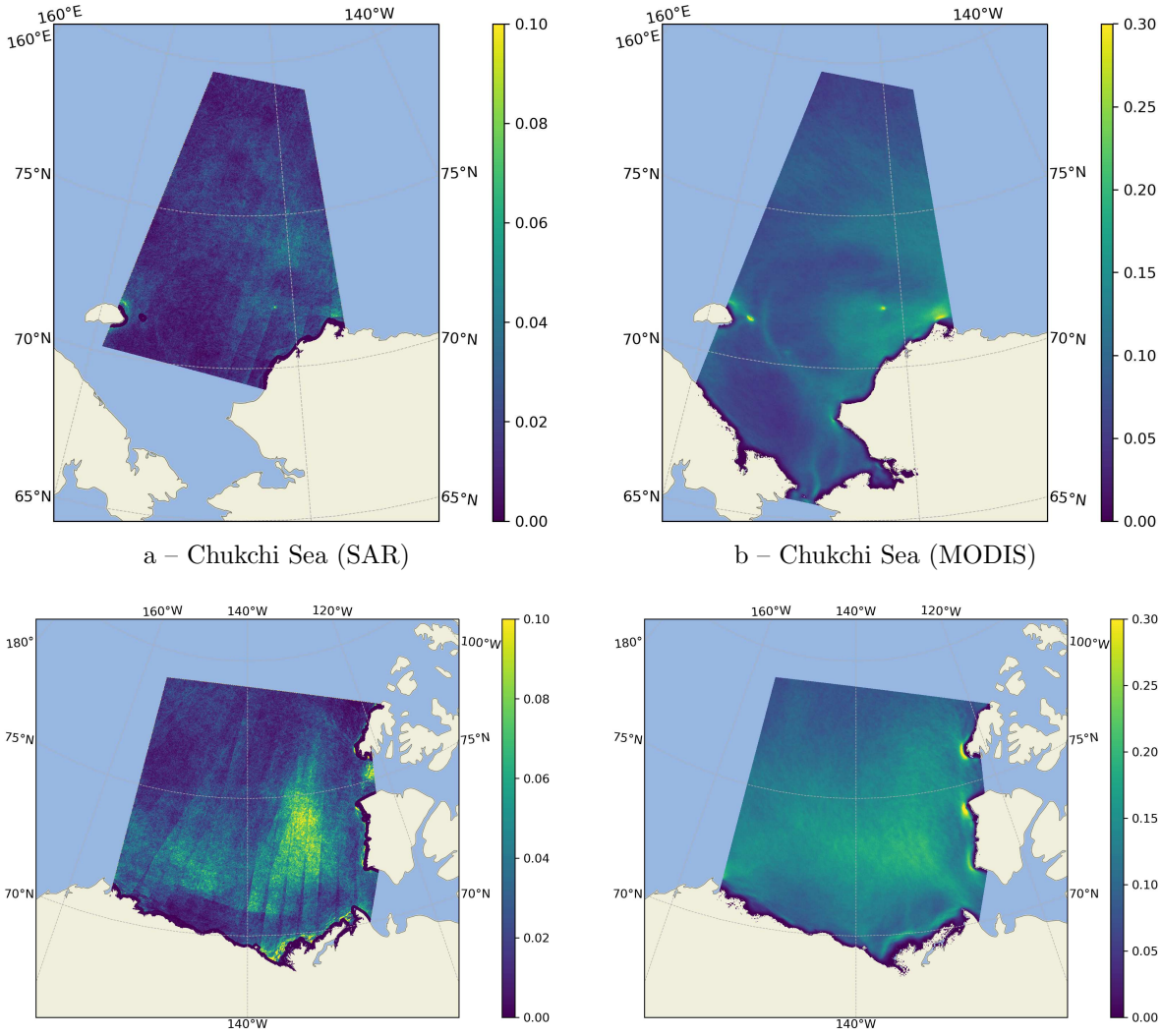

a – Chukchi Sea (SAR)

b – Chukchi Sea (MODIS)

c – Beaufort Sea (SAR)

d – Beaufort Sea (MODIS)

Figure 6.7: Regional lead frequency of occurrence from SAR (left column) and MODIS (right column), both are calculated for 5 winter seasons 2016–2021.

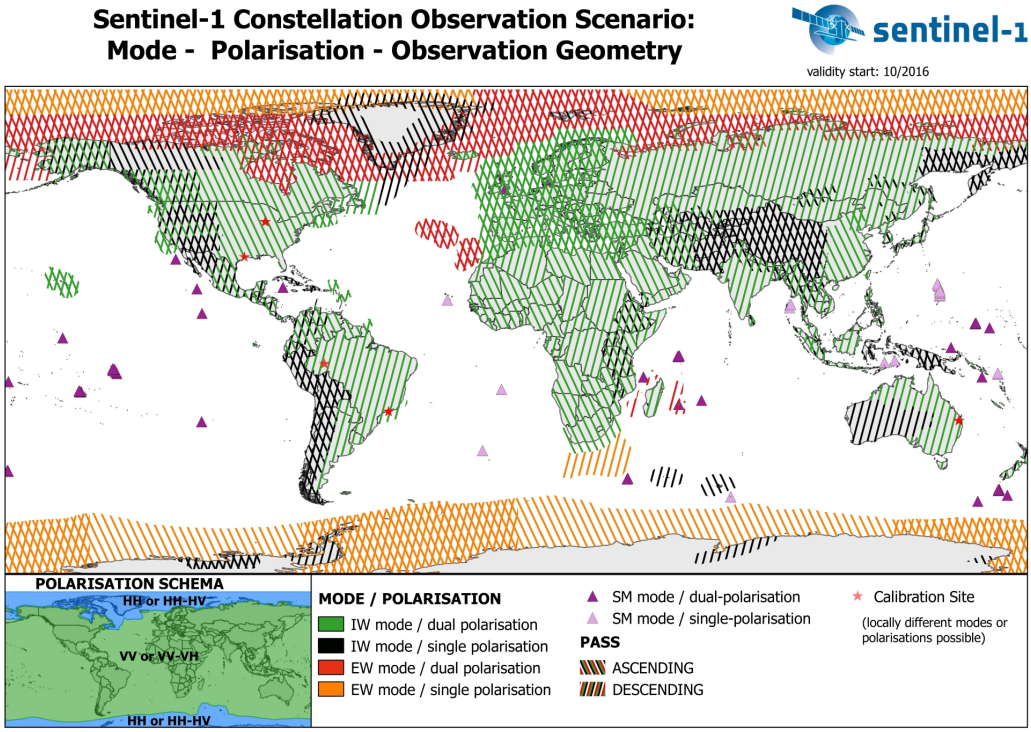

a – Sentinel-1 acquisition plan covering 2016–2017 winter season

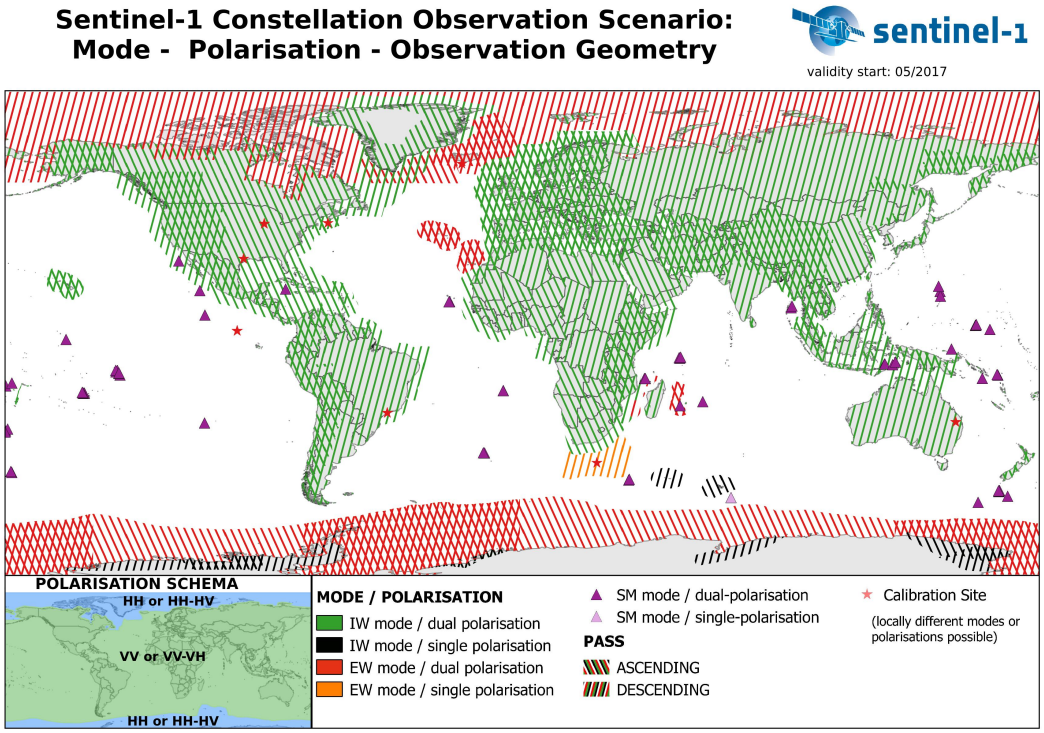

b – Sentinel-1 acquisition plan covering 2017–2018 winter season

Figure 6.8: Sentinel-1 acquisition geometry according to ESA, images from `https://sentinel.esa.int/en/web/sentinel/copernicus/sentinel-1/acquisition-plans/observation-scenario-archive`.

6.3.3 Number of leads

Table 6.3.3 summarized number of leads detected in Beaufort Sea, Barents Sea, Chukchi Sea, East Siberian Sea, Fram Strait, Kara Sea, Laptev Sea, and Central Arctic during winters 2016–2021, the data is visualized in Figure 6.9. Each season is split into three stages: early season – November and December, mid-season – January and February, and late season – March and April. Only leads that are wider than 320 meters, which corresponds to 8 pixels in the native Sentinel-1 pixel spacing, are accounted here because more narrow leads are not reliably detected as it will be shown later in Section 6.3.6. Number of leads is increasing throughout a season in the areas, where sea ice extent increases. This is especially noticeable in the Barents Sea and the Fram Strait. Beaufort Sea shows increase in number of leads late in the season, while the increase from November till end of February is smaller than inter-annual variations in lead number. Kara Sea, Laptev Sea, and East Siberian Sea do not show increase in lead number throughout winter seasons.

6.3.4 Lead area distribution

Distribution of lead area for each of the eight defined regions is present in Figure 6.10. Despite variations in lead number, the normalized lead area distribution does not show any changes during winter seasons in most cases. The largest leads up to 3200 km^2 are found in the Barents Sea, Kara Sea, and Laptev Sea, while in the Beaufort Sea, Central Arctic, and East Siberian Sea leads only reach about 1600 km^2. Areal distribution of leads in Chukchi Sea shows decrease in lead size from early to mid- and late season. All distributions show a maxima at around 50–60 square pixels, 0.08–0.10 km^2. This indicates leads, smaller than the size, are not reliably detection with the lead detection algorithm described in Chapter 5. The change in distribution slope at around 2000 pixels, 3.2 km, is not expected (details are provided in Section 6.1) and is likely to come from SAR image processing. This effect will further be discussed in Section 6.3.5 describing lead length distribution.

6.3.5 Lead length

Lead length is estimated as the major axis length of an ellipse approximating the detected object (shown in Figure 6.11), and as a length of the detected object skeleton (show in Figure 6.12). By definitions described in Section 4.1.6, major axis length overestimates the length of the detected object, while skeleton length underestimates it. The peak in distributions shows the minimal length of leads that are reliably detected, 10–20 pixels or 400–800 m in both the major axis length and the skeleton length approximations.

		Beaufort Sea	Barents Sea	Central Arctic	Chukchi Sea	East Siberian Sea	Fram Strait	Kara Sea	Laptev Sea
2016-2017	early	104610	18312	294215	101261	159792	84643	129286	166014
	mid	72779	69972	417532	79505	138641	102215	178724	125164
	late	86386	125213	551003	56399	163534	197393	201228	169678
2017-2018	early	131630	18649	562759	67424	181552	85349	177980	157008
	mid	155764	66232	657160	88849	126814	63266	168672	203622
	late	175381	126762	591078	71603	112381	89341	127644	122725
2018-2019	early	139586	14979	209249	118302	212040	50820	142415	112553
	mid	124239	66599	233768	85156	107682	64468	94804	63479
	late	202723	105839	237350	67587	100870	116490	124446	63914
2019-2020	early	142612	40033	180681	110649	197011	97106	162233	33027
	mid	172218	90178	210489	96787	127983	51447	112402	36163
	late	245018	121559	217584	34249	154500	114021	130703	43424
2020-2021	early	117280	20901	235215	83910	151161	87985	108657	72148
	mid	123495	103623	202377	50951	78817	104751	160365	25348
	late	209264	102040	239916	62644	152317	113298	122420	51313
2017-2021	early	635718	112874	1482119	481546	901556	405903	720571	540750
	mid	648495	396604	1721326	401248	579937	386147	714967	453776
	late	918772	581413	1836931	292482	683602	630543	706441	451054

Table 6.3: Number of leads in regions of the Arctic Ocean during early (November – December), mid- (January – February), and late (March – April) season during years 2016–2021.

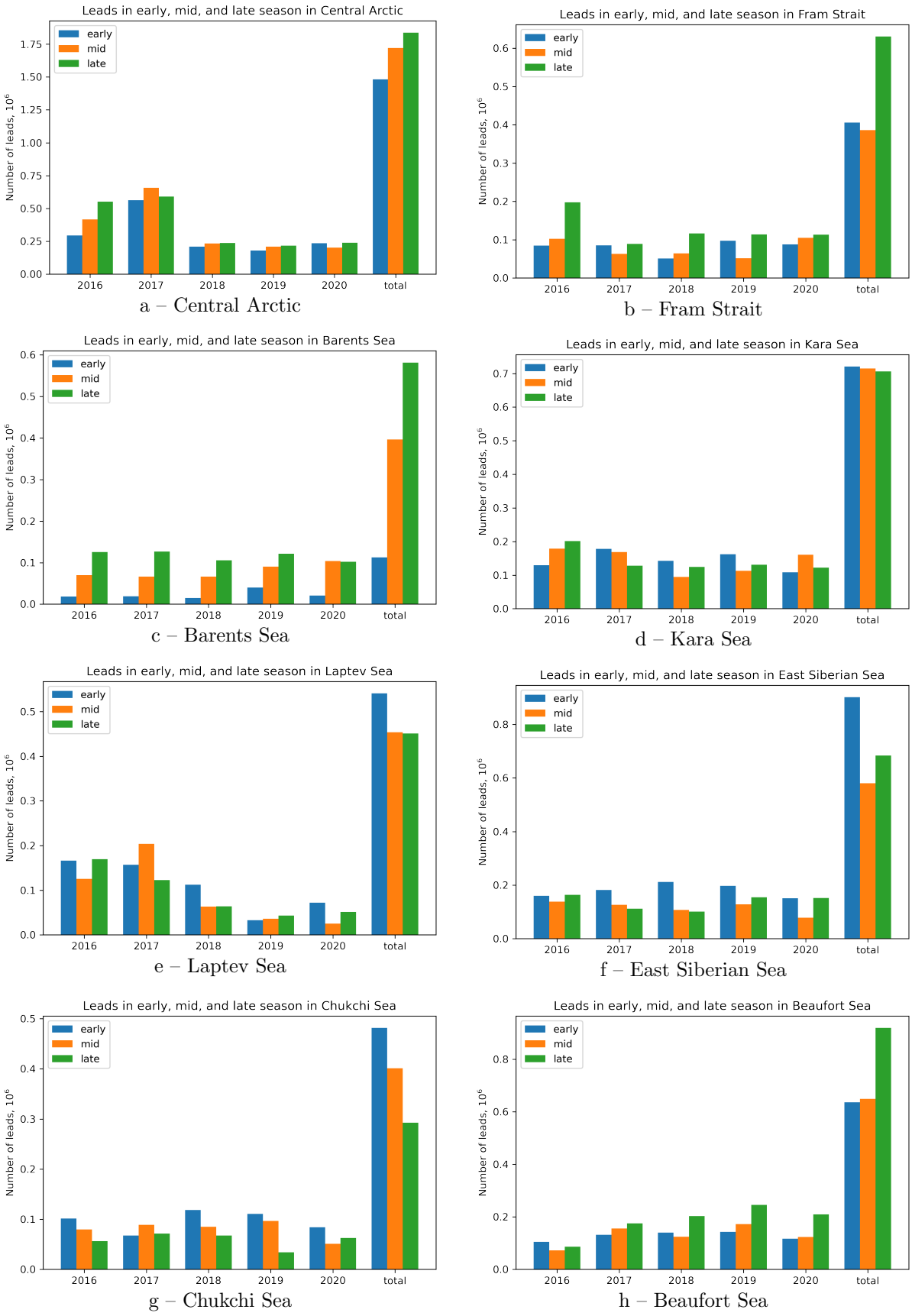

Figure 6.9: Number of leads in early (November–December, in blue), mid (January–February, in orange), and end season (March–April, in green) in 2016–2021 per Arctic region.

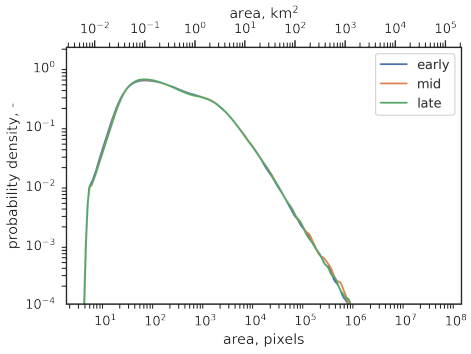

a – Central Arctic

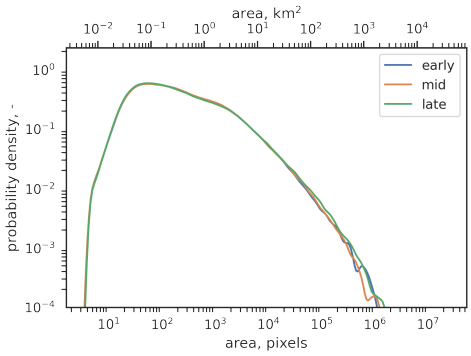

b – Fram Strait

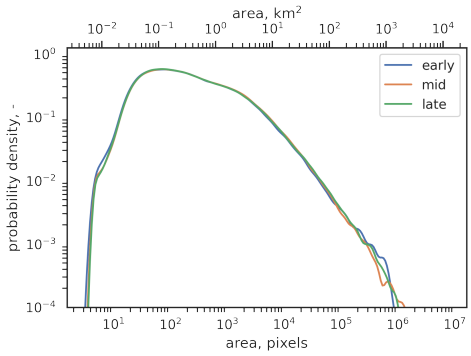

c – Barents Sea

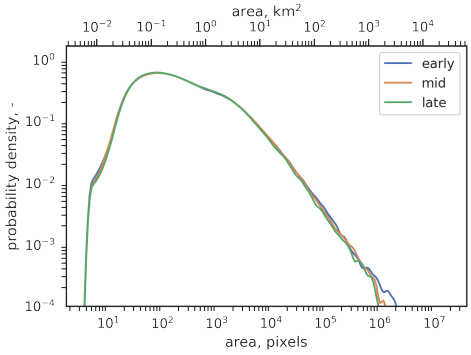

d – Kara Sea

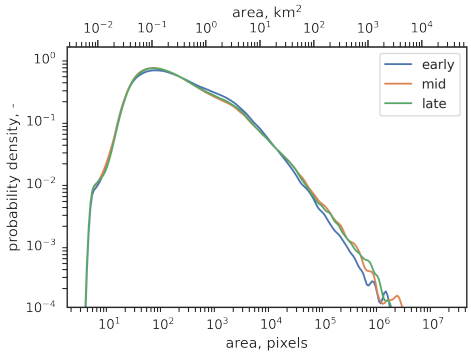

e – Laptev Sea

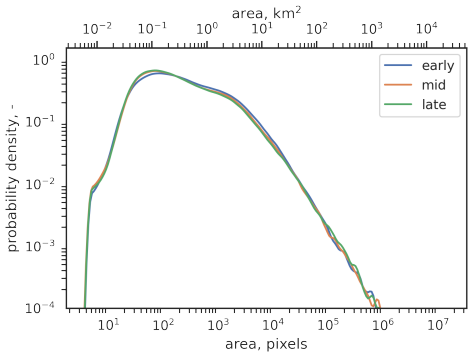

f – East Siberian Sea

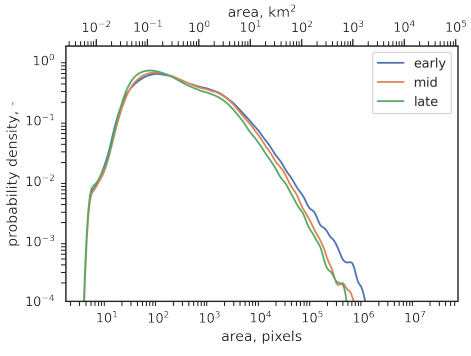

g – Chukchi Sea

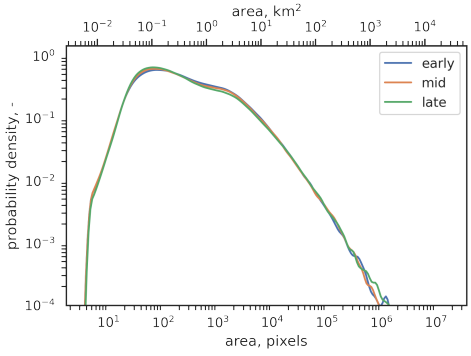

h – Beaufort Sea

Figure 6.10: Regional lead area distribution at log-log scale, size is given in pixels, 40 m × 40 m = 160 m² size. The distributions are calculated for the five winter seasons, separately for early season (November, December) in blue, mid-season (January, February) in orange, and late season (March, April) in green.

The inclination of the lead length distributions show a change at a characteristic length of 30–60 pixels, which corresponds to 1.2–2.4 km. The change is likely to come from the lead detection algorithm since 32 pixels and 64 pixels are two characteristic sizes within the U-Net -based architecture shown in Figure 5.1.2. However, the mechanism of these specific sizes influence on distribution of lengths is uncertain. It should also be noticed that the change in the distribution slope effect is NOT coming from:

- SAR subswath size is around 80 km, which is much larger that the characteristic length;
- SAR scalloping noise pattern size is about 500 pixels and is not comparable with the characteristic length;
- shape filter described in Section 4.1.6 is not used after the U-Net -based lead detection;
- image warping does not introduce any defects at the characteristic length.

Oscillations in skeleton length distributions for short leads come from pixel discretization, as skeleton length directly counts number of pixels in the morphological skeleton and can only be an integer. On major axis length distributions the oscillations are not present as the major axis length is calculated from the ellipse parameters and, therefore, may be a floating number. Lead lengths up to 4000 pixels, 160 km, are often detected in all regions except of the Barents Sea and Chukchi Sea, where leads are shorter. The difference in the maximal lead length between the major axis length approximation and the skeleton length approximation is small.

6.3.6 Lead width

Lead width is estimated through the effective width parameter which is calculated as lead area divided on major axis length of the approximation ellipse corresponding to the detected object, shown in Figure 6.13. Lead width distribution is expected to follow the power law according to Weiss (2003). The significant deviation from a power law is observed as lead widths below 5 pixels, or 200 m, therefore this size is set as a threshold for reliably detected leads, used earlier in Section 6.3.3. More narrow leads are also detected, however a notable amount of them are missed with the lead detection algorithm. The exponent of the power law for the lead width distributions shown in Figure 6.13 is 1.86 with 0.16 standard deviation, which is comparable to the value 1.6 ± 0.18 reported by Lindsay and Rothrock (1995), but lower compared to other studies summarized in Table 6.1. It should be noticed that according to the definition given in Section 4.1.6, effective width is an average width of the detected objects, while width may change from smaller to larger values for a single object. Although the total number of leads change throughout winters, the lead width distribution does not show any change with time,

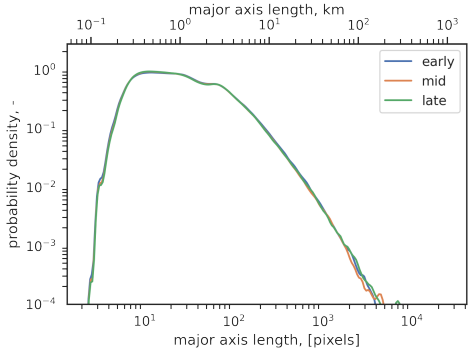

a – Central Arctic

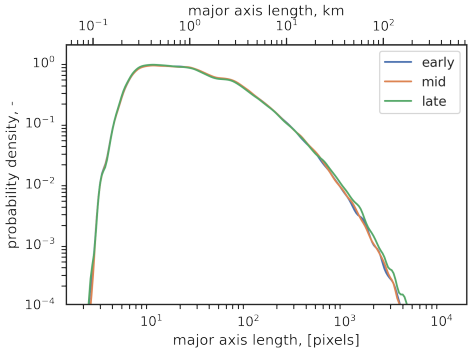

b – Fram Strait

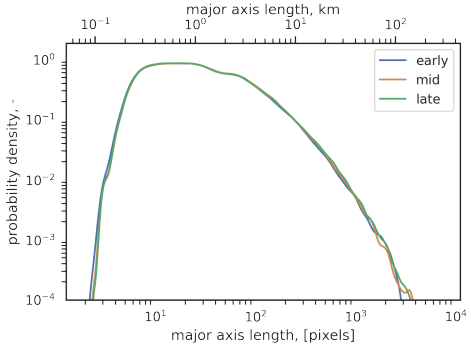

c – Barents Sea

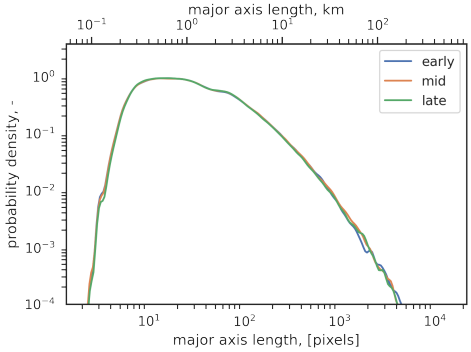

d – Kara Sea

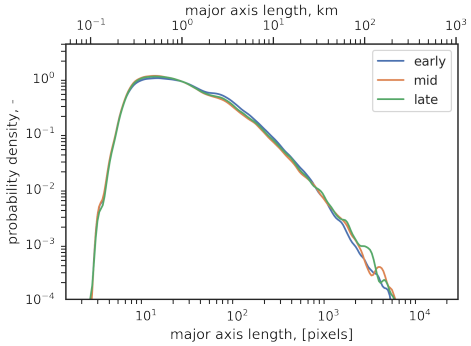

e – Laptev Sea

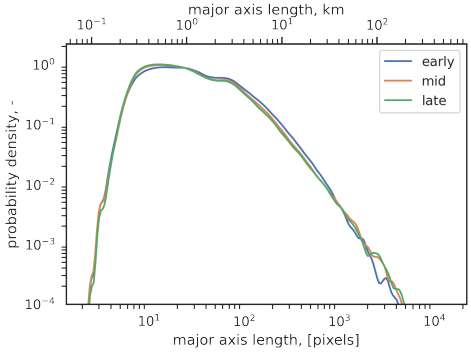

f – East Siberian Sea

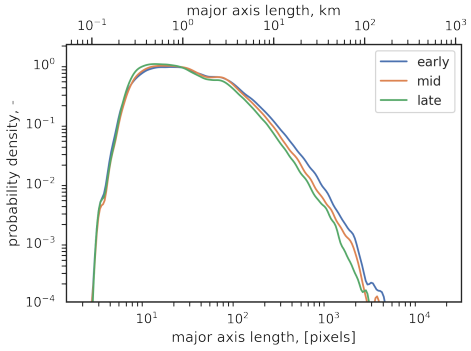

g – Chukchi Sea

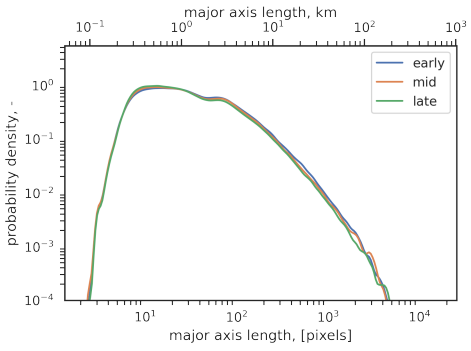

h – Beaufort Sea

Figure 6.11: Regional lead major axis length distribution as an overestimating lead length approximation, at log-log scale, size is given in 40 m pixels.

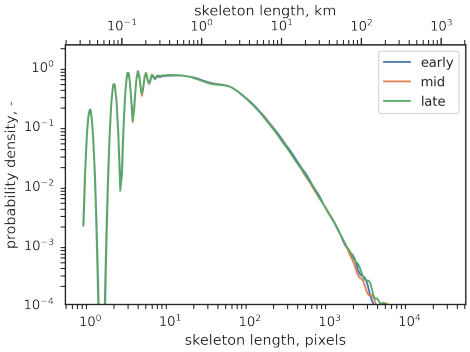

a – Central Arctic

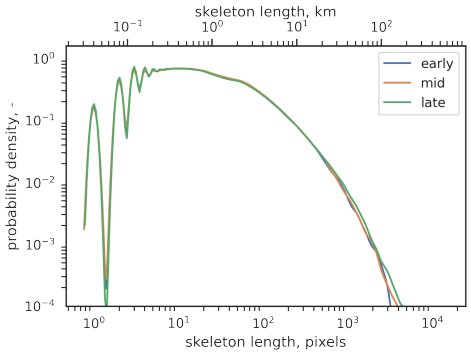

b – Fram Strait

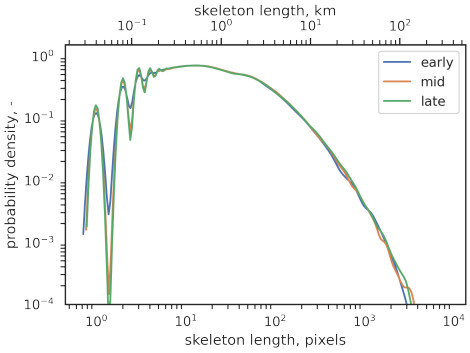

c – Barents Sea

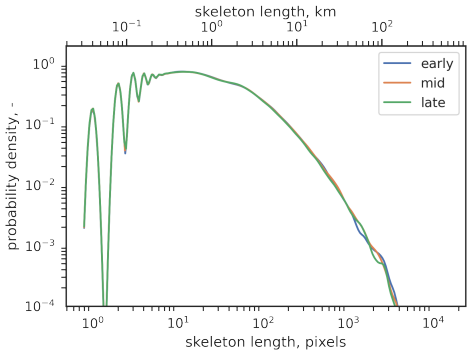

d – Kara Sea

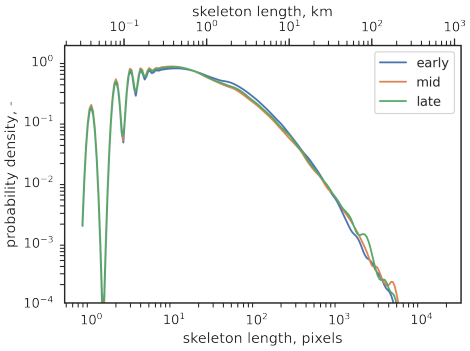

e – Laptev Sea

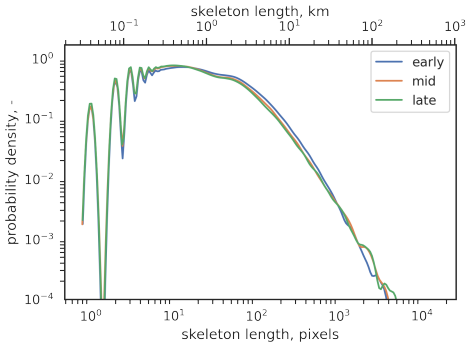

f – East Siberian Sea

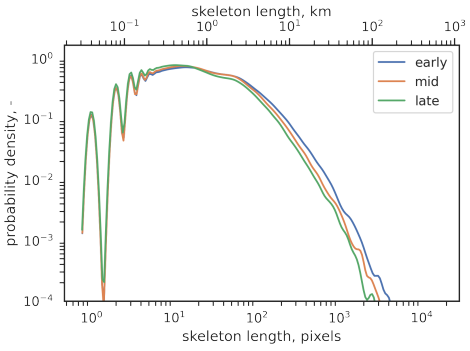

g – Chukchi Sea

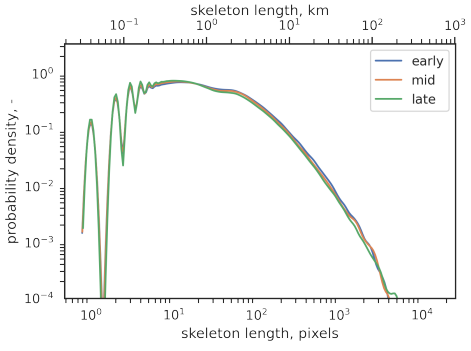

h – Beaufort Sea

Figure 6.12: Regional lead skeleton length distribution as an underestimating lead length approximation, at log-log scale, size is given in 40 m pixels.

except of the wider leads present in the Chukchi Sea earlier in winter seasons.

6.3.7 Lead orientation

Lead orientation distribution shows if there is a preferred direction for leads to occur. It is calculated regionally, relatively to the region projection as shown in Figures 6.1 and 6.2, and is presented in Figure 6.14. The orientation angle of 0° corresponds to a horizontal line in the projection, angle values increase from –90° to 90° counter-clockwise.

Each of the Arctic Ocean regions show non-uniform lead orientation distribution. In the Central Arctic more leads are oriented at 30° angle, perpendicular to the direction towards Fram Strait. Throughout a winter the dependence becomes more pronounced. Fram Strait, in turn shows more leads oriented perpendicular to the south-directed sea ice movement. In the Kara Sea leads tend to be oriented along the Franz Josef Land. In addition to that, lead orientation distribution in the Kara Sea shows two maxima at –50° and 55°, while 0° orientation is a local minimum. Leads in the East Siberian Sea more often form along the coastline, preferred orientation at –20°. Beaufort Sea lead orientation show a single minimum at –30° and a maximum at 30°, which approximately correspond to the north-east to south-west direction. Similar to the Central Arctic, the minimum and the maximum in the orientation distribution are more pronounced in late winter. For comparison, Figure 6.15 shows lead orientation distribution calculated by Bröhan and Kaleschke (2014) from AMSR-E passive microwave data. The most likely directions derived from Sentinel-1 scenes with the lead detection algorithm, shown regionally in Figure 6.14, are in line with the lead directions derived by Bröhan and Kaleschke (2014).

6.4 Discussion

Leads detected on Sentinel-1 scenes with the lead detection algorithm described above are compared with the ones derived from MODIS thermal infrared images and AMSR-E passive microwave data. The frequency of lead occurrence show similar patterns to the lead maps derived from MODIS by Reiser et al. (2020). The absolute values are different because various satellite instruments rely on different physical principles. As the result, definition of leads may vary between studies, as mentioned in Section 2.1. A more detailed study on differences in lead detection with SAR image analysis methods, MODIS thermal infrared lead detection, CryoSat-2 lead maps, sea ice concentration maps derived from AMSR2 data, and thermal infrared helicopter-borne imagery is conducted by von Albedyll et al. (2023). Lead orientation distribution correspond to the one derived from AMSR-E data by Bröhan and Kaleschke (2014). These comparisons work as an extra

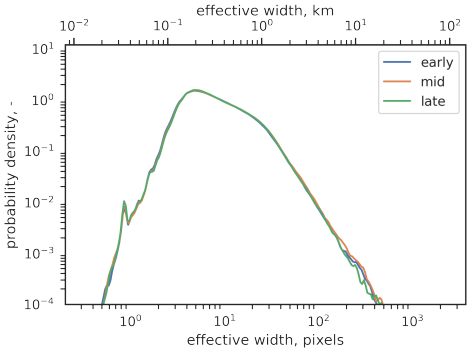

a – Central Arctic

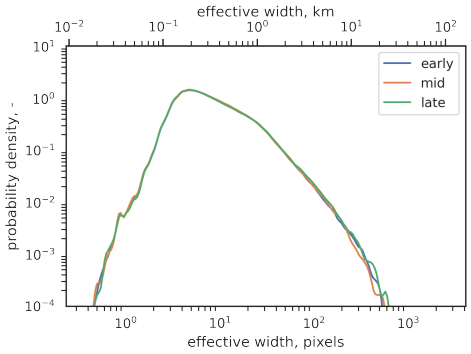

b – Fram Strait

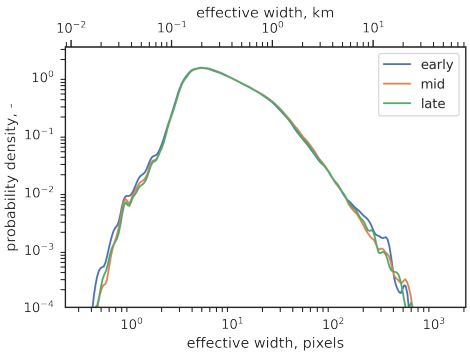

c – Barents Sea

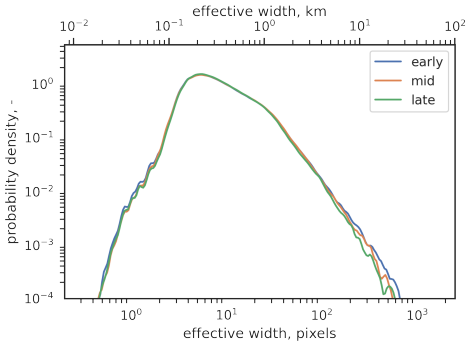

d – Kara Sea

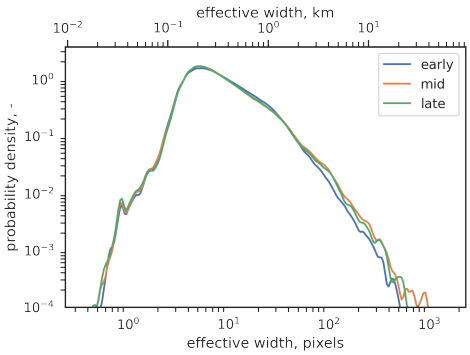

e – Laptev Sea

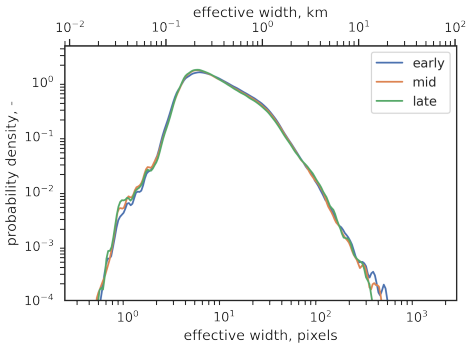

f – East Siberian Sea

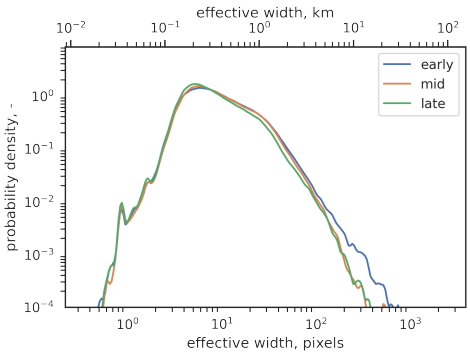

g – Chukchi Sea

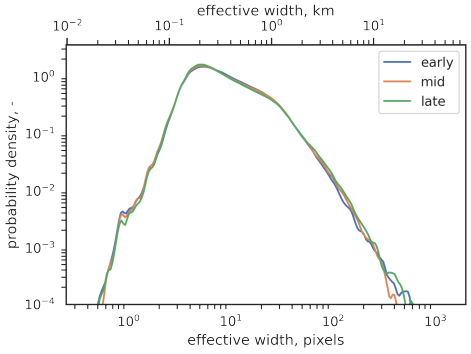

h – Beaufort Sea

Figure 6.13: Regional lead effective width distribution approximating lead width, at log-log scale, size is given in 40 m pixels.

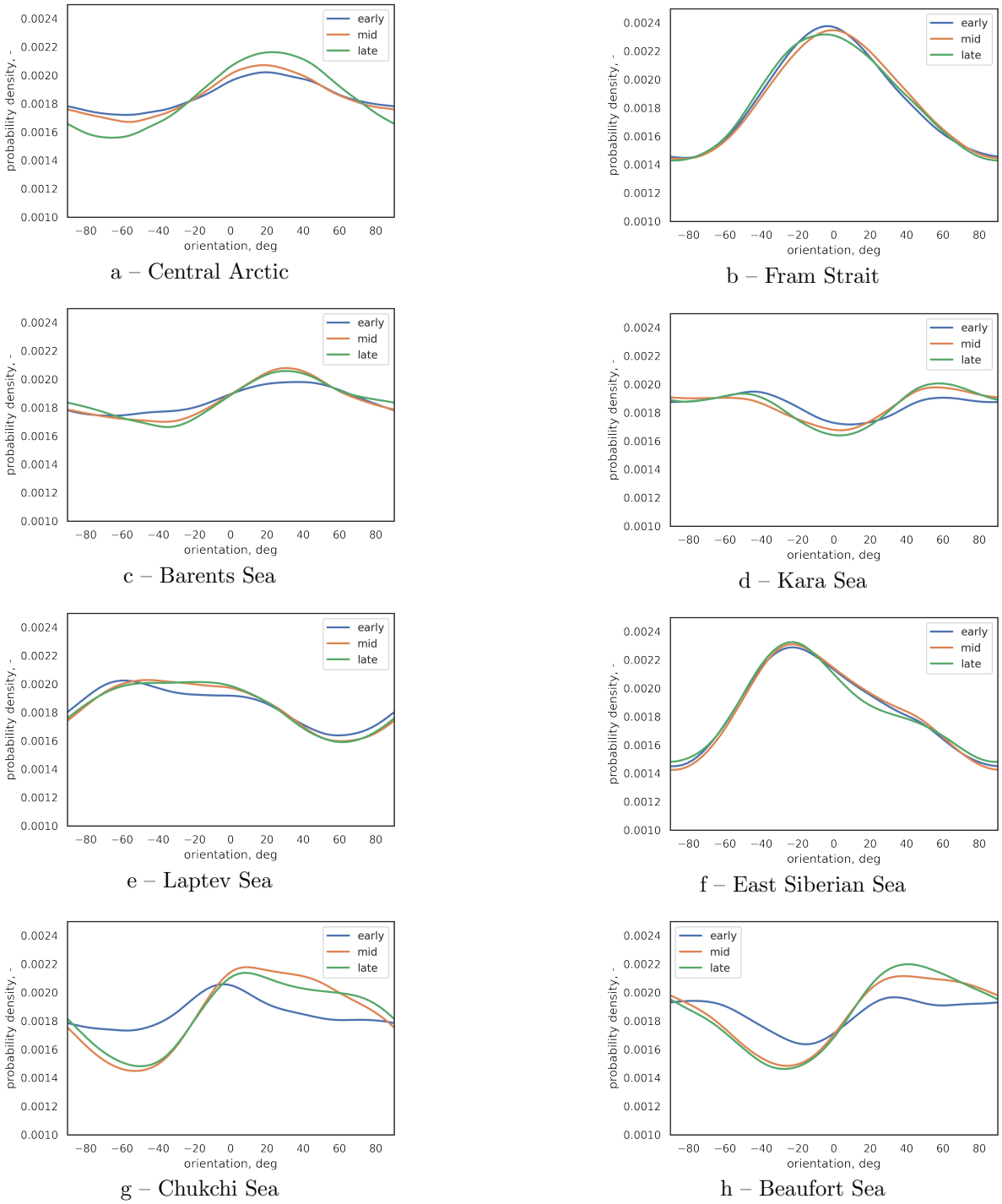

a – Central Arctic

b – Fram Strait

c – Barents Sea

d – Kara Sea

e – Laptev Sea

f – East Siberian Sea

g – Chukchi Sea

h – Beaufort Sea

Figure 6.14: Regional lead orientation distribution. Angles are given relatively to a horizontal line in the corresponding region projection, as shown in Figures 6.1 and 6.2.

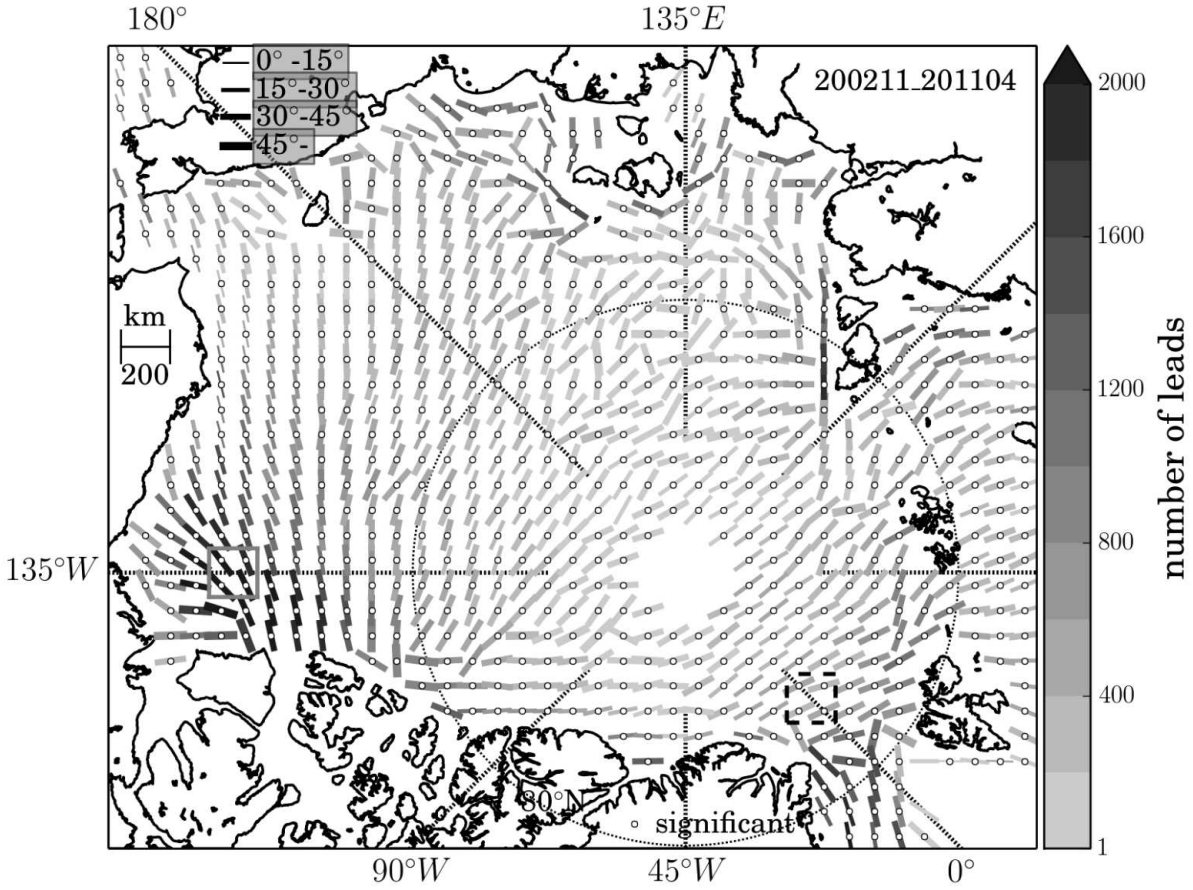

Figure 6.15: Lead orientation derived by Bröhan and Kaleschke (2014) from AMSR-E passive microwave measurements, image from the corresponding paper. The data was taken between 2002 and 2011 years. AMSR-E measurements are gridded at 6.25 km spatial resolution.

evaluation for the lead detection algorithm and prove that the lead detection described in Chapter 5 provides reliable results Arctic-wide with unprecedented resolution of 40 meters. In case, scenes are always acquired in the same geometry, uncertainties from single scenes accumulate into notable stripes in frequency of lead occurrence, as shown in Section 6.3.2. However, if an area is covered at various geometries, these uncertainties are not notable. Such high-resolution maps provide an opportunity to analyze shape of leads and look at lead distributions to a finer scale over the entire Arctic Ocean. Further, various Arctic Ocean regions are described in more details.

6.4.1 Central Arctic

The entire Central Arctic region is covered with sea ice in the beginning of November. The small increase in total number of leads in the region cannot be explained with increase in sea ice area as the sea ice extent might show only small changes in the region throughout winter. Leads are smaller in area and length in the Central Arctic compared to other areas, but the lead width distribution is comparable. Sea ice in the area moves towards the Fram Strait, which is the main gate for sea ice from the Arctic. This movement is called transpolar drift and is driven with the ocean current that moves from the Laptev and the East Siberian Sea through the North Pole towards Fram Strait. As the result sea ice cracks in the direction perpendicular to the drift, resulting in the preferred lead orientation of 30° in the projection shown in Figures 6.1 and 6.2, which also corresponds to the lead direction shown in Figure 6.15.

6.4.2 Fram Strait

Fram Strait is the main gate for sea ice to leave the Arctic Ocean (Spreen et al., 2020). Sea ice drifts southwards, and leads appear mostly in the direction perpendicular to the drift. The preferred orientation is very notable in the area. Long leads are not rare in the area, crossing Fram Strait from east to west. Leads also often occur along the coast of Greenland, as it is shown in Figure 6.4.

6.4.3 Barents Sea

A significant part of the Barents Sea is not frozen even during winter. Most of the ice is located in the northern part of the sea. As the ice freezing throughout winter the sea ice extend in the region increases and, therefore, number of leads also increases. In the northern part there are areas, where leads open more often than in other areas, which is notable in the lead frequency distribution shown in Figure 6.4. Leads are often shorter in the area, although they have a similar width distribution compared to other Arctic

Ocean regions. The orientation of cracks is more uniformly distributed with a small peak perpendicular to the direction to the Fram Strait.

6.4.4 Kara Sea

Small islands in the eastern part of the Kara Sea are located on the way of young sea ice being transported north, therefore many leads are oriented along the sea ice movement, not across as shown in Figure 6.4 and coincide with the direction of lead frequency of occurrence patterns, shown in Figure 6.6a,b. The preferred orientation is not as pronounced as in other Arctic areas and is governed with the western part of the sea, where leads are forming along Franz Josef Land (see Figure 6.14).

6.4.5 Laptev and East Siberian Sea

Both the Laptev Sea and the East Siberian Sea are normally covered with newly formed sea ice in the beginning of November. Thin ice is then being transported north through the transpolar drift, resulting in large number of leads opening. This explains the high variation in number of leads in the area. New Siberian islands between the Laptev Sea and the East Siberian Sea creates a barrier for sea ice movement, which leads to leads openings, as shown in lead frequency of occurrence map in Figure 6.6c-f.

6.4.6 Chukchi Sea

Located between the Beaufort Sea and the East Siberian Sea, north of Bering Strait the Chukchi Sea is located on the way of pacific water to the Arctic. Movement of sea ice northwards often opens leads north of Wrangel Island in the north-west part of the Chukchi Sea, as shown in Figure 6.7a,b. The lead preferred orientation is east to west, perpendicular to the water flow, as shown in Figure 6.14. However, this is different from the orientation derived from passive microwave data in 2002–2011 by Bröhan and Kaleschke (2014), which is shown in Figure 6.15. Figure 6.11, 6.12 6.13 show that leads occurring in the Chukchi Sea are shorter and narrower than in the other areas of the Arctic Ocean.

6.4.7 Beaufort Sea

Sea ice movement in the Beaufort Sea is governed by the Beaufort Gyre, which is an ocean current that moves water along the coast of Canada and Alaska in the clockwise direction. The Beaufort Sea freezes usually freezes during November and from the beginning of December until summer is fully covered with sea ice. Lead orientation

distribution in Figure 6.14 shows a noticeable preferred lead direction perpendicular to the sea ice movement along the Beaufort Gyre. This sea is also a region of wide leads occurrence.

7 Conclusions

To summarize the thesis, the three main questions which has been set for the thesis are concisely answered below.

(1) Can leads be automatically detected on C-band SAR images?

Chapter 4 describes an automatic lead detection algorithm for Sentinel-1 SAR scenes based on traditional machine learning approach when pre-defined image characteristics are calculated prior the classification. Image texture is analyzed with gray-level co-occurrence matrix characteristic, then Random Forest classifier is used to discriminate leads from sea ice. Texture characteristic calculated based on gray-level co-occurrence matrix combined with random forest classification provide a good starting point for lead detection. Various polarimetric combinations of the available SAR channels can provide an additional information for the classifier. Texture features can be extended with more various combinations, however, the more features are added, the less profit they add for the classifier. Recursive feature elimination is an extremely useful approach to evaluate necessity in extra texture feature extension. There is always a tradeoff between computation time and number of various texture characteristic calculated and used for image analysis. Another tradeoff is amount of object detected and the reliability of detection, which is represented with the precision–recall curve. By choosing a threshold on probabilistic classification the classification precision can be increased by a decrease in amount of detected leads and vice versa. The algorithm has been shown to provide reliable lead maps in the European Arctic. In the Siberian Arctic, where young ice rapidly freezes over large areas in the beginning of winter, SAR images indicate smooth surface covering large areas in the absence of rough ice around. In this case ice moves more uniformly, as drag forces from both the ocean currents and the atmosphere do not vary due to various sea ice thickness, which leads to less stresses in the ice and, therefore, less ridging occurs. As surface scattering has a significant impact on backscatter of young ice, areas of young undeformed ice with no ridges are misclassified as leads. Therefore, more advanced image analysis techniques are required to differentiate young ice and leads in the area.

(2) Do deep learning methods provide a more reliable lead maps?

Deep learning methods and convolutional neural networks in particular is a tool that can provide a more robust lead detection algorithm, as described in Chapter 5. This is achieved through the fact, that texture characteristics are not precalculated, but are derived during the training process. This allows texture feature adjustments for particular objects on images, in this case leads on Sentinel-1 images. But this comes at a cost of larger amount of significantly larger amount of computations, However, modern libraries for deep leaning provide an easy way to employ Graphics Processing Units (GPU) for these calculations making them comparable with classifications based on pre-computed texture characteristics.

The lead detection algorithm based on modified U-Net architecture shows better performance compared to the algorithm based on "traditional" machine learning methods when applied to Sentinel-1 scenes taken all over the Arctic Ocean, as shown in Figure 5.2.3. It is able to detect more narrow leads which are 5 pixels (200 m) wide compared to 7 pixel minimal lead width for the lead detection based on GLCM + RFC. Variation in Arctic-wide lead area fraction during January 2019 shows higher correlation with the open water fraction derived from AMSR2 passive microwave measurement, as discussed in Section 5.3.

(3) What insights do high resolution pan-Arctic lead maps provide about lead characteristics in the Arctic Ocean?

In Chapter 6 pan-Arctic binary lead maps are analyzed. First, frequency of lead occurrence shows how often a lead opens in a certain place of the Arctic Ocean. Higher frequency of lead occurrence is found in the areas of faster ice movement, the Beaufort Sea and Fram Strait, as well as in the areas where islands represent obstacles on the way of sea ice movement, northern Barents Sea, north-east part of the Kara Sea, east of the Laptev Sea and east of the East Siberian Sea, north-west of the Chukchi Sea. Second, lead area fraction shows how much open water is present within the sea ice cover. The average lead area fraction is found to be between 3.7% and 2.5% during winters 2016–2022. Third, the lead size distribution follow the power low. Exponent of the effective lead width distribution is 1.86 with standard deviation of 0.16. Some of the previous studies have showed values in the same range (1.6±0.18 by Lindsay and Rothrock (1995)), other studies reported a higher value 2.1...2.61 (detailed in Table 6.1). This extends the applicability of the power law for lead width distribution down to leads 200 meters wide at most. Last, every region of the Arctic Ocean shows the presence of regularity in lead orientation. The preferred orientation shows little variation from year to year and during a single season. In cases of islands being present on the way of sea

ice movement, leads tend to form after the obstacle in along drift direction. In other cases, leads tend to form in the direction perpendicular to the drift direction.

Importance of image preprocessing

The cross-polarization channel HV of Sentinel-1 scenes adds extra information required to detect leads with wind-roughed surface. Without the use of the HV channel the bright leads branch of the lead detection algorithm would not exist. However, the backscatter in the HV channel is weaker and closer to the noise level compared to the co-polarization HH channel. This means the preprocessing is an essential step before the HV channel can be reliability used for automatic image processing algorithms. At the same time, the calibration parameters provided with Sentinel-1 scenes are not precise enough to eliminate thermal and scalloping noise entirely. One could, but should not rely on machine leaning techniques to take the presence of the noise into account automatically. Every step that complicates an image classification task would introduce extra uncertainties and require an exponentially growing training data set. If it is possible to do an advanced preprocessing prior the image classification, it should be done separately from the image classification. For the same reason, in order to account for the variability of SAR lead signatures in C-band backscatter, leads that appear dark and bright on the HH channel should be considered separately.

Reliability of classification

In addition to the lead detection result evaluation on an evaluating data set, the lead maps derived with the lead detection algorithm developed within the study have been compared to data received with several other instruments. First, SAR lead detection results have been compared with 10 m resolution Sentinel-2 optical images taken on the same day. Correspondence between the visible image and the calculated lead map is shown in Figure 5.6. Second, lead area fraction derived from SAR have been compared with open water fraction derived within the same time frame from AMSR2 passive microwave instrument by Spreen et al. (2008). Sentinel-1 -based mean lead area fraction in January 2019 is 2.44% with 0.25% standard deviation, open water concentration derived from AMSR2 is 1.8% with 0.3% standard deviation, as detailed in Section 5.2.3. Third, frequency of lead occurrence derived from SAR have been compared with lead maps based on MODIS thermal infrared images, provided by Willmes et al. (2023) (Section 6.3.2). Fourth, lead orientation derived from SAR images have been compared to the lead orientation calculated from AMSR-E data previously published by Bröhan and Kaleschke (2014) in Section 6.3.7.

Pan-Arctic 40 m resolution lead maps

The lead detection algorithm applied to all Sentinel-1 scenes acquired in the Arctic produces pan-Arctic lead maps at 40 meters resolution. This resolution is significantly higher compared to all other satellite sources providing Arctic-wide sea ice measurements. Passive microwave radiometers provide measurement, which are normally gridded to 6.25 km, MODIS thermal infrared images provide lead maps at 1 km resolution, two-dimensional lead information is derived from CryoSat-2 radar altimeter data at 25 km grid.

Object shape analysis

The 40 m resolution lead maps allow not only detect the presence of leads, but also characterize their shape, as it has been shown in Section 4.1.6. The shape-based filter can be used to additionally discriminate between leads and look-alikes. Although it has been shown in Chapter 5 that the shape-based filter is not required for lead detection in the Arctic Ocean during winter. However, during summer, when surface melt makes microwave and thermal infrared measurement unreliable, the object shape analysis may provide a way to filter out objects that radiometrically look like leads but come from sea ice covered with water. Similar approach can be used for lead detection in Antarctic to filter out flooded thick ice floes.

8 Outlook

The developed lead detection algorithm has only been applied during winter season. Snow and ice melt during summer increases lead detection uncertainties to a degree, when many satellite methods do not provide any automatic results. This is the case for microwave radiometers, microwave scatterometers, thermal infrared imagers, radar altimeters. Apart from these instruments, SAR provides a significantly higher resolution and, with the Sentinel-1 satellite constellation launch, a moderate spatial coverage. While measurements at lower spatial resolution can only indicate the presence of an object, the high spatial resolution also gives an opportunity to analyze shape of the detected object. Since leads often have an elongated shape, the shape of the detected object can help to filter out misclassifications, as it has been shown in Section 4.2.4 and decrease uncertainties in summer lead retrieval. This can potentially lead to a lead detection algorithm that would work all year round, automatically providing information on sea ice conditions, which is otherwise not available.

The SAR operation frequency determines surface penetration depth. It has been mentioned that under certain conditions, sea ice can be undistinguishable from open water. However, this issue can be solved if a dual-frequency SAR system is used. Measurements conducted with C-band SAR instruments (Sentinel-1, Radarsat Constellation Mission) can be extended with an existing L-band SAR instrument, ALOS-2. However, overlap between the acquisition made with two satellites at different orbits is small. A planned Rose-L L-band mission will share the orbit with Sentinel-1 C-band can potentially supplement every C-band measurement over sea ice with a L-band image. Furthermore, an experimental NISAR mission will provide an opportunity to use two frequencies (L-band and S-band) from the same SAR satellite. Therefore, C-band lead detection can be extended with C-band + L-band lead detection which will decrease amount of cases when open water is undistinguishable from sea ice.

Acknowledgements

A long PhD project have come to the end and I would like to acknowledge people who have contributed to it. First of all, I would like to thank my supervisor Dr. Gunnar Spreen for his support and advices throughout my work on the thesis. With the notable degree of freedom in research I have learned a lot during these years, and I really enjoyed it. I would also like to thank Dr. Marcus Huntemann for the numerous technical discussions we had during these years. I would like to acknowledge members of my PhD committee – Prof. Dr. Wolfgang Dierking, Dr. Martin Losch, Prof. Dr. Bruno Tremblay, Dr. Stefan Hendricks, Dr. Gunnar Spreen and Dr. Marcus Huntemann – for their comments and suggestions for the PhD project. I am grateful to Prof. Dr. Christian Haas, the second reviewer for my thesis, and to the members of the examination committee: Dr. Volker Perlick, Prof. Dr. Mihalis Vrekoussis, Dr. Christian Melsheimer, and Maxi Tontsch. I would like to acknowledge Dr. Andrey Pleskachevsky, Dr. Valentin Ludwig and Dr. Philip Rostosky for proofreading my thesis.

A nice work atmosphere at the "Remote Sensing of Polar Regions" group at the University of Bremen and at the "Maritime safety and security" lab at the German Aerospace Center (DLR) have helped me a lot to stay on track with my PhD project. Special thanks go to my former office mates, Dr. Valentin Ludwig and Dr. Philip Rostosky, and the current office mate Dr. Karl Kortum, it is always a lot of fun to discuss both research-related and research-unrelated question with you. I would like to thank ArcTrain students from both the German and the Canadian side for interesting discussions during annual meetings. Being an associated PhD student at ArcTrain gave me many opportunities to participate in conferences, to organize a research stay in Canada, and, most importantly, participate in the Floating University, which took place in the Arctic Ocean. I would also like to thank Dr. Randy Scharien for hosting my research stay at the University of Victoria, and his group for a nice atmosphere. Thanks to Alfred Wegener Institute (AWI) and Dr. Thomas Krumpen for the opportunity to join the TransArktika-2019 expedition as a part of AWI group and get more field experience with sea ice. I would also like to acknowledge GLOMAR PhD school for the numerous courses provided.

And finally, I want to thank my family and friends for their support during my PhD project.

This research has been supported by a Junior Research Group in the framework of the Institutional Strategy of the University of Bremen (funded by the German Excellence Initiative) and by the Deutsche Forschungsgemeinschaft (grant no. GRK1904/ArcTrain), to both of whom I am grateful for the funding. The study is based on Copernicus Sentinel-1 data [2016–2022] provided by Alaska Satellite Facility and the Copernicus Open Access Hub (`https://scihub.copernicus.eu`), processed by ESA.

Bibliography

Alonso-Gonzalez, A., Lopez-Martınez, C., Salembier, P., and Deng, X. (2013). Bilateral Distance Based Filtering for Polarimetric SAR Data. *Remote Sensing*, 5:5620–5641.

Assmy, P., Fernández-Méndez, M., Duarte, P., Meyer, A., Randelhoff, A., Mundy, C. J., Olsen, L. M., Kauko, H. M., Bailey, A., Chierici, M., Cohen, L., Doulgeris, A. P., Ehn, J. K., Fransson, A., Gerland, S., Hop, H., Hudson, S. R., Hughes, N., Itkin, P., Johnsen, G., King, J. A., Koch, B. P., Koenig, Z., Kwasniewski, S., Laney, S. R., Nicolaus, M., Pavlov, A. K., Polashenski, C. M., Provost, C., Rösel, A., Sandbu, M., Spreen, G., Smedsrud, L. H., Sundfjord, A., Taskjelle, T., Tatarek, A., Wiktor, J., Wagner, P. M., Wold, A., Steen, H., and Granskog, M. A. (2017). Leads in Arctic pack ice enable early phytoplankton blooms below snow-covered sea ice. *Scientific Reports*, 7.

Assur, A. (1960). Composition of sea ice and its tensile strength.

Bentes, C., Velotto, D., and Tings, B. (2018). Ship Classification in TerraSAR-X Images With Convolutional Neural Networks. *IEEE Journal of Oceanic Engineering*, 43(1):258–266.

Boulze, H., Korosov, A., and Brajard, J. (2020). Classification of Sea Ice Types in Sentinel-1 SAR Data Using Convolutional Neural Networks. *Remote Sensing*, 12(13):2165.

Breiman, L. (2001). Random Forests. *Machine Learning*, 45(1):5–32.

Brekke, C., Holt, B., Jones, C., and Skrunes, S. (2014). Discrimination of oil spills from newly formed sea ice by synthetic aperture radar. *Remote Sensing of Environment*, 145:1–14.

Brekke, C., Jones, C. E., Skrunes, S., Holt, B., and Espeseth, M. (2016). Cross-Correlation Between Polarization Channels in SAR Imagery Over Oceanographic Features. *IEEE Transactions on Geoscience and Remote Sensing*, 13(7):997–1001.

Bröhan, D. and Kaleschke, L. (2014). A nine-year climatology of arctic sea ice lead orientation and frequency from AMSR-E. *Remote Sensing*, 6:1451–1475.

Burger, W. and Burge, M. J. (2009). *Principles of Digital Image Processing: Core Algorithms*. Springer, London.

Chechin, D. G., Makhotina, I. A., Lüpkes, C., and Makshtas, A. P. (2019). Effect of Wind Speed and Leads on Clear-Sky Cooling over Arctic Sea Ice during Polar Night. *Journal of the Atmospheric Sciences*, 76(8):2481–2503.

Cortes, C., Mohri, M., and Rostamizadeh, A. (2009). L2 Regularization for Learning Kernels.

Curry, J. A. and Schramm, J. L. (1995). Sea Ice-Albedo Climate Feedback Mechanism. *Journal of Climate*, 8:240–247.

Dai, A., Luo, D., Song, M., and Liu, J. (2019). Arctic amplification is caused by sea-ice loss under increasing CO2. *Nature Communications*, 10(1):121.

Davis, J. and Goadrich, M. (2006). The Relationship Between Precision-Recall and ROC Curves. In *Proceedings of the 23rd International Conference on Machine Learning*.

Dierking, W. (2010). Mapping of different sea ice regimes using images from sentinel-1 and ALOS synthetic aperture radar. *IEEE Transactions on Geoscience and Remote Sensing*, 48(3):1045–1058.

Dierking, W. (2013). Sea Ice Monitoring by Synthetic Aperture Radar. *Oceanography*, 26(3):100–111.

Dierking, W. and Wesche, C. (2014). C-band radar polarimetry - Useful for detection of icebergs in sea ice? *IEEE Transactions on Geoscience and Remote Sensing*, 52(1):25–37.

Ebert, E. E. and Curry, J. A. (1993). An Intermediate One-Dimensional Thermodynamic Sea Ice Model for Investigating Ice-Atmosphere Interactions. *Journal of Geophysical Research*, 98:10085–10109.

ESA (2016). Sentinel-1 Level 1 Detailed Algorithm Definition. Technical report, ESA.

Fawcett, T. (2006). An introduction to ROC analysis. *Pattern Recognition Letters*, 27:861–874.

Fukushima, K. (1969). Visual Feature Extraction by a Multilayered Network of Analog Threshold Elements. *IEEE Transactions on Systems Science and Cybernetics*, 5(4):322–333.

Haralick, R. M., Shanmugam, K., and Dinstein, I. (1973). Textural Features for Image Classification. *IEEE Transactions on Systems, Man, and Cybernetics*, smc-3(6):610–621.

Hinton, G. E., Srivastava, N., Krizhevsky, A., Sutskever, I., and Salakhutdinov, R. R. (2012). Improving neural networks by preventing co-adaptation of feature detectors.

Ho, T. K. (1998). The random subspace method for constructing decision forests. *IEEE Transactions on Pattern Analysis and Machine Intelligence*, 20(8):832–844.

Hutchings, J. K., Heil, P., and Hibler, W. D. (2005). Modeling linear kinematic features in pack ice. *Monthly Weather Review*, 133(12):3481–3497.

Hutter, N., Zampieri, L., and Losch, M. (2019). Leads and ridges in Arctic sea ice from RGPS data and a new tracking algorithm. *Cryosphere*, 13(2):627–645.

Isleifson, D., Galley, R. J., Barber, D. G., Landy, J. C., Komarov, A. S., and Shafai, L. (2014). A Study on the C-Band Polarimetric Scattering and Physical Characteristics of Frost Flowers on Experimental Sea Ice. *IEEE Transactions on Geoscience and Remote Sensing*, 52(3):1787–1798.

Ivanova, N., Rampal, P., and Bouillon, S. (2016). Error assessment of satellite-derived lead fraction in the Arctic. *The Cryosphere*, 10:585–595.

Karvonen, J. (2014). Baltic sea ice concentration estimation based on C-band dual-polarized SAR data. *IEEE Transactions on Geoscience and Remote Sensing*, 52(9):5558–5566.

Korosov, A. A. and Park, J.-W. (2016). Very high resolution classification of Sentinel-1A data using segmentation and texture analysis. In *Living Planet Symposium 2016*.

Kwok, R. (2018). Arctic sea ice thickness, volume, and multiyear ice coverage: Losses and coupled variability (1958–2018). *Environmental Research Letters*, 13(10):105005.

Leigh, S., Wang, Z., and Clausi, D. A. (2014). Automated ice-water classification using dual polarization SAR satellite imagery. *IEEE Transactions on Geoscience and Remote Sensing*, 52(9):5529–5539.

Lindsay, R. W. and Rothrock, D. A. (1995). Arctic sea ice leads from advanced very high resolution radiometer images. *Journal of Geophysical Research*, 100(C3):4533–4544.

Liu, H., Guo, H., and Zhang, L. (2015). SVM-Based Sea Ice Classification Using Textural Features and Concentration From RADARSAT-2 Dual-Pol ScanSAR Data. *IEEE Journal of Selected Topics in Applied Earth Observations and Remote Sensing*.

Lüpkes, C., Vihma, T., Birnbaum, G., and Wacker, U. (2008). Influence of leads in sea ice on the temperature of the atmospheric boundary layer during polar night. *Geophysical Research Letters*, 35(3).

Malmgren-Hansen, D., Pedersen, L. T., Nielsen, A. A., Kreiner, M. B., Saldo, R., Skriver, H., Lavelle, J., Buus-Hinkler, J., and Krane, K. H. (2021). A Convolutional Neural Network Architecture for Sentinel-1 and AMSR2 Data Fusion. *IEEE Transactions on Geoscience and Remote Sensing*, 59(3):1890–1902.

Mao, Y., Yang, Y., Ma, Z., Li, M., Su, H., and Zhang, J. (2020). Efficient Low-Cost Ship Detection for SAR Imagery Based on Simplified U-Net. *IEEE Access*, 8:69742–69753.

Marcq, S. and Weiss, J. (2012). Influence of sea ice lead-width distribution on turbulent heat transfer between the ocean and the atmosphere. *The Cryosphere*, 6:143–156.

Maykut, G. A. (1978). Energy exchange over young sea ice in the central Arctic. *Journal of Geophysical Research*, 83(C7):3646–3658.

Meier, W. N., Stroeve, J., and Fetterer, F. (2007). Whither Arctic sea ice? A clear signal of decline regionally, seasonally and extending beyond the satellite record. *Annals of Glaciology*, 46:428–434.

Moen, M. A. N., Anfinsen, S. N., Doulgeris, A. P., Renner, A. H. H., and Gerland, S. (2015). Assessing polarimetric SAR sea-ice classifications using consecutive day images. *Annals of Glaciology*, 56(69):285–294.

Murashkin, D. and Frost, A. (2021). Arctic Sea ICE Mapping Using Sentinel-1 SAR Scenes with a Convolutional Neural Network. In *2021 IEEE International Geoscience and Remote Sensing Symposium IGARSS*, pages 5660–5663.

Murashkin, D. and Spreen, G. (2019). Sea Ice Leads Detected From Sentinel-1 SAR Images. In *IGARSS 2019 - 2019 IEEE International Geoscience and Remote Sensing Symposium*, pages 174–177.

Murashkin, D., Spreen, G., Huntemann, M., and Dierking, W. (2018). Method for detection of leads from Sentinel-1 SAR images. *Annals of Glaciology*, 59(76):124–136.

Najman, L., Schmitt, M., Najman, L., Schmitt, M., and Signal, F. (1994). Watershed of a Continuous Function To cite this version : HAL Id : Hal-00622129. *Signal Processing, Elsevier*, 38(1):99–112.

National Snow and Ice Data Center, Meier, W., and Stroeve, J. (2022). An Updated Assessment of the Changing Arctic Sea Ice Cover. *Oceanography*.

Nghiem, S. V., Martin, S., Perovich, D. K., Kwok, R., Drucker, R., and Gow, A. J. (1997). A laboratory study of the effect of frost flowers on C band radar backscatter from sea ice. *Journal of Geophysical Research*, 102(C2):3357–3370.

Notz, D. and Worster, M. G. (2009). Desalination processes of sea ice revisited. *Journal of Geophysical Research: Oceans*, 114(C5).

Park, J. W., Korosov, A. A., Babiker, M., Won, J. S., Hansen, M. W., and Kim, H. C. (2020). Classification of sea ice types in Sentinel-1 synthetic aperture radar images. *The Cryosphere*, 14(8):2629–2645.

Qu, M., Pang, X., Zhao, X., Zhang, J., Ji, Q., and Fan, P. (2019). Estimation of turbulent heat flux over leads using satellite thermal images. pages 1565–1582.

Reiser, F., Willmes, S., and Heinemann, G. (2020). A New Algorithm for Daily Sea Ice Lead Identification in the Arctic and Antarctic Winter from Thermal-Infrared Satellite Imagery. *Remote Sensing*, 12(12):1957.

Ressel, R., Singha, S., Lehner, S., Rosel, A., and Spreen, G. (2016). Investigation into Different Polarimetric Features for Sea Ice Classification Using X-Band Synthetic Aperture Radar. *IEEE Journal of Selected Topics in Applied Earth Observations and Remote Sensing*, 9(7):3131–3143.

Ringeisen, D., Losch, M., Tremblay, L. B., and Hutter, N. (2019). Simulating intersection angles between conjugate faults in sea ice with different viscous – plastic rheologies. *The Cryosphere*, 13:1167–1186.

Röhrs, J. and Kaleschke, L. (2012). An algorithm to detect sea ice leads by using AMSR-E passive microwave imagery. *The Cryosphere*, 6:343–352.

Ronneberger, O., Fischer, P., and Brox, T. (2015). U-Net: Convolutional Networks for Biomedical Image Segmentation.

Rothrock, D. A. and Thorndike, A. S. (1984). Measuring the sea ice floe size distribution. *Journal of Geophysical Research: Oceans*, 89(C4):6477–6486.

Scharien, R. K. and Yackel, J. J. (2005). Analysis of Surface Roughness and Morphology of First-Year Sea Ice Melt Ponds: Implications for Microwave Scattering. *IEEE Transactions on Geoscience and Remote Sensing*, 43(12):2927–2939.

Serreze, M. C., Barrett, A. P., Stroeve, J. C., Kindig, D. N., and Holland, M. M. (2009). The emergence of surface-based Arctic amplification. *The Cryosphere*, 3(1):11–19.

Serreze, M. C. and Francis, J. A. (2006). The Arctic Amplification Debate. *Climatic Change*, 76(3):241–264.

Spreen, G., de Steur, L., Divine, D., Gerland, S., Hansen, E., and Kwok, R. (2020). Arctic Sea Ice Volume Export Through Fram Strait From 1992 to 2014. *Journal of Geophysical Research: Oceans*, 125(6):e2019JC016039.

Spreen, G., Kaleschke, L., and Heygster, G. (2008). Sea ice remote sensing using AMSR-E 89-GHz channels. *Journal of Geophysical Research*, 113.

Steffen, K. (1991). Energy flux density estintation over sea ice based on satellite passive microwave measurements. *Annals of Glaciology*, 15:178–183.

Stirling, I. (1997). The importance of polynyas, ice edges, and leads to marine mammals and birds. *Journal of Marine Systems*, 10(1):9–21.

Stokholm, A., Wulf, T., Kucik, A., Saldo, R., Buus-Hinkler, J., and Hvidegaard, S. M. (2022). AI4SeaIce: Toward Solving Ambiguous SAR Textures in Convolutional Neural Networks for Automatic Sea Ice Concentration Charting. *IEEE Transactions on Geoscience and Remote Sensing*, 60:1–13.

Thielke, L., Spreen, G., Huntemann, M., and Murashkin, D. (2023). *Spatio-Temporal Variability of Small-Scale Leads Based on Helicopter Winter Sea Ice Surface Temperatures*.

Thorndike, A. S., Rothrock, D. A., Maykut, G. A., and Colony, R. (1975). The thickness distribution of sea ice. *Journal of Geophysical Research*, 80(33):4501–4513.

Tomasi, C. and Manduchi, R. (1998). Bilateral filtering for gray and color images. In *Sixth International Conference on Computer Vision*.

Ulaby, F. T. and Long, D. G. (2014). *Microwave Radar and Radiometric Remote Sensing*. The University of Michigan Press.

von Albedyll, L., Hendricks, S., Hutter, N., Murashkin, D., Kaleschke, L., Willmes, S., Thielke, L., Tian-Kunze, X., Spreen, G., and Haas, C. (2023). Lead fractions from SAR-derived sea ice divergence during MOSAiC. *The Cryosphere Discussions*, pages 1–39.

Wang, Q., Danilov, S., Jung, T., Kaleschke, L., and Wernecke, A. (2016a). Sea ice leads in the Arctic Ocean: Model assessment, interannual variability and trends. *Geophysical Research Letters*, 43:7019–7027.

Wang, Y., Holt, B., Rogers, W. E., Thomson, J., and Shen, H. H. (2016b). Wind and wave influences on sea ice floe size and leads in the Beaufort and Chukchi Seas during the summer-fall transition 2014. *Journal of Geophysical Research: Oceans*, 121:1502–1525.

Weeks, W. (2010). *On Sea Ice*. University of Alaska Press, Fairbanks.

Weiss, J. (2003). Scaling of fracture and faulting of ice on earth. *Surveys in Geophysics*, 24.

Wendisch, M., Brückner, M., Crewell, S., Ehrlich, A., Notholt, J., Lüpkes, C., Macke, A., Burrows, J. P., Rinke, A., Quaas, J., Maturilli, M., Schemann, V., Shupe, M. D., Akansu, E. F., Barrientos-Velasco, C., Bärfuss, K., Blechschmidt, A.-M., Block, K., Bougoudis, I., Bozem, H., Böckmann, C., Bracher, A., Bresson, H., Bretschneider, L., Buschmann, M., Chechin, D. G., Chylik, J., Dahlke, S., Deneke, H., Dethloff, K., Donth, T., Dorn, W., Dupuy, R., Ebell, K., Egerer, U., Engelmann, R., Eppers, O., Gerdes, R., Gierens, R., Gorodetskaya, I. V., Gottschalk, M., Griesche, H., Gryanik, V. M., Handorf, D., Harm-Altstädter, B., Hartmann, J., Hartmann, M., Heinold, B., Herber, A., Herrmann, H., Heygster, G., Höschel, I., Hofmann, Z., Hölemann, J., Hünerbein, A., Jafariserajehlou, S., Jäkel, E., Jacobi, C., Janout, M., Jansen, F., Jourdan, O., Jurányi, Z., Kalesse-Los, H., Kanzow, T., Käthner, R., Kliesch, L. L., Klingebiel, M., Knudsen, E. M., Kovács, T., Körtke, W., Krampe, D., Kretzschmar, J., Kreyling, D., Kulla, B., Kunkel, D., Lampert, A., Lauer, M., Lelli, L., von Lerber, A., Linke, O., Löhnert, U., Lonardi, M., Losa, S. N., Losch, M., Maahn, M., Mech, M., Mei, L., Mertes, S., Metzner, E., Mewes, D., Michaelis, J., Mioche, G., Moser, M., Nakoudi, K., Neggers, R., Neuber, R., Nomokonova, T., Oelker, J., Papakonstantinou-Presvelou, I., Pätzold, F., Pefanis, V., Pohl, C., van Pinxteren, M., Radovan, A., Rhein, M., Rex, M., Richter, A., Risse, N., Ritter, C., Rostosky, P., Rozanov, V. V., Donoso, E. R., Garfias, P. S., Salzmann, M., Schacht, J., Schäfer, M., Schneider, J., Schnierstein, N., Seifert, P., Seo, S., Siebert, H., Soppa, M. A., Spreen, G., Stachlewska, I. S., Stapf, J., Stratmann, F., Tegen, I., Viceto, C., Voigt, C., Vountas, M., Walbröl, A., Walter, M., Wehner, B., Wex, H., Willmes, S., Zanatta, M., and Zeppenfeld, S. (2023). Atmospheric and Surface Processes, and Feedback Mechanisms Determining Arctic Amplification: A Review of First Results and Prospects of the (AC)3 Project. *Bulletin of the American Meteorological Society*, 104(1):E208–E242.

Wernecke, A. and Kaleschke, L. (2015). Lead detection in Arctic sea ice from CryoSat-2: Quality assessment, lead area fraction and width distribution. *The Cryosphere-Cryosphere*, 9:1955–1968.

Wessel, P. and Smith, W. H. F. (1996). A global, self-consistent, hierarchical, high-resolution shoreline database. *Journal of Geophysical Research: Solid Earth*, 101(B4):8741–8743.

Willmes, S. and Heinemann, G. (2015). Pan-Arctic lead detection from MODIS thermal infrared imagery. *Annals of Glaciology*, 56(69):29–37.

Willmes, S. and Heinemann, G. (2016). Sea-ice wintertime lead frequencies and regional characteristics in the Arctic, 2003-2015. *Remote Sensing*, 8(4).

Willmes, S., Heinemann, G., and Schnaase, F. (2023). Patterns of wintertime Arctic sea ice leads and their relation to winds and ocean currents. *The Cryosphere Discussions*, pages 1–23.

World Meteorological Organization (2014). WMO Sea-Ice Nomenclature.

Zakhvatkina, N., Korosov, A., Muckenhuber, S., Sandven, S., and Babiker, M. (2017). Operational algorithm for ice–water classification on dual-polarized RADARSAT-2 images. *The Cryosphere*, 11:33–46.

Zakhvatkina, N. Y., Alexandrov, V. Y., Johannessen, O. M., Sandven, S., and Frolov, I. Y. (2013). Classification of sea ice types in ENVISAT synthetic aperture radar images. *IEEE Transactions on Geoscience and Remote Sensing*, 51(5):2587–2600.

Zhang, T. Y. and Suen, C. Y. (1984). A fast parallel algorithm for thinning digital patterns. *Communications of the ACM*, 27(3):236–239.